Lightning Induced Voltages on Overhead Lines above Non-Uniform and Non-Homogeneous Ground

Author
Raúl Esteban Jiménez Mejía

Master Thesis Dissertation

Universidad Nacional de Colombia
Departamento de Energía Eléctrica y Automática
Facultad de Minas
November 2014

Lightning Induced Voltages on Overhead Lines above Non-Uniform and Non-Homogeneous Ground

Author
Raúl Esteban Jiménez Mejía

Master Thesis Dissertation
Presented as a partial fulfillment of the requirements for the degree of Master on Electrical Engineering

Advisor
Prof. Javier Gustavo Herrera Murcia, Ph.D.

Universidad Nacional de Colombia
Departamento de Energía Eléctrica y Automática
Facultad de Minas
November 2014

To my Parents

Acknowledgments

There are many people that I must be grateful with by all of their attention and comprehension along these two years. I would like to express my sincere gratitude to all of those that have been there offering me their valuable comments and assistance during the development of this thesis. Along the time working on it, I have learned not only about lighting induced voltages but also that when you are with a good working group and excellent people around you, there are more probabilities to succeed.

I wish to thank Prof. Javier Herrera for accepting to be the advisor of this work and the way how he from the first time offered me all his experience on lightning research for the development of this thesis.

I really have to highlight all the support that I have received from the Research Group on Applied Technologies (GITA) and express my especial gratitude to Prof. Guillermo Mesa who has been a very important advisor not only academically but also as a real and sincere friend. I would also like to thank to Prof. Clara Rojo for all of her valuable advices and her support whereas I held my position as teaching assistant of the high voltage laboratory.

My sincere gratitude to my parents for all of their confidence on me and on my work. Special thanks to my brother David who has given me important advices along this work and to Stephanie who has been present to encourage me along this two years.

I am sincerely grateful to my teamwork and friends: Gilbert, Camilo and Juan Fernando for backing me up when I was unavailable and for all of their valuable suggestions and encouragements.

Finally, I would also like to address my gratitude to all of my old friends and colleagues for their valuable assistance and comments.

Abstract

Lightning induced voltages are one of the most common sources of failures on distribution networks operating in high lightning activity regions. Traditionally, the selection of insulation levels and protecting devices are carried out using statistical analysis based on typical values of resistivity and assuming a homogeneous ground for the whole network. In calculating lightning induced voltages, the effect of the topography and non-homogeneities of the ground have been traditionally neglected.

In rural distribution lines, non-homogeneous and non-uniform ground is a common feature. In literature, induced voltages calculations are mainly calculated based on several assumptions that are not valid when more realistic conditions are taken into account. In order to allow a better selection of protective devices and hence contributing to the improvement of some power quality indicators of rural distribution networks, the calculation of lightning induced voltages for distribution lines must be performed including the effects of the non-homogeneous and non-uniform ground.

Most of the theoretical approaches proposed for calculating the propagation path effects on the radiated electromagnetic fields for a current dipole above ground, are valid only in the far-field region even when considering irregular and inhomogeneous terrain. Despite some authors have demonstrated the validity of those approaches for flat ground in the near field range calculations, there are valid for some specific cases and geometric symmetry that in some practical cases cannot be assumed.

In order to overcome this problem, this thesis presents an extensive application of a full wave solution obtained from the implementation of the Finite Difference Time Domain (FDTD) method including a non-regular mesh. This method is applied to the calculation of lightning induced voltages on an overhead single wire when different ground features such as: homogeneity, inhomogeneity and non-uniformity are present all simultaneously in a simulation scenario. In order to validate the FDTD implementation, some numerical comparisons were made with previous results presented in the literature.

The aim of this thesis is to provide new elements related to the effects on lighting induced voltages on overhead lines when different electric and geometric parameters of the surrounding ground are considered. Along this thesis, the lightning induced voltage problem has been analyzed taking into account three involved aspects individually: the return-stroke model, the propagation of the electromagnetic field produced by it, and the resulting induced voltages on the overhead lines once all their models are included into an FDTD simulation.

This document has been divided into eight sections. The first section presents a discussion about lightning induced voltages and how they have been addressed in the literature. Throughout this

section all the involved elements into the lighting induced problem have been addressed and a short discussion about their previous results and conclusions is also presented.

In section 2 the scope of the thesis is defined in order to give the reader a brief summary about the objectives that were established in the master thesis proposal.

Section 3 presents the FDTD method. In this section most of the theoretical background is presented related to: sources, lumped elements and thin-wire modeling techniques. Next, the FDTD method is formulated for a non-regular mesh and a general formulation for an automatic meshing algorithm is proposed. Finally, a comparison between the FDTD method implementation used in this thesis and some experimental data from a two horizontal wires cross-talk problem is presented.

Section 4 deals with the calculation of radiated fields when different propagation paths are present. Homogeneous ground effects on radiated fields were obtained by using the Norton's approach and the surface impedance concept. Inhomogeneities of the ground conductivity for flat grounds were also analyzed by using the surface impedance concept and the Wait´s formula derived from the compensation theorem; the Wait´s formulas for a mixed-path of two and three section were implemented and compared with some results presented before in literature. Finally, the terrain non-uniformity was addressed by means of the Ott's integral approach. Despite all of these implemented approaches allow the analysis of radiated fields, they are derived under several assumptions and are valid only for the far field region and a cylindrical symmetry regarding geometry. Then, a comparison between these and the results obtained by means of the FDTD method were performed for different simulation scenarios in order to analyze their validity.

In section 5 the lightning return-stroke is modeled by means of an implementation of engineering and electromagnetic models. A discussion about the current distribution along the channel depending on the return-stroke model is also presented. Besides, a comparison between the antenna theory and the series RL-loaded thin-wire model included into the FDTD method was carried out taking into account the characteristics of apparent propagation velocity and current wave shape along the channel.

In section 6 the lightning radiated fields are calculated for different propagation path conditions such as: perfectly conducting ground, homogeneous finitely conductive ground and inhomogeneous conducting ground. For those propagation paths a set of comparisons between the FDTD method and the approximated formulas discussed in section 5 were performed.

Lightning induced voltages are analyzed in section 7. In this section the lightning channel and the overhead line are included into the FDTD method. A set of simulations scenarios were proposed in order to evaluate the influence of different ground features on the induced voltages on a single overhead-wire. Important influences on induced voltage waveforms were determined for inhomogeneous and irregular terrains, resulting in changes on polarity and higher induced peak voltages values when compared to those obtained from a flat homogeneous ground.

In section 8 concluding remarks about the analyzed cases and most critical situations are presented. There is also a future work proposed by the author based on the obtained results.

Table of Contents

Table of Figures

1 The Lighting Induced Voltage Problem: State of the Art Discussion

Lightning induced over-voltages on power overhead lines has been one of the most important research fields related to lightning return strokes consequences, not only because its negative effects on power quality indicators, but also for the academic challenge they represent. Several proposals have been made in the literature in order to relate the lighting return stroke characteristics and the induced voltages on overhead lines [1], some of them resulting into different induced voltage magnitudes and waveforms because of the assumed theoretical background and the different approaches used for the return stroke current representation. Another important source of difference is the coupling model for the incident electromagnetic field on the overhead line, which depending on the assumptions can lead to different induced voltage magnitudes. One of the most popular and complete formulation for the coupling of an incident electromagnetic field to an overhead line was proposed by Agrawal [2], which allows the inclusion of simultaneous horizontal and vertical components of the lightning radiated electric field as excitation sources in the transmission line equations. From this approach, the lightning induced voltage problem has been focused traditionally on the lightning radiated field calculation, especially for the electric field components.

The problem of lightning induced voltages on overhead lines has been usually analyzed taking into account three aspects: 1) the lightning return-stroke modeling including the characteristics of the current propagation along the channel, 2) the calculation of the electromagnetic fields including the effect of the propagation path and 3), the coupling of the electromagnetic fields with the overhead line. All the involved aspects in lightning induced voltages must be carefully analyzed and depending on the problem scenario, they can become crucial for the induced voltage characteristics.

For lightning protection engineering and lightning induced voltages analysis, several representations of the lightning return-stroke channel have been used in order to reproduce the measured electromagnetic fields due to the natural lightning discharges, resulting in reasonably agreement [4]. Nowadays, several techniques have contributed to determine the characteristics, parameters and typical waveforms of the lightning current discharges for the study of lightning interactions between other systems, especially with overhead transmission lines [5][6][7][8].

The effects of the Lightning Electromagnetic Pulse - LEMP can lead to over-voltages and flashovers depending on the lightning current characteristics and the distance between the overhead-line and the striking point [4][9]. When the induced voltage on the line propagates along the overhead line reaching the distribution transformer, severe damages in the transformer itself, protective devices or in the end-user's equipment can be caused due to the transferred surge [10][11][12].

This situation is even more critical in rural distribution lines where costs and time associated to the re-establishment of the service are representative. Taking into account all of the problems that could be presented by the lighting induced voltages on overhead lines, the well understanding of this electromagnetic phenomena and the parameters that are involved in it would allow a better power lines and protective devices design [13].

It has been also demonstrated that the lightning induced voltages are reasonably affected by the characteristics of the ground. Not only because the overhead line parameters are affected [14], but also because the propagation path is able to modify the lightning radiated electric and magnetic field waveforms, and hence, the its electromagnetic coupling with the line conductors [15]. In actual overhead lines, several ground configurations can be found along them being more common finding ground in-homogeneities and topography irregularities in rural regions where the lines are longer covering large areas. However, the most common ground structure considered for lighting induced voltage calculations, even independent on the length of the line, has been the flat homogeneous ground.

The problem of calculating induced voltages on overhead lines lies on the calculation of the incident field radiated due to a lightning return-stroke and its electromagnetic coupling to the overhead line. In order to calculate the radiated electromagnetic fields due to the current distribution along the channel, several return-stroke models have been presented in literature [6]. Although, the lightning-channel modeling is still a research topic, existing models have being useful for engineering applications and they have enabled the analysis of the lightning induced voltages effects and effective protective systems design [13].

The calculation of the radiated fields by an electrical dipole located above flat homogeneous was historically addressed by Arnold Sommerfeld who proposed a set of equations for calculating radiated electric and magnetic field components based on a cylindrical expansion of the magnetic vector potential, and a Leontovich's boundary condition of continuity along the air-ground interface [16]. Sommerfeld´s integrals take into account the presence of a flat homogeneous ground and establish a rigorous solution for the radiated electromagnetic field components due to a harmonic oscillator current dipole [16]. However, because of his original formulation doesn't have an analytical closed solution, numerical techniques must be implemented for the solution of the integrals in order to calculate the radiated electric field components. These numerical approaches must deal with high oscillatory integrands with slow convergence and for most of the practical cases it leads to time-consuming computational routines [16]. Although there have been proposed several approaches in order to solve the Sommerfeld's integrals with reasonably low computation times when evaluating them at an observation point [17], the rigorous solution based on the Sommerfeld´s formulation continues being time-consuming when several observation points must be calculated or detailed frequency spectrum must be analyzed.

One of the most interesting results in the Sommerfeld's formulation is that after some rearrangements of the terms in the resulting equations, the total solution of the radiated fields can be seen as superposition of a perfectly conductive ground solution and a term that relates the

ground effect on the total field [16]. Based on those results, various approximations and simplified formulas have been derived from the Sommerfeld´s original formulation and proposed in literature to deal with the radiation above a finitely conducting ground [17][20]. The Norton´s proposal is one of the most popular; in this approach, the radiated fields can be calculated without the integration of the Sommerfeld´s integrals allowing faster and quite accurate results for several cases. Norton´s approach predicts the waveform of the radiated fields above finitely conductive ground with reasonably accuracy for several cases when compared with the rigorous solution.

A popular solution for the lightning radiated field calculation above finitely conductive flat ground has been derived from the Norton's approach with good accurate results for typical ground resistivity values, this approach is known as the Cooray – Rubinstein (CR) formula [21][22], which allows predicting the horizontal electric field at intermediate and long ranges from the lightning channel base by using straightforward calculations. Despite its usefulness, some considerations to the initial CR formulation must be taken into account when lightning radiated fields are calculated in presence of high resistivity grounds [17][22]. The accuracy of the CR formula has been tested in different scenarios showing good agreements when they are compared with rigorous solutions.

Lightning induced voltages are also dependent on the striking point. Typically, they have been well characterized in presence of finitely conducting flat ground [23]. Recently, there have been some attempts to calculate the induced voltages when lightning strikes to an elevated and tall object presenting differences related to the flat ground strike scenario [24][25]. From them, coupling models to the overhead line have been extended satisfactorily and measured data have been reasonably reproduced [25][26].

When ground inhomogeneities are present in the propagation path within the near field region and even for some of the far field regions, the formulas and approximations mentioned before cannot be used and only for some cases accurate results can be found. The solution to this problem has been obtained mainly by the application of the compensation theorem or the Green´s theorem based on the wave solution in the frequency domain [16]. These solutions have been typically proposed taking into account some simplified boundary conditions and symmetry assumptions regarding the geometry.

When ground conductivity variations are present along the propagation path above the ground surface, the traveling electromagnetic wave faces several changes of surface impedances and hence the existence of different reflection coefficients along the surface terrain that are able to modify the electromagnetic waveform characteristics; this propagation path is also known as a *mixed-path*.

For the study and analysis of the mixed-path problem, Wait proposed a formula in order to deal with it based on the compensation theorem and the surface impedance concept [18][19]. Wait´s formulation for mixed paths is one of the most used in literature [18] and its validity within the near field range have been analyzed by several authors showing good agreement for some of the field components, when compared with a full-wave solutions as the ones obtained from the FDTD method [19]. An alternative formulation is based on the integral equation method and the Green´s

theorem. This formulation not only allows the inclusion of non-homogeneities, but also non-uniformities along the boundary between air and the ground. However, several assumptions must be imposed to the radiated field characteristics and accurate results can be obtained for the far field region only and taking into account some high-frequency bands [16] [18].

The effects of the ground inhomogeneities and non-uniformities on the lightning radiated fields and their related induced voltages on overhead lines have shown to impose important variations on the radiated fields in some scenarios [27]. Recently, an induced voltage calculation on a single-wire overhead line was performed in [28] by using also a cone-shaped representation of the mountain and a full-wave solution by using the Finite Element Method (FEM).

This thesis presents the induced voltages calculations for several inhomogeneous and irregular ground propagation paths, not only when the inhomogeneity and irregularity exist nearby the line, but also when they are present under the overhead line by means of a full wave solution based on the FDTD method using a non-regular mesh.

2 Scope of the Thesis

This thesis deals with the problem of the lightning induced voltages on overhead lines in presence of a non-homogeneous and non-uniform ground.

This work is focused on the analysis of the influence of the ground characteristics on the overhead lines over-voltages when a nearby lightning strike occurs. The general objective of this thesis is the evaluation of the influence of a non-homogeneous and non-uniform ground on the lightning induced over-voltages on single-phase overhead lines.

In order to achieve this general objective, this thesis studies several existing approaches for lightning radiated field calculations for medium and long range distances from the lightning channel base; a set of simulation scenarios have been implemented for testing their validity and limitations. Once the methods for calculating lightning induced voltages have been analyzed, the thesis addresses the lightning induced voltages by means of a full wave time-domain solution based on the Finite-Difference Time-Domain method.

The results for lightning induced voltages simulations are presented and discussed for several set-ups in presence of non-homogenous and non-uniform grounds, giving initial conclusions about some of the influences on the lightning induced voltages when more realistic scenarios regarding to ground geometry and electrical parameter variations are represented.

3 The Finite Difference Time-Domain Method for Electromagnetic Fields

The finite-difference time-domain method is in general a discrete approach for solving spatial-temporal differential equations. This method allows solving scalar and vector field equations by means of a recursive scheme in order to find the time and space evolution of a vector field. There are several applications of the FDTD in physics and engineering, although it was primarily applied to electromagnetic fields, it has been also applied to acoustical fields and fluid dynamic problems.

Traditionally, most numerical approaches intended for solving complex electromagnetic problems were based on frequency domain solutions. The frequency response of the problem is calculated for several frequencies by the harmonic representation of the excitation sources and once it is obtained, the inverse Fourier transform is applied in order to find the solution in the time-domain. Using this approach, the inclusion of non-linearities usually requires highly sophisticated implementations. One of the advantages of the FDTD method is that it allows a direct inclusion of time-dependent characteristics on the equations in order to find the time evolution of a vector field.

3.1 Maxwell´s Equations and Electromagnetic Fields

The solution of Maxwell's equations predicts the propagation of the electromagnetic fields produced by a known source through a medium described by its electrical constitutive parameters. These equations relate the electric and magnetic field vectors to their sources under the following spatial-temporal equations (3.1)(3.2)(3.3)(3.4).

$$\nabla \times \vec{E} = -\mu \frac{\partial \vec{H}}{\partial t} \tag{3.1}$$

$$\nabla \cdot \vec{E} = \frac{\rho}{\varepsilon} \tag{3.2}$$

$$\nabla \times \vec{H} = \varepsilon \frac{\partial \vec{E}}{\partial t} + \sigma \vec{E} + \overrightarrow{J_f} \tag{3.3}$$

$$\nabla \cdot \vec{H} = 0 \tag{3.4}$$

where $\vec{E}$ and $\vec{H}$ are the electric and magnetic field intensities; σ, μ and ε are the medium electrical constitutive parameters; ρ corresponds to the volumetric charge density in space and $\overrightarrow{J_f}$ to free conduction current sources present in the media. The electric and magnetic fields are also related by the constitutive equations through electric field density $\vec{D} = \varepsilon \vec{E}$ and the magnetic field density $\vec{B} = \mu \vec{H}$.

3.2 Numerical Solution of the Maxwell´s Equations

The finite-difference time-domain method is a discrete approach to the continuous electromagnetic field formulation presented before, where the electric field components (E_x, E_y, E_z) and the magnetic field components (H_x, H_y, H_z) are located in a staggered fashion over the faces of a cube known as e Yee´s cell [28] as shown in Figure 1. The electrical constitutive parameters are also discretized and related to each field component as (σ_x, σ_y, σ_z), (ε_x, ε_y, ε_z) and (μ_x, μ_y, μ_z). Each cell representing a part of the space is related to a unique location (*i, j, k*) where *i, j* and *k* are integers. These indexes are related to the actual coordinates of each field component, for example, for the x-component of the magnetic field H_x the actual coordinates would be

$$H_x(i,j,k) \rightarrow \big((i-1)\Delta x, (j-0.5)\Delta y, (k-0.5)\Delta z\big) \tag{3.5}$$

where $\Delta x, \Delta y$ and Δz are the lengths of the cell sides.

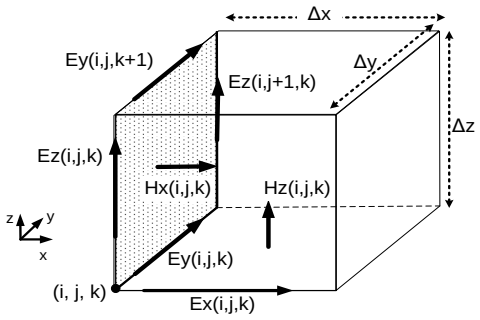

Figure 1 Yee's cell for the electric and magnetic fields location in space.

In vacuum, without any electric charge or current source, the set of equations (3.1)-(3.4) can be reduced to (3.1) and (3.3) as the divergence equations are included in them [30]. When the rotational equations are expanded using a Cartesian coordinate system, it is possible to obtain an equation for the time variation of each component of the electromagnetic field as a function of the spatial variation of its counterpart. This is shown in (3.6) for the x-component of the magnetic field H_x.

$$\frac{\partial H_x}{\partial t} = \frac{1}{\mu_x}\left(\frac{\partial E_y}{\partial z} - \frac{\partial E_z}{\partial y}\right) \tag{3.6}$$

The side of the Yee's cell relating the components of (3.6) is shown dotted in Figure 1. It can be seen that (3.6) relates the time variation of the x-component of the magnetic field as a function of the spatial variations of the electric fields components circulating around it; in this case the *y* and *z* components of E_z and E_y. This distribution is adequate in order to apply a central-difference approximation [30][31][32] to the terms on right hand side of (3.3) resulting in (3.7)

$$\frac{\partial H_x}{\partial t} = \frac{1}{\mu_x}\left(\frac{E^n{}_y(i,j,k+1) - E^n{}_y(i,j,k)}{\Delta z} - \frac{E^n{}_z(i,j+1,k) - E^n{}_z(i,j,k)}{\Delta y}\right) \tag{3.7}$$

The time updating equation for each field component is determined based on a leap-frog scheme as it is shown in Figure 2.

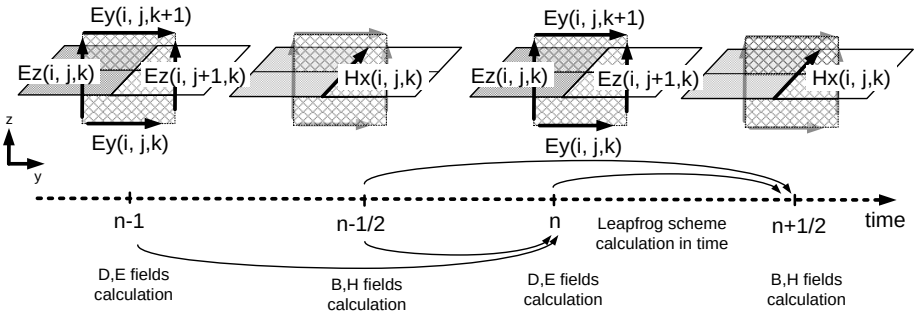

Figure 2 Leapfrog scheme in time for updating electric and magnetic fields.

As it is illustrated, in order to calculate the magnetic field component H_x at the time step *n+1/2*, the information of the electric field at instant *n* and the magnetic field information calculated at *n-1/2* are needed. This means that the magnetic and electric field components are not calculated at the same actual discrete time step; this spatial-time discretization results in a recursive calculation for electric and magnetic field components [28][30]. Applying again a central-difference approach to the time derivative on the left-hand side of (3.6), the x-component magnetic field equation can be written as (3.8):

$$\frac{H_x{}^{n+1/2}(i,j,k) - H_x{}^{n-1/2}(i,j,k)}{\Delta t} = \frac{1}{\mu_x}\left(\frac{E^n{}_y(i,j,k+1) - E^n{}_y(i,j,k)}{\Delta z} - \frac{E^n{}_z(i,j+1,k) - E^n{}_z(i,j,k)}{\Delta y}\right) \tag{3.8}$$

From this, a recursive updating equation can be obtained for H_x. The same analysis can be performed for all six faces on the Yee's cell in order to obtain the complete set of discrete-space equations [28][30][32]. The set of equations (3.9 - 3.14) for all of the electromagnetic components is:

$$\frac{E_x{}^{n+1}(i,j,k) - E_x{}^{n}(i,j,k)}{\Delta t} = \frac{1}{\varepsilon_x}\left(\frac{H_z^{n+1/2}(i,j+1,k) - H_z^{n+1/2}(i,j,k)}{\Delta y} - \frac{H_y^{n+1/2}(i,j,k+1) - H_y^{n+1/2}(i,j,k)}{\Delta z}\right) \tag{3.9}$$

$$\frac{E_y{}^{n+1}(i,j,k) - E_y{}^{n}(i,j,k)}{\Delta t} = \frac{1}{\varepsilon_y}\left(\frac{H_x^{n+1/2}(i,j,k+1) - H_x^{n+1/2}(i,j,k)}{\Delta z} - \frac{H_z^{n+1/2}(i+1,j,k) - H_z^{n+1/2}(i,j,k)}{\Delta x}\right) \tag{3.10}$$

$$\frac{{E_z}^{n+1}(i,j,k)-{E_z}^{n}(i,j,k)}{\Delta t}=\frac{1}{\varepsilon_z}\left(\frac{H_y^{n+1/2}(i+1,j,k)-H_y^{n+1/2}(i,j,k)}{\Delta x}-\frac{H_x^{n+1/2}(i,j+1,k)-H_x^{n+1/2}(i,j,k)}{\Delta y}\right) \quad (3.11)$$

$$\frac{{H_x}^{n+1/2}(i,j,k)-{H_x}^{n-1/2}(i,j,k)}{\Delta t}=\frac{1}{\mu_x}\left(\frac{{E^n}_y(i,j,k+1)-{E^n}_y(i,j,k)}{\Delta z}-\frac{{E^n}_z(i,j+1,k)-{E^n}_z(i,j,k)}{\Delta y}\right) \quad (3.12)$$

$$\frac{{H_y}^{n+1/2}(i,j,k)-{H_y}^{n-1/2}(i,j,k)}{\Delta t}=\frac{1}{\mu_y}\left(\frac{{E^n}_z(i+1,j,k)-{E^n}_z(i,j,k)}{\Delta x}-\frac{{E^n}_x(i,j,k+1)-{E^n}_x(i,j,k)}{\Delta z}\right) \quad (3.13)$$

$$\frac{{H_z}^{n+1/2}(i,j,k)-{H_z}^{n-1/2}(i,j,k)}{\Delta t}=\frac{1}{\mu_z}\left(\frac{{E^n}_x(i,j+1,k)-{E^n}_x(i,j,k)}{\Delta y}-\frac{{E^n}_y(i+1,j,k)-{E^n}_y(i,j,k)}{\Delta x}\right) \quad (3.14)$$

3.3 Numerical Stability Criteria

In this section the numerical stability criteria is defined in order to determine the limits of minimal time and space discretization. Consider a one-dimensional wave propagating along the x-axis in the vacuum. As it has been shown, the wave-equation can be written for one-dimension as (3.15):

$$\frac{\partial^2 F}{\partial x^2}=\frac{1}{{C_0}^2}\frac{\partial^2 F}{\partial t^2} \quad (3.15)$$

where F represents any of the electromagnetic field components. This one-dimensional wave-equation can be described by means of two waves traveling in opposite directions as [30]

$$\left(\frac{\partial F}{\partial x}-\frac{1}{C_0}\frac{\partial F}{\partial t}\right)\left(\frac{\partial F}{\partial x}+\frac{1}{C_0}\frac{\partial F}{\partial t}\right)=0 \quad (3.16)$$

Now, taking the wave traveling in the negative x-direction (3.17) and applying a central difference approximation [30][31], a time-space discrete equation can be obtained as shown in (3.18):

$$\frac{\partial F_x}{\partial x}=\frac{1}{C_0}\frac{\partial F}{\partial t} \quad (3.17)$$

$$\frac{F_{x+\Delta x/2}^{n}-F_{x-\Delta x/2}^{n}}{\Delta x}=\frac{1}{C_0}\frac{F_x^{n+\Delta t/2}-F_x^{n-\Delta t/2}}{\Delta t} \quad (3.18)$$

Rearranging (3.18), a numerical scheme in order to find the time-evolution of the field under calculation can be written as (3.19):

$$F_x^{n+\Delta t/2}=F_x^{n-\Delta t/2}+\lambda\left(F_{x+\Delta x/2}^{n}-F_{x-\Delta x/2}^{n}\right) \quad (3.19)$$

where, $\lambda = C_0 \Delta t / \Delta x$.

It can be shown that depending on the factor λ value, the recursive updating equation presented above is stable if $\lambda \leq 1$. Then,

$$C_0 \frac{\Delta t}{\Delta x} \leq 1 \tag{3.20}$$

The expression above allows defining the time-step value for stable calculations. Using an attenuation factor, expression (3.20) can be written as (3.21)

$$\Delta t = C_f \frac{1}{C_0} \Delta x \tag{3.21}$$

where, C_f is an attenuating factor used for maintaining a reasonable quantization error. The same numerical stability condition can be found for the three dimensional wave equation as [30][31][32]:

$$\Delta t = C_f \frac{1}{C_0 \sqrt{\frac{1}{(\Delta x)^2} + \frac{1}{(\Delta y)^2} + \frac{1}{(\Delta z)^2}}} \tag{3.22}$$

If the spatial discretization is made by cubic cells $\Delta x = \Delta y = \Delta z = \Delta s$ the stability criteria can be simplified to [31][32]:

$$\Delta t = C_f \frac{\Delta s}{C_0 \sqrt{3}} \tag{3.23}$$

where Δs is the cell side length. In general, $C_f \leq 1$ and it is typically set to be 0.9 for FDTD simulations. This factor is known as the Courant's factor. The relations that have been presented here are illustrative, a more rigorous determination of the Courant's factor can be found in [30].

3.4 Media Modeling

As the electrical constitutive parameters of the medium are directly related to their electric and magnetic field components, the FDTD approach allows a straightforward inclusion of any material and medium representation. As it was shown in section 3.2, the electrical constitutive parameters are also discretized and related to each field component as (σ_x, σ_y, σ_z), (ε_x, ε_y, ε_z) and (μ_x, μ_y, μ_z). In order to describe the constitutive parameter location into the Yee's cube, some of the constitutive parameters components are shown in Figure 3.

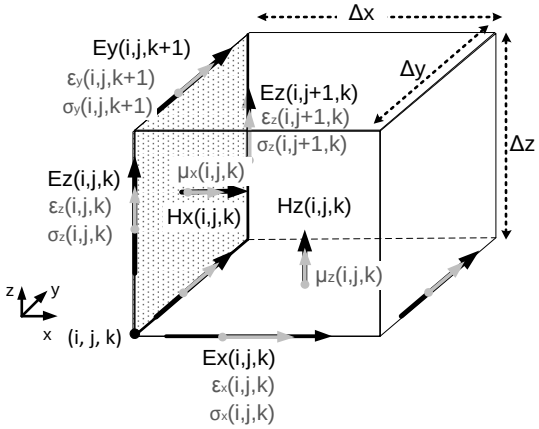

Figure 3 Material Inclusion into the Yee's Cell

In order to include the complete set of Maxwell's equation into the FDTD method, the equations (3.1)-(3.4) are expanded as:

$$\frac{\partial E_x}{\partial t} = \frac{1}{\varepsilon_x}\left(\frac{\partial H_z}{\partial y} - \frac{\partial H_y}{\partial z} - \sigma_x E_x - J_{fx}\right) \tag{3.24}$$

$$\frac{\partial E_y}{\partial t} = \frac{1}{\varepsilon_y}\left(\frac{\partial H_x}{\partial z} - \frac{\partial H_z}{\partial x} - \sigma_y E_y - J_{fy}\right) \tag{3.25}$$

$$\frac{\partial E_z}{\partial t} = \frac{1}{\varepsilon_z}\left(\frac{\partial H_y}{\partial x} - \frac{\partial H_x}{\partial y} - \sigma_z E_z - J_{fz}\right) \tag{3.26}$$

$$\frac{\partial H_x}{\partial t} = \frac{1}{\mu_x}\left(\frac{\partial E_y}{\partial z} - \frac{\partial E_z}{\partial y}\right) \tag{3.27}$$

$$\frac{\partial H_y}{\partial t} = \frac{1}{\mu_y}\left(\frac{\partial E_z}{\partial x} - \frac{\partial E_x}{\partial z}\right) \tag{3.28}$$

$$\frac{\partial H_z}{\partial t} = \frac{1}{\mu_z}\left(\frac{\partial E_x}{\partial y} - \frac{\partial E_y}{\partial x}\right) \tag{3.29}$$

The new term present in the components equations of the electric field, which is related to the conductivity of the media must be included carefully. As it was described in the leap-frog scheme in Figure 2, the central difference discretization used to find the time-updating equations scheme implies the calculation of the fields on the right side of the equations (3.24)-(3.29) at a time step located between the time steps of the left side components. The expression (3.30) shows the discretization of equation (3.29) using the central difference approach [28][30][31][32]:

$$\frac{{E_x}^{n+1}(i,j,k) - {E_x}^{n}(i,j,k)}{\Delta t} = \frac{1}{\varepsilon_x}\left(\frac{H_z^{n+1/2}(i,j+1,k) - H_z^{n+1/2}(i,j,k)}{\Delta y} - \frac{{H_y}^{n+\frac{1}{2}}(i,j,k+1) - {H_y}^{n+\frac{1}{2}}(i,j,k)}{\Delta z} - \sigma_x(i,j,k){E_x}^{n+\frac{1}{2}}(i,j,k) - {J_{fx}}^{n+\frac{1}{2}}(i,j,k)\right) \tag{3.30}$$

As the electric field component at the *n+1/2* time step is not calculated by means of the time-updating equation, an average of this electric field must be performed with those components calculated at the *n* and *n+1* time-steps as is shown in (3.31):

$$E_x{}^{n+\frac{1}{2}}(i,j,k) = \frac{E_x{}^{n+1}(i,j,k) + E_x{}^{n}(i,j,k)}{2} \tag{3.31}$$

Replacing (3.31) in (3.30) and rearranging some terms, a time-updating equation for the electric field component under analysis can be found as is presented in (3.32). The time-updating equations for the other electric field components can be found similarly [28][30][31][32]. As the equations of the magnetic field components have not been modified by any new term, their time-update equations remain unaltered as those presented in section 3.1.

$$\begin{aligned} E_x{}^{n+1}(i,j,k) = {} & \left(\frac{2\varepsilon_x(i,j,k) - \Delta t\sigma_x(i,j,k)}{2\varepsilon_x(i,j,k) + \Delta t\sigma_x(i,j,k)}\right) E_x{}^{n}(i,j,k) \\ & + \frac{2\Delta t}{2\varepsilon_x(i,j,k) + \Delta t\sigma_x(i,j,k)}\left(\frac{H_z^{n+1/2}(i,j+1,k) - H_z^{n+1/2}(i,j,k)}{\Delta y}\right) \\ & - \frac{2\Delta t}{2\varepsilon_x(i,j,k) + \Delta t\sigma_x(i,j,k)}\left(\frac{H_y^{n+\frac{1}{2}}(i,j,k+1) - H_y^{n+\frac{1}{2}}(i,j,k)}{\Delta z}\right) \\ & - \frac{2\Delta t}{2\varepsilon_x(i,j,k) + \Delta t\sigma_x(i,j,k)} J_{fx}{}^{n+\frac{1}{2}}(i,j,k) \end{aligned} \tag{3.32}$$

As can be seen, the media parameter inclusion can be performed easily into the FDTD method if the geometrical shape of the material coincides with a straight or parallelepipedal geometry. If this is not the case, different techniques such as subcell models can be used in order to represent curved geometrical features [30].

3.5 Lumped Elements Modeling

As it has been shown in the previous sections, the FDTD method uses a relation between the electric and magnetic fields and the media parameters when they are located at specific places in a cube cell. Based on this, it is possible to calculate the evolution in time of an electromagnetic simulation scenario if the magnitude of any component of the electric or magnetic field is imposed at some point. Lumped elements, such as sources, resistors, capacitors, inductors and non-linear elements can be included into the FDTD method by means of the voltage-current relation between their terminals. Equations (3.24) and (3.25) present the integral expression relating the voltage and current magnitudes with the electric field and current density respectively [31].

Voltage and Electric Field relation

$$\Delta V = -\int_l \vec{E}\overrightarrow{dl} \tag{3.33}$$

Current and density Current relation

$$I = \iint_s \overrightarrow{J_f}.\overrightarrow{ds} \tag{3.34}$$

Any lumped component represented by means of it voltage-current relation can be included into the FDTD scheme through the impressed current density term $\overrightarrow{J_f}$ in the Ampère-Maxwell equation (3.26):

$$\nabla \times \vec{H} = \varepsilon \frac{\partial \vec{E}}{\partial t} + \sigma \vec{E} + \overrightarrow{J_f} \tag{3.35}$$

Care must be taken as the voltage must be calculated in the same discrete time *n* as the electric field, and the current must be also calculated as the same discrete time *n+1/2* for the magnetic field as:

$$\Delta V^n = \Delta z {E_z}^n \tag{3.36}$$

$$J^{n+1/2} = \frac{1}{\Delta x \Delta y} I^{n+1/2} \tag{3.37}$$

Taking into account the equations (3.36) and (3.37) any voltage-current relation can be included into the Yee´s cell and into the FDTD scheme in different convenient ways. Following subsections show how to include different lumped elements such as sources and loads starting from their voltage-current relation. All of the lumped elements that have been considered for illustration have been placed in the z-direction.

3.5.1 Sources Modeling

Voltage and current sources are useful to model several electromagnetic problems, especially for several engineering applications where the electromagnetic fields are generated by sophisticated physical arrangements that depending on the simplifications and approximations, can be reduced to this kind of representation. These elements can be included into the FDTD by means of the imposition of a time-varying function on a component of the electric or magnetic field using the physical relation between the fields and the voltage-current characteristic [30][31].

Consider a voltage source having an internal impedance different of zero placed between two z-directed nodes of the Yee´s cube as is shown in Figure 4(a).

Figure 4 Source Modeling into the Yee´s Cell (a) Lumped Voltage Source with non-zero internal impedance (b) Current Source

The lumped voltage source can be related to the vertical electric field component between the two nodes in the time domain by means of the expression:

$$V_s(t) - I(t)R_s = E_z(t)\Delta z \tag{3.38}$$

As it was explained before, the most convenient time-discretization for the expression (3.38) can be written as:

$$V_s{}^n - I^n R_s = E_z{}^n \Delta z \tag{3.39}$$

As the current at the discrete instant *n* (I^n) is not calculated explicitly in the recursive FDTD scheme, its average is used:

$$I^n = \frac{I^{n-1/2} + I^{n+1/2}}{2} \tag{3.40}$$

Replacing (3.40) into (3.39) the expression for the voltage source with internal resistance can be written as:

$$V_s{}^n - \left(I^{n-1/2} + I^{n+1/2}\right)\frac{R_s}{2} = E_z{}^n \Delta z \tag{3.41}$$

Rearranging equation (3.41) and using (3.34), the lumped source expression can be written as:

$$J^{n+1/2} = -J^{n-1/2} - \frac{2}{\Delta x \Delta y R_s}(E_z{}^n \Delta z + V_s{}^n) \tag{3.42}$$

If the source to be modeled has zero internal resistance, then the voltage time-varying voltage source into the FDTD method can be included as

$$E_z{}^n = \frac{V_s{}^n}{\Delta z} \tag{3.43}$$

In order to include a lumped current source, the expression (3.34) applied to a side of the Yee's cube leads to (3.44).

$$J_z{}^{n+1/2} = \frac{1}{\Delta x \Delta y} I_s{}^{n+1/2} \tag{3.44}$$

As it is shown in Figure 4(b) the current between the two nodes can be directly related to the current density.

3.5.2 Resistor

Consider a resistor element placed between two z-directed nodes of the Yee´s cell as it is shown in Figure 5.

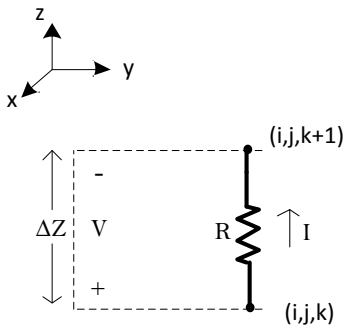

Figure 5 Resistor Modeling into the Yee´s Cell

For a resistor, the relation between current and voltage in the time domain can be written as:

$$I(t) = \frac{V(t)}{R} \tag{3.45}$$

Using the discrete-time relation at the time instant *n+1/2* the following relation can be found:

$$I^{n+1/2} = \frac{V^{n+1/2}}{R} \tag{3.46}$$

As the voltage cannot be calculated at the discrete time *n+1/2*, the same time average approach presented before for the voltage source can be applied here for the voltages:

$$V^{n+1/2} = \frac{\Delta V^{n+1} + \Delta V^{n}}{2} \tag{3.47}$$

Using this result, the current calculation for the discrete-time *n+1/2* can be written as:

$$I^{n+1/2} = \frac{{E_z}^{n+1} + {E_z}^{n}}{2R}\Delta z \tag{3.48}$$

Finally, the current density can be calculated by means of the following expression allowing the inclusion of the resistor into the FDTD scheme:

$$J^{n+1/2} = \frac{\Delta z}{2R\Delta x\Delta y}\left[{E_z}^{n+1} + {E_z}^{n}\right] \tag{3.49}$$

3.5.3 Inductor

Consider a lumped inductor placed between two z-directed nodes of the Yee´s cell as it is shown in Figure 6

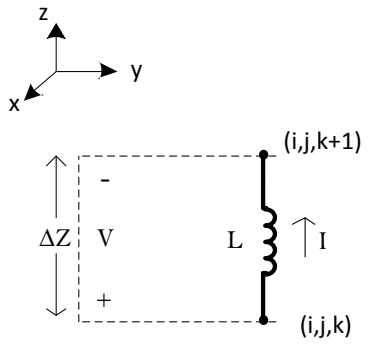

Figure 6 Inductor Modeling into the Yee´s Cell

The voltage-current relation through the element involves a time-derivative operator over the current time-varying function given by:

$$V(t) = L\frac{dI}{dt} \tag{3.50}$$

A central finite-difference approach can be included in order to calculate the voltage between the two terminals as:

$$V^n = L\left(\frac{I^{n+1/2} - I^{n-1/2}}{\Delta t}\right) \tag{3.51}$$

Using this central approach and rearranging the expression, the current density at that cell due to the presence of the inductor can be carried out by the following expression:

$$J^{n+1/2} = J^{n-1/2} + \frac{\Delta t\Delta z}{\Delta x\Delta yL}{E_z}^{n} \tag{3.52}$$

3.5.4 Capacitor

Consider a capacitor placed between two z-directed nodes of the Yee´s cell as it is shown in Figure 7.

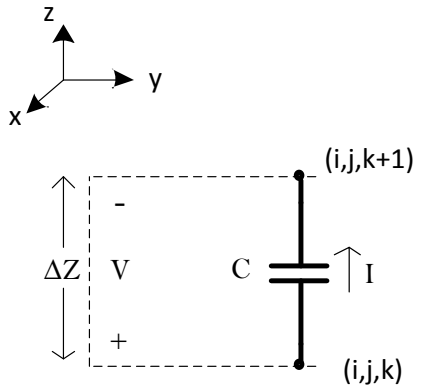

Figure 7 Capacitor Modeling into the Yee´s Cell

For a capacitor, the voltage-current relation involves a time-derivative operator on the voltage given by:

$$I(t) = C\frac{dV}{dt} \tag{3.53}$$

The most convenient discrete-time relation for the current through the capacitor must be calculated at the instance *n+1/2*:

$$I^{n+1/2} = C\frac{V^{n+1} - V^{n}}{\Delta t} \tag{3.54}$$

As the expression (3.54) relates voltage terms calculated at the same time-steps as the electric field components in the FDTD method, the current density equation is:

$$J^{n+1/2} = \frac{C\Delta Z}{\Delta x \Delta y \Delta t}\left[{E_z}^{n+1} - {E_z}^{n}\right] \tag{3.55}$$

3.5.5 Series RL load

This lumped element is composed by a resistor and an inductor connected in series and located at the same spatial point. In order to be included into the FDTD equations, a relation between the

electric and magnetic fields must take into account the effect of the series inductive and resistive load. Consider a lumped resistor in series with an inductor placed between two z-directed nodes of the Yee´s cell as it is shown in Figure 8.

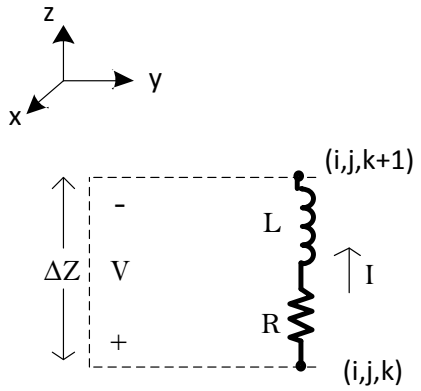

Figure 8 Lumped RL-Load Modeling into the Yee´s Cell

The equation that relates the voltage and current for the series RL-lumped element can be written as:

$$V(t) = I(t)R + L\frac{dI}{dt} \tag{3.56}$$

In order to include the series RL-lumped element into the FDTD scheme, the discretization can be done as it was presented for the resistor and the inductor. The most convenient formulation can be written as:

$$V^n = R\left(\frac{I^{n+1/2} + I^{n-1/2}}{2}\right) + L\left(\frac{I^{n+1/2} - I^{n-1/2}}{\Delta t}\right) \tag{3.57}$$

Using the expression for the voltage calculation by means of the electric field and rearranging expression (3.57), it can be obtained (3.58):

$$I^{n+1/2} = \frac{(R\Delta t - 2L)}{(R\Delta t + 2L)} I^{n-1/2} - \frac{\Delta z}{(R\Delta t + 2L)} {E_z}^n \tag{3.58}$$

Finally, using equation (3.58) and expressing in terms of the current-density, it can be shown:

$$J^{n+1/2} = \frac{(R\Delta t - 2L)}{(R\Delta t + 2L)} J^{n-1/2} - \frac{\Delta z}{\Delta x \Delta y (R\Delta t + 2L)} {E_z}^n \tag{3.59}$$

3.5.6 Parallel RC load

Consider a RC lumped element placed between two z-directed nodes of the Yee´s cell, as it is shown in Figure 9.

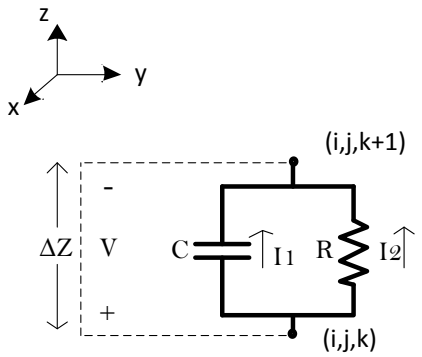

Figure 9 Parallel RC-lumped Load into the Yee´s Cell

The current through a parallel RC circuit can be written as the sum of each branch current by means of the current Kirchhoff's law as:

$$I(t) = \frac{V(t)}{R} + C\frac{dV}{dt} \tag{3.60}$$

Equation (3.60) can be written at the *n+1/2* time-step for convenience leading to:

$$I^{n+1/2} = {I_c}^{n+1/2} + {I_r}^{n+1/2} \tag{3.61}$$

As both currents ${I_r}^{n+1/2}$ and ${I_c}^{n+1/2}$ were previously calculated for the resistor and the capacitor in section 3.5.2 and section 3.5.4 respectively, the lumped RC element can be described using the same results described in the above sections:

$$I^{n+1/2} = \frac{C\Delta Z}{\Delta t}\left[{E_z}^{n+1} - {E_z}^{n}\right] + \frac{{E_z}^{n+1} + {E_z}^{n}}{2R}\Delta Z \tag{3.62}$$

Finally, the equation for the current density can be written as:

$$J^{n+1/2} = \frac{\Delta Z}{\Delta X \Delta Y}\left[\frac{C}{\Delta t} + \frac{1}{2R}\right]{E_z}^{n+1} + \frac{\Delta Z}{\Delta X \Delta Y}\left[\frac{1}{2R} - \frac{C}{\Delta t}\right]{E_z}^{n} \tag{3.63}$$

3.6 Boundary Conditions

As it has been presented above, the FDTD method produces a recursive scheme for calculating magnetic and electric field including not only the material properties but also different lumped elements. The relations derived before have been presented for a general discrete point *(i,j,k)* inside the problem space.

In all cases, the problem space must be represented by a finite computational domain composed by a finite number of Yee´s cubes. Some of those cubes will have all of their components located inside the computational volume making their electric and magnetic field possible to be calculated using the surrounding components from contiguous cubes [30][31]. When one of the Yee´s cube coincides with the boundary of the computational domain, some of the field components cannot be calculated by surrounding fields as some of them are out of the domain. Figure 10 depicts this situation when the vertical electric field component located at the 2D boundary must be calculated based on the surrounding components. As can be seen from Figure 10, all the vertical electric field components that are located inside the domain can be calculated using the central difference approach by means of the surrounding magnetic fields. However, when the electric field is at the boundary, there are magnetic field components outside the computational domain which are not available for the calculation.

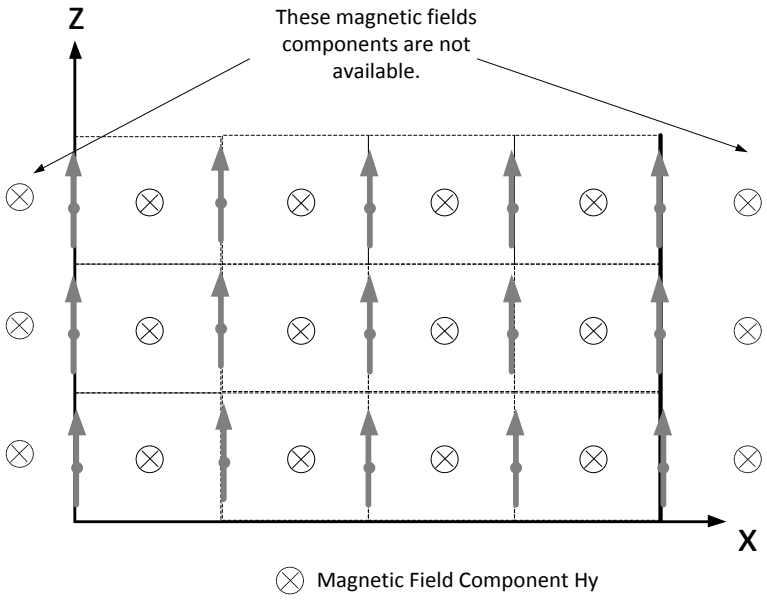

Figure 10 Electric Field Components calculation at the Boundary of the Computational Domain

In order to overcome this problem, several methods have been proposed in literature for calculating the components of the electromagnetic field at the boundary based on its past values and available components located inside the domain. Typically, the boundary conditions are applied to the electric field components because they can be easily related to physical conditions (i.e. when perfectly conductive planes are present). However, boundary conditions can be also applied for magnetic field components placed on the boundary [30]. In this thesis all the boundaries conditions were implemented for the electric field components.

3.6.1 Perfectly Conductive Boundary Condition

This boundary condition assumes that the boundaries of the computational domain are perfect conductors with zero thickness [28][30][31]. This assumption allows defining the electric field components as inside a perfect conductor, therefore they are forced to be zero. These boundaries are commonly named as Perfect Electric Conductor or "PEC" Boundaries.

A computational set up was proposed in order to evaluate the PEC implementation into the FDTD scheme. The total domain was simulated using 50x24x10 cubic cells; each cube was simulated with a side of 2mm in length. The source was represented by means of an array of vertical electric field components with the same waveform; it is worth noting that all of the sources were imposed with no phase delay between each other in order to control the symmetry of the radiated wave propagation. The vertical source array was placed at (26, 13) on the XY plane and extended along the Z axis; the electric field measured was located at the node (33, 13, 5). Figure 11(a) presents the simulation set-up.

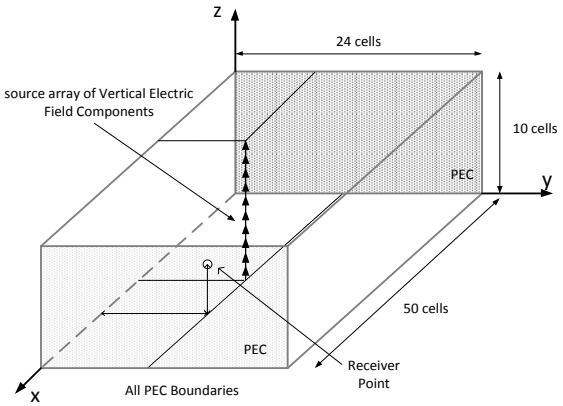

(a)

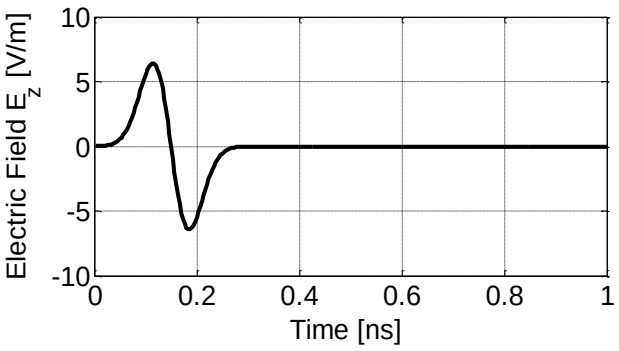

(b)

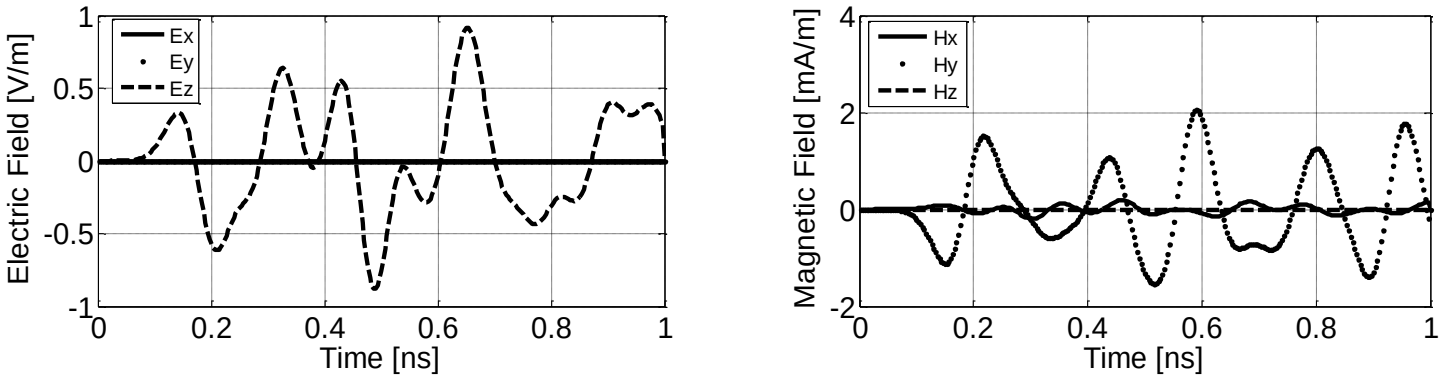

(c) (d)

Figure 11 (a) Simulation Set-up for PEC Boundaries Implementation (b) Source Waveform (c) Electric Field Magnitudes for each component at the Receiver Point (d) Magnetic Field magnitudes for each component at the Receiver Point

Figure 11(b) shows the source waveform used in the simulation set-up. This waveform known as the *normalized derivative Gaussian waveform* and is commonly used for the excitation of a wide frequency spectrum without taking into account very low frequency components [31].

Despite the excitation vanishes once the bipolar pulse ends, the electromagnetic field components showed in Figure 11(c) and Figure 11(d) present an oscillatory pattern for the entire time interval. These patterns are caused by the multiple reflections of the electromagnetic wave on the boundaries. An infinite oscillatory steady-state will be reached and most of the resonance characteristics of the cavity can be analyzed from the time solution.

3.6.2 Absorbing Boundaries Conditions

PEC boundaries are useful when perfectly conductive thin layers must be included into the simulation. However, several applications require that the boundaries act as an open space, meaning that no reflections of the incident waves are desired. This section presents some of the most popular boundary conditions that have been proposed in literature for non-reflecting characteristics at the boundary of the computational domain. All of these boundaries are based on known values taken from the internal domain, leading to a set of updating equations for the electric field components at the boundary.

3.6.2.1 Mur´s Boundaries

The Mur´s Boundaries conditions are based on the plane-wave unbounded propagation characteristics [33]. The wave equation for any component of the electromagnetic field can be written as:

$$\nabla^2 F = \frac{1}{{C_0}^2}\frac{\partial^2 F}{\partial t^2} \tag{3.64}$$

where F, represents any component of the electromagnetic field and C_0 is the propagation velocity. Using rectangular coordinates:

$$\left(\frac{\partial^2}{\partial x^2}+\frac{\partial^2}{\partial y^2}+\frac{\partial^2}{\partial z^2}\right)F-\frac{1}{{C_0}^2}\frac{\partial^2 F}{\partial t^2}=0 \tag{3.65}$$

Along the x-axis, expression (3.65) can be rearranged as in (3.66).

$$\left(\frac{\partial^2}{\partial x^2}\right)F=\frac{1}{{C_0}^2}\frac{\partial^2 F}{\partial t^2}-\left(\frac{\partial^2}{\partial y^2}+\frac{\partial^2}{\partial z^2}\right)F \tag{3.66}$$

Figure 12 shows a geometric interpretation about the boundary condition based on a one-way propagation wave along the x-axis.

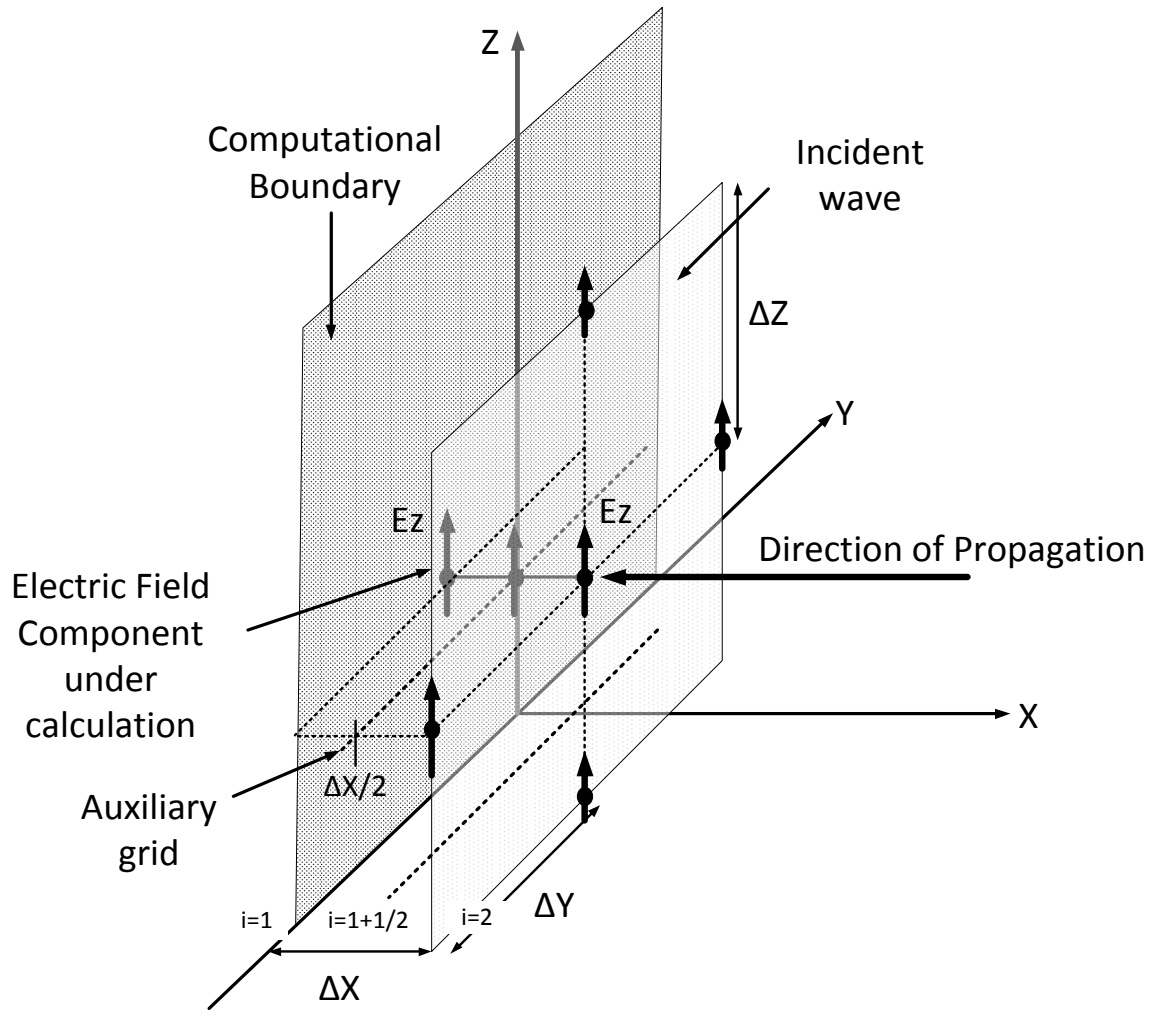

Figure 12 Geometric Interpretation of an incident wave for the Mur's Boundary Conditions derivation

From Figure 12, an area ΔYΔZ is taken into account as a part of the wave front reaching the boundary. The vertical electric field component at the boundary can be related to the spatial variation of the field on the wave front segment and its time variation, by means of the expression (3.66) evaluated at the auxiliary grid located at ΔX/2.

In order to obtain an explicit time-updating equation for the components at the boundary, expression (3.66) can be rearranged as:

$$\left(\frac{\partial^2}{\partial x^2}\right)F = \frac{1}{{C_0}^2}\frac{\partial^2}{\partial t^2}\left(1 - \left(\frac{\frac{\partial^2}{\partial y^2} + \frac{\partial^2}{\partial z^2}}{\frac{\partial^2}{\partial t^2}}\right)\right)F \tag{3.67}$$

Defining,

$$S^2 = \left(\frac{\frac{\partial^2}{\partial y^2} + \frac{\partial^2}{\partial z^2}}{\frac{\partial^2}{\partial t^2}}\right) \tag{3.68}$$

and replacing (3.68) in (3.67) yields to:

$$\left(\frac{\partial^2}{\partial x^2}\right)F - \frac{1}{{C_0}^2}\left(\frac{\partial^2}{\partial t^2}(1 - S^2)\right)F \tag{3.69}$$

By means of the derivative operator properties, the wave equation can be factorized as [30]:

$$\left(\frac{\partial}{\partial x} - \frac{1}{C_0}\frac{\partial}{\partial t}\sqrt{1 - S^2}\right)\left(\frac{\partial}{\partial x} + \frac{1}{C_0}\frac{\partial}{\partial t}\sqrt{1 - S^2}\right) = 0 \tag{3.70}$$

The boundary condition now can be applied depending on the direction of the incident wave. If the field component in the x-direction F_x is assumed to be a plane unidirectional wave traveling in the negative direction of the x-axis, the boundary condition can be calculated for the left term of the equation above as:

$$\left(\frac{\partial}{\partial x} - \frac{1}{C_0}\frac{\partial}{\partial t}\sqrt{1 - S^2}\right) = 0 \tag{3.71}$$

The imperfection of the absorbing characteristics rises from the discretization of equation (3.71). Engquist and Majda [34] proposed an expansion of the $\sqrt{1 - S^2}$ term using Taylor series and leading to different approximations for the numerical simulation of incident waves depending on the number of terms taken into account [30].

Mur, proposed a discrete approach for equation (3.71) and a Taylor series representation based on a finite central difference approximation, in order to represent the boundary condition using

the same scheme of the FDTD method. The first order Mur´s boundary condition can be derived if the spatial derivatives terms are disregarded. The expression (3.71) can be simplified to

$$\left(\frac{\partial}{\partial x}-\frac{1}{C_0}\frac{\partial}{\partial t}\right)=0 \tag{3.72}$$

Consider the incident wave of the vertical electric field component as shown in Figure 12. Applying the derivative operator (3.72) to the field component under analysis it can be obtained that:

$$\frac{\partial F_z}{\partial x}=\frac{1}{C_0}\frac{\partial F_z}{\partial t} \tag{3.73}$$

Applying the central difference approach to (3.73) yields to:

$$\frac{F_z^n(2,j,k)-F_z^n(1,j,k)}{\Delta x}=\frac{1}{C_0}\left(\left.\frac{\partial F_z}{\partial t}\right|_{(1+1/2,j,k)}\right) \tag{3.74}$$

As the central difference approach is performed at an auxiliary grid $i=1+1/2$, it is not included directly into the FDTD scheme presented in section 3.1. The derivative value at $i=1+1/2$ can be averaged using known derivative values as:

$$\left.\frac{\partial F_z}{\partial t}\right|_{(1+1/2,j,k)}=\frac{1}{2}\left(\left.\frac{\partial F_z}{\partial t}\right|_{(1,j,k)}+\left.\frac{\partial F_z}{\partial t}\right|_{(2,j,k)}\right) \tag{3.75}$$

Applying a central difference approach to each term and replacing in (3.74), a time updating equation can be written for the field component under analysis [30]:

$$F_z^{n+1}(1,j,k)=F_z^n(2,j,k)+\frac{C_0\Delta t-\Delta x}{C_0\Delta t+\Delta x}\left(F_z^{n+1}(2,j,k)-F_z^n(1,j,k)\right) \tag{3.76}$$

The result presented in (3.76) can be extended to the rest of the components and directions of the propagating traveling wave.

If the Taylor´s series is again applied for representing the expression $\sqrt{1-S^2}$, and two terms of the expansion are taken into account, a better representation of the incident wave can be obtained:

$$\sqrt{1-\left(\frac{\frac{\partial^2}{\partial y^2}+\frac{\partial^2}{\partial z^2}}{\frac{\partial^2}{\partial t^2}}\right)}\approx 1-\frac{1}{2}\left(\frac{\frac{\partial^2}{\partial y^2}+\frac{\partial^2}{\partial z^2}}{\frac{\partial^2}{\partial t^2}}\right) \tag{3.77}$$

Replacing (3.77) in (3.71) and rearranging the equation we find:

$$\frac{\partial^2}{\partial t \partial x} - \frac{1}{C_0}\frac{\partial^2}{\partial t^2} + \frac{1}{2C_0}\left(\frac{\partial^2}{\partial y^2} + \frac{\partial^2}{\partial z^2}\right) = 0 \tag{3.78}$$

Using a central difference approach for discretizing the differential equation in space and time, the second order Mur's boundaries can be found. For this case the discretization leads to a second order derivative discrete equation. Again, the central difference approach is used at the auxiliary grid presented in Figure 12. As the auxiliary grid is not explicit in the FDTD scheme presented in section 3.1, the second order time derivative can be calculated as an average between the time derivative of the adjacent points (3.80) and for the space-second order derivatives (3.81)-(3.82):

$$\left.\frac{\partial^2}{\partial t \partial x}\right|_{(1+1/2,j,k)} = \frac{\partial}{\partial t}\left(\frac{\partial}{\partial x}\right) = \frac{1}{2\Delta t}\left(\left.\frac{\partial}{\partial x}\right|^{n+1}_{(1+1/2,j,k)} - \left.\frac{\partial}{\partial x}\right|^{n-1}_{(1+1/2,j,k)}\right) \tag{3.79}$$

$$\left.\frac{\partial^2}{\partial t^2}\right|^{n}_{(1+1/2,j,k)} = \frac{1}{2}\left(\left.\frac{\partial^2}{\partial t^2}\right|^{n}_{(1,j,k)} + \left.\frac{\partial^2}{\partial t^2}\right|^{n}_{(2,j,k)}\right) \tag{3.80}$$

$$\left.\frac{\partial^2}{\partial y^2}\right|^{n}_{(1+1/2,j,k)} = \frac{1}{2}\left(\left.\frac{\partial^2}{\partial y^2}\right|^{n}_{(1,j,k)} + \left.\frac{\partial^2}{\partial y^2}\right|^{n}_{(2,j,k)}\right) \tag{3.81}$$

$$\left.\frac{\partial^2}{\partial z^2}\right|^{n}_{(1+1/2,j,k)} = \frac{1}{2}\left(\left.\frac{\partial^2}{\partial z^2}\right|^{n}_{(1,j,k)} + \left.\frac{\partial^2}{\partial z^2}\right|^{n}_{(2,j,k)}\right) \tag{3.82}$$

Applying the central differences and replacing in (3.78), an expression for the unknown field at the boundary can be found in function of the inner field values as [30][33]:

$$\begin{aligned} F_z^{n+1}(1,j,k) = &-F_z^{n-1}(2,j,k) + \frac{C_0\Delta t - \Delta x}{C_0\Delta t + \Delta x}\left(F_z^{n+1}(2,j,k) + F_z^{n-1}(1,j,k)\right) \\ &+ \frac{2\Delta x}{C_0\Delta t + \Delta x}\left(F_z^{n}(2,j,k) + F_z^{n}(1,j,k)\right) \\ &+ \frac{(C_0\Delta t)^2\Delta x}{2\Delta y^2(C_0\Delta t + \Delta x)}\begin{pmatrix} F_z^n(2,j+1,k) - 2F_z^n(2,j,k) + F_z^n(2,j-1,k) \\ +F_z^n(1,j+1,k) - 2F_z^n(1,j,k) + F_z^n(1,j-1,k)\end{pmatrix} \\ &+ \frac{(C_0\Delta t)^2\Delta x}{2\Delta z^2(C_0\Delta t + \Delta x)}\begin{pmatrix} F_z^n(2,j,k+1) - 2F_z^n(2,j,k) + F_z^n(2,j,k-1) \\ +F_z^n(1,j,k+1) - 2F_z^n(1,j,k) + F_z^n(1,j,k-1)\end{pmatrix} \end{aligned} \tag{3.83}$$

The expression presented in (3.83) can be also derived for the remaining components. In order to validate the implementation of the Mur´s boundaries in the FDTD formulation presented in this thesis, Figure 13 shows the comparison between the results obtained by the implementation of the Mur's boundaries in this thesis with those results presented in [33]. The simulation set-up consisted of a vertical current dipole with a harmonic excitation of wavelength λ. The current dipole was located at the coordinate (5λ, 5λ) on the XY plane. A contour plot of this field component is obtained from XY plane values.

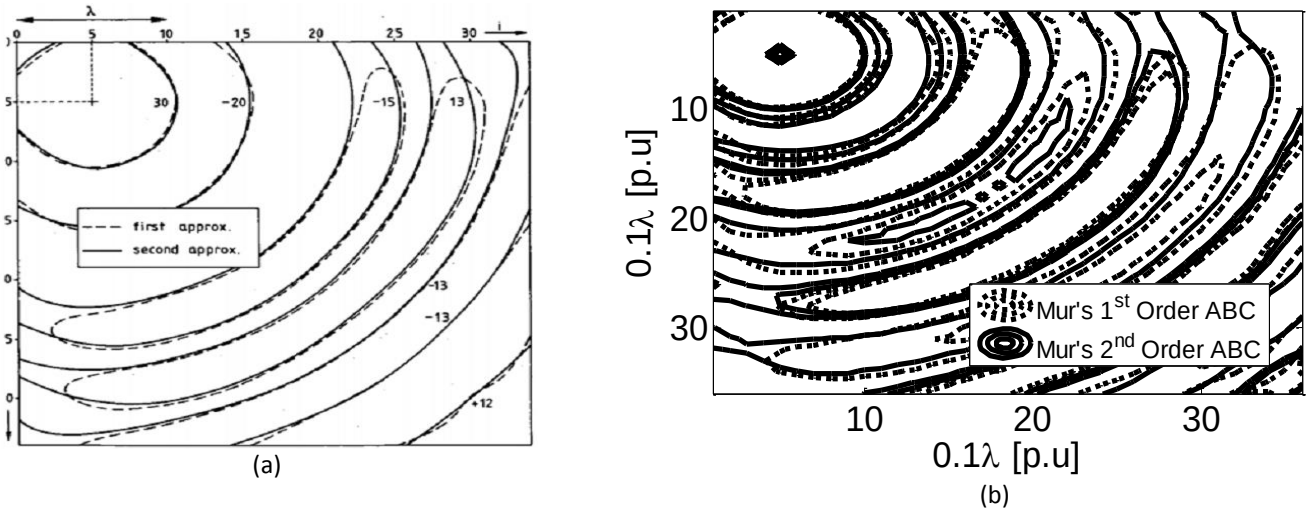

(a) (b)

Figure 13 Vertical Electric Field contour plot of an oscillating vertical current dipole by using Mur's Boundaries as ABCs (a) Contour Radiation Pattern for the first Order and second order approximation presented in [33] (b) 1st Order and 2nd Order Mur's Boundaries implementation

As the results presented in [33] were obtained from a 2D implementation of the FDTD method, and the implementation made in this thesis was extended to the 3D full wave solution, some slightly differences between both results are present. It can be seen that using the Mur's boundaries, the expected behavior of the electric field of a typical vertical dipole can be well reproduced by the proposed expressions for the truncation of the computational domain. It can be also seen that the second order representation of the boundary conditions improves enormously the radiation contour plot when they are compared to the first order approach.

3.6.2.2 Liao´s Boundaries

The Liao´s boundaries are one of the most simple and effective absorbing boundary conditions presented in the literature. They were proposed in 1984 by Liao et al [35]. The idea behind the Liao's proposal is to obtain the electric field components at the boundary by means of an extrapolation of the internal electric field values. These boundaries are based on the wave propagation characteristics as it was proposed by Mur [33]. However, the fields at the boundary are calculated based on the past values of the fields using a polynomial expression. Figure 14 presents an interpretation of the Liao´s extrapolation for a one-dimensional propagating wave.

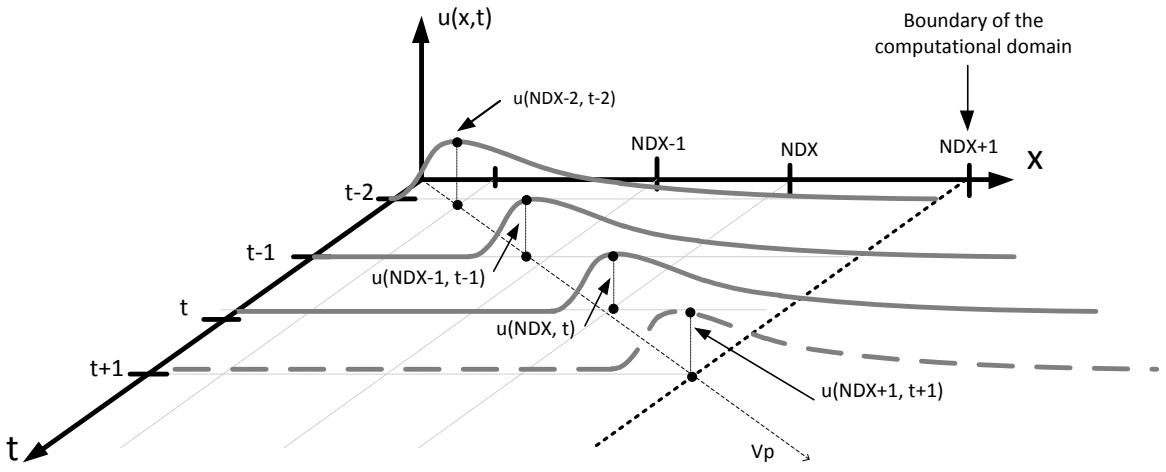

Figure 14 One-Dimensional propagating wave calculated at discrete time-spatial locations

Figure 14 shows a one-dimensional wave *u*(x,t) propagating at a fixed velocity Vp. The unknown value at the boundary u(NDX+1,t+1) is proposed to be obtained from past values of the same function, using an extrapolation equation representing the propagation characteristics of the traveling wave. Liao´s boundaries formulation establishes this kind of relation based on past values from the traveling wave as:

$$u(\mathrm{NDX}+1, t+1) = A_0 u(\mathrm{NDX}, t) + A_1 u(\mathrm{NDX}-1, t-1) + A_2 u(\mathrm{NDX}-2, t-2) + \cdots + A_n u(\mathrm{NDX}-\mathrm{n}, t-n) \quad (3.84)$$

The expression (3.84) adopts the form of an interpolating Newton's polynomial and the unknown constants can be calculated as shown in [30]. Depending on the number past-time terms, the Liao´s Boundaries are higher in order and obviously more past field values must be allocated during the FDTD loop calculations.

It can be demonstrated that finding the coefficients of the interpolating Newton's polynomial, the expressions for the 2nd order and 3rd order Liao's boundaries can be written respectively as [30]:

$$u(\mathrm{NDX}+1, t+1) = 2u(\mathrm{NDX}, t) - 1u(\mathrm{NDX}-1, t-1) \quad (3.85)$$

$$u(\mathrm{NDX}+1, t+1) = 3u(\mathrm{NDX}, t) - 3u(\mathrm{NDX}-1, t-1) + u(\mathrm{NDX}-2, t-2) \quad (3.86)$$

As an example of the performance of the Liao's boundaries, a comparison between the Mur´s boundaries presented before and the Liao´s boundaries was implemented. The simulation set-up is the same as that presented in section 3.6.2.1. Figure 15(a) presents the radiation pattern when 2nd order Mur´s boundaries are applied and Figure 15(b) presents the same simulation set-up when Liao's 2nd order boundaries are applied.

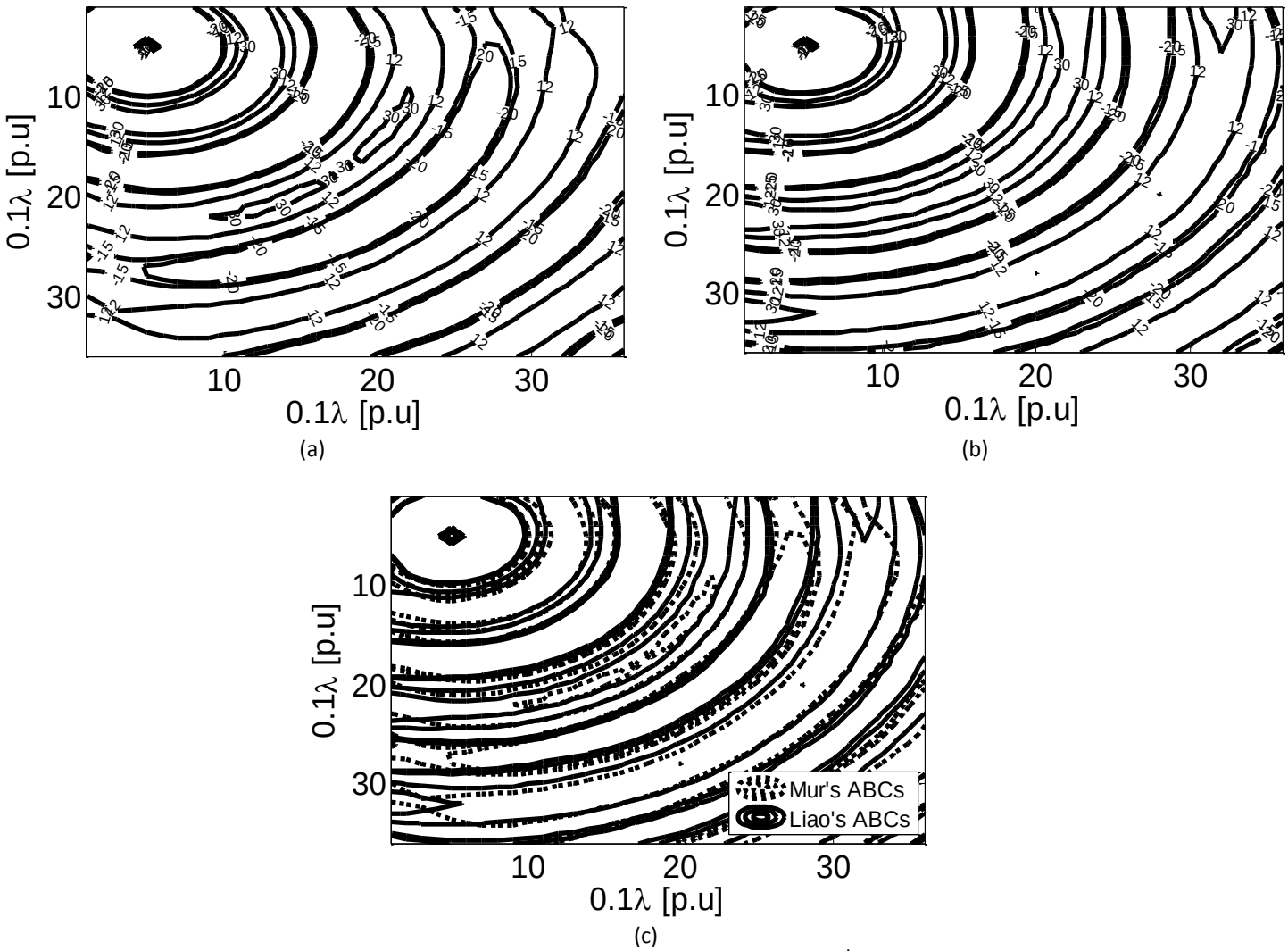

Figure 15 Liao´s Boundaries performance compared with (a) Mur´s Boundaries (2nd Order) Boundaries (b) Liao's Boundaries (2nd Order) (c) Contour plot comparison

As can be seen from Figure 15(c), Liao's boundaries present a better performance for the expected cylindrical pattern. Due to this, Liao's boundaries have become one of the most used absorbing boundaries not only by its good performance, but also by its straightforward implementation when compared with other sophisticated absorbing boundary conditions. Liao´s boundaries has been tested in several numeric experiments and it has been shown a good absorbing condition and low sensitivity to the incident wave propagating angle. These boundaries present between 10dB and 20dB less reflection than the 2nd order Mur's boundaries [30].

3.6.3 PML and CPML Boundaries

One of the most effective implementation for absorbing boundaries is that proposed by Berenger in 1994 [36]. This approach is based on the idea of truncating the computational domain by means of an artificial medium with the same electromagnetic propagation characteristics of the medium in which an electromagnetic wave is propagating through. This has the mathematical consequence of non-reflections from the truncating medium. The Perfectly Matched Layer - PML absorbing boundary condition can theoretically perfectly match any type of medium [36]. Depending on the implementation and the discretization of the equations, some numerical reflections can occur. However, it has been shown that the reflections due to the PML implementation are far lower than other absorbing boundaries approaches [30][36].

The implementation of the PML into the FDTD method has been very popular and its better performance as an absorbing boundary condition has been widely demonstrated [30][31][36][37]. The Convolutional Perfect Matched Layer (CPML) is an improvement of the PML boundary condition [31][39].

Figure 16 presents a comparison of the performance between the CPML boundaries and the implementations of boundary conditions that have been analyzed before in this thesis. The results presented for the CPML boundary conditions were obtained by using the formulation discussed in [31].

The simulation setup was composed of a vertical electric dipole represented by a voltage source with a 50Ω internal resistance. The total problem space was 50 x 50 x 50m^3 and the discretization was performed using cubic Yee´s cells with 1m^3 in volume. The source was placed at the center of the problem space volume and the observation point was located at the coordinate (X=10.5m, Y=10.5m, and Z=10.5m). The voltage source excitation was set to be a Gaussian's pulse described by the expression:

$$V(t) = e^{-\frac{(t-t_0)^2}{\tau^2}} \tag{3.87}$$

The parameters were set to $t_0 = 150\text{ns}$ and $\tau = 33.35\text{ns}$ [31].Figure 16(a) presents the excitation waveform.

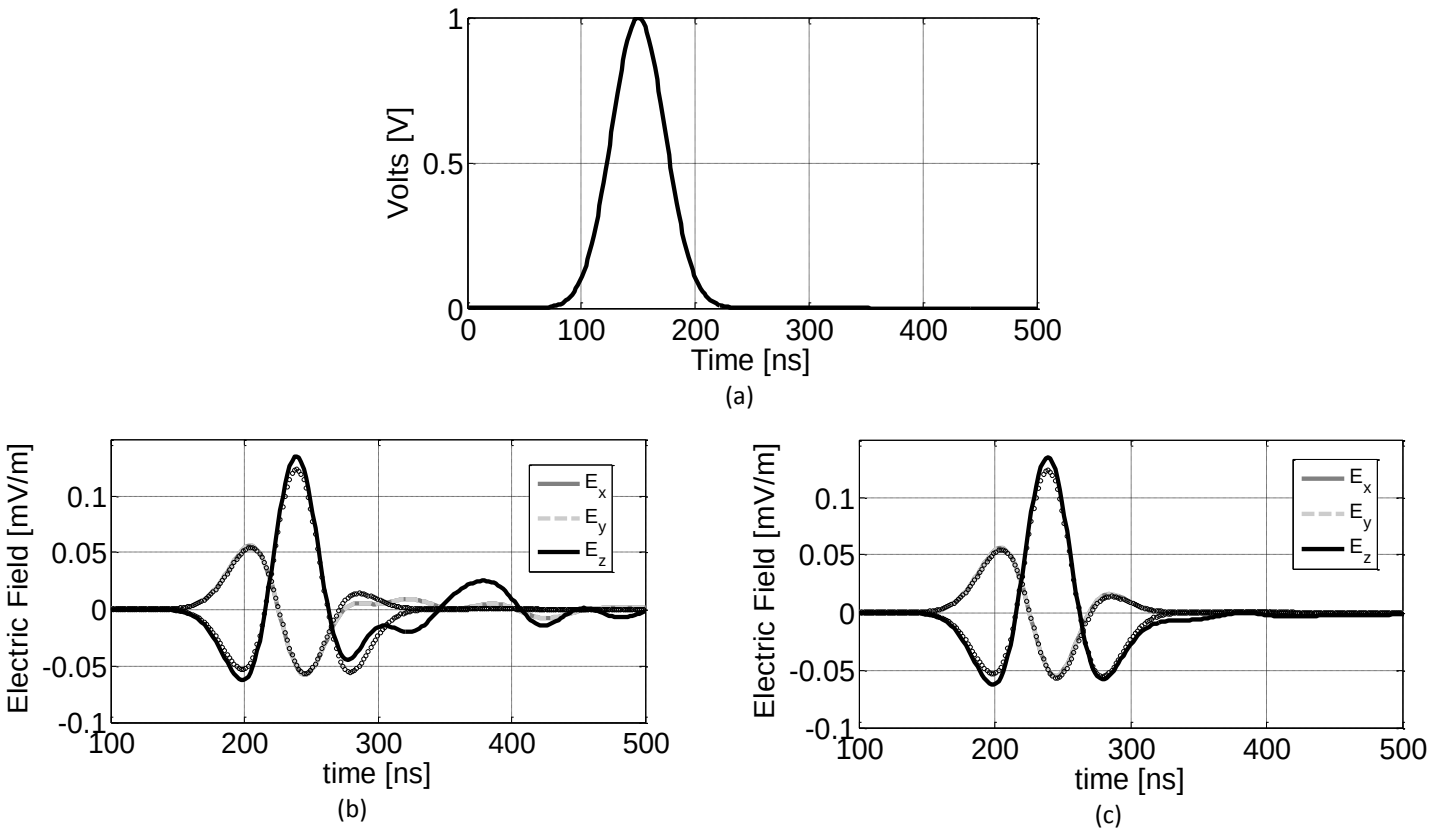

Figure 16 Comparison between ABCs boundaries implementations (a) Gaussian's Pulse Excitation (b) Mur's and CPML ABCs (Solid: Mur's 2nd Order 3D Boundaries, Circles: CPML) (c) Performance Comparison between Liao's and CPML ABCs (Solid: Liao's 2nd Order Boundaries, Circles: CPML)

As can be seen from Figure 16(b) the Mur´s boundary condition for the case under simulation presents some reflections distorting the electric field components before vanishing at latter time instants. This effect is more representative for the vertical component of the electric field. For the X and Y component of the electric field no representative reflections are observed mainly because the incident angle of the traveling wave is near to be normal at the boundary surface.

From the derivation of the Mur's boundaries shown in section 3.6.2.1, it can be observed that they are obtained assuming a plane wave incidence. Therefore, a high sensitivity of the wave-propagation angle is present expected and hence, affecting its effectiveness for grazing incidence.

In Figure 16(c) there is a comparison for the Liao's boundary conditions and the CPML ones. As it can be seen, the Liao's boundaries absorb almost perfectly the incident wave due to the X and Y component and its waveform is in very good agreement with those results calculated by the CPML implementation. As in the Mur's boundaries, Liao´s presents some reflections for the vertical component but it is also evident that for the Liao´s boundaries the Z component converges rapidly to zero.

3.7 Thin-Wire Modeling

Overhead lines are one of the most common configuration for electric energy distribution. Depending on the amount of power to be transmitted, the number of wires and its configuration can vary; the simplest configuration is the single wire above the ground.

The problem of including wires into FDTD simulations raises from the inclusion of the small geometrical dimensions of the wire into larger cell sizes. A fine mesh could be used for representing thin wires geometry and its conductive characteristics. Nevertheless, simulations of full size scenarios using such sizes for the FDTD cells are even today computationally prohibitive.

In order to include a thin wire into the FDTD simulations, several models have been proposed assuming that their radius are smaller than the cell side length [40][41].

Figure 17 shows the main features of the inclusion of a perfectly conducting wire into the FDTD method along the z-axis direction. The wire is represented by a cylindrical segment with ΔZ in length and radius *a*. As it is shown in Figure 17, the wire is placed along one of the edges of a Yee's cube. The vertical electric field component along the wire is forced to be zero; the equations related to the surrounding components of the electromagnetic field remain initially unaltered from those formulated in section 3.2.

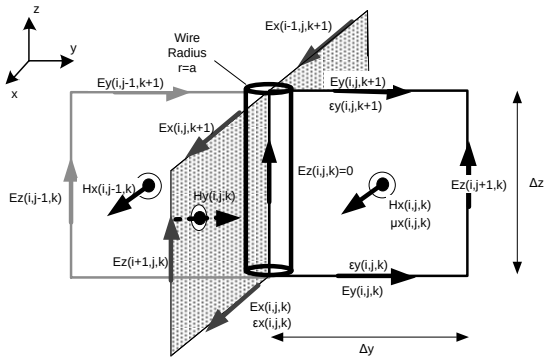

Figure 17 Thin-wire segment inclusion into the Yee´s cell

In order to take into account the presence of the thin wire, the constitutive parameters related to the surrounding components must be modified due to the thin wire presence. Next sections present two of the most popular thin-wire approaches.

3.7.1 Umashanark´s Model (UM)

A very popular thin wire model was proposed by Umashankar et al. [40]. This thin-wire model (called UM in the following) is based on a modification of the surrounding magnetic field components due to the presence of the wire. The main idea behind the Umashankar´s proposal is

to find the surrounding magnetic field by means of the Faraday´s law equation assuming an electrostatic and magnetostatic behavior of the fields near the wire[30][31][40]. In Figure 18 there is a representation of a vertical segment of a straight wire.

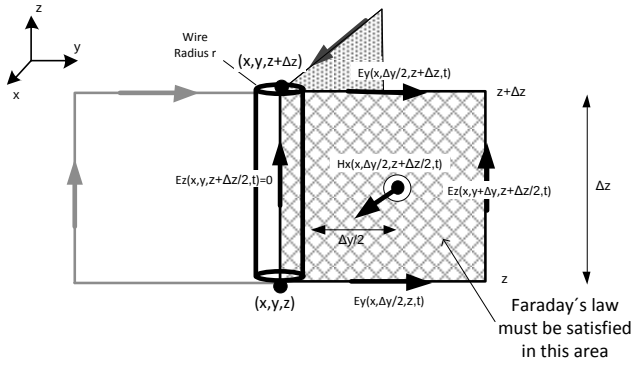

Figure 18 Segment of a z-directed wire

Applying the Faraday´s law on the shadowed area, the components of the fields can be related each other as:

$$\iint_{\Delta y \Delta z} \nabla \times \vec{E}\,\overrightarrow{ds} = -\mu \iint_{\Delta y \Delta z} \frac{\partial \vec{H}}{\partial t}\overrightarrow{ds} \tag{3.88}$$

Using the Stokes´ theorem in (3.88) a relation between the magnetic field on the area of interest and the surrounding electric fields can be obtained:

$$\oint_{l} \vec{E}\overrightarrow{dl} = -\mu \frac{\partial}{\partial t} \iint_{\Delta y \Delta z} \vec{H}\overrightarrow{ds} \tag{3.89}$$

Assuming static electric and magnetic fields distributions in the vicinity the wire, their components can be expressed as inverse-distance dependent from the wire axis, as:

$$\overrightarrow{E_y}(y,z,t) = \frac{E_{y0}\big|_z(t)}{y} \tag{3.90}$$

$$\overrightarrow{E_y}(y,z+\Delta z,t) = \frac{E_{y0}\big|_{z+\Delta z}(t)}{y} \tag{3.91}$$

$$\overrightarrow{H_x}(y,z,t) = \frac{H_{x0}(t)}{y} \tag{3.92}$$

where $E_{y0}\big|_z(t)$, $E_{y0}\big|_{z+\Delta z}(t)$ and $H_{x0}(t)$ are a unknown time-dependent functions evaluated at the locations depicted in Figure 18. Including them into (3.89) it can be obtained:

$$\int_{r}^{\Delta y}\left(\frac{E_{y0}\big|_{z+\Delta z}}{y}\right)dy - E_z(\Delta y)\Delta z - \int_{r}^{\Delta y}\left(\frac{E_{y0}\big|_{z}}{y}\right)dy = -\mu\frac{\partial}{\partial t}\left(\iint_{\Delta y\Delta z}\frac{H_{x0}}{y}dydz\right) \tag{3.93}$$

Integrating (3.93) and rearranging some terms,

$$\left[E_{y0}\big|_{z+\Delta z} - E_{y0}\big|_{z}\right]\ln\left(\frac{\Delta y}{r}\right) - E_z(\Delta y)\Delta z = -\mu\Delta z\ln\left(\frac{\Delta y}{r}\right)\frac{\partial H_{x0}}{\partial t} \tag{3.94}$$

Evaluating the fields at the locations presented in Figure 18, it can be found that:

$$E_{y0}\big|_{z+\Delta z}(t) = \left(\frac{\Delta y}{2}\right)E_y\left(\frac{\Delta y}{2}, z+\Delta z, t\right) \tag{3.95}$$

$$E_{y0}\big|_{z}(t) = \left(\frac{\Delta y}{2}\right)E_y\left(\frac{\Delta y}{2}, z, t\right) \tag{3.96}$$

$$H_{x0}(t) = \left(\frac{\Delta y}{2}\right)H_x\left(\frac{\Delta y}{2}, t\right) \tag{3.97}$$

Replacing (3.95), (3.96) and (3.97) in (3.94) yields finally to:

$$-\mu\Delta z\ln\left(\frac{\Delta y}{r}\right)\left(\frac{\Delta y}{2}\right)\frac{\partial H_x\left(\frac{\Delta y}{2}\right)}{\partial t} = \left[\left(\frac{\Delta y}{2}\right)E_y\left(\frac{\Delta y}{2}, z+\Delta z\right) - \left(\frac{\Delta y}{2}\right)E_y\left(\frac{\Delta y}{2}, z\right)\right]\ln\left(\frac{\Delta y}{r}\right) - E_z(\Delta y)\Delta z \tag{3.98}$$

Rearranging terms in the (3.98) it is possible to obtain:

$$\frac{\partial H_x\left(\frac{\Delta y}{2}\right)}{\partial t} = \frac{2}{\Delta y\mu\ln\left(\frac{\Delta y}{r}\right)}E_z(\Delta y) - \frac{1}{\mu\Delta z}\left[E_y\left(\frac{\Delta y}{2}, z+\Delta z\right) - E_y\left(\frac{\Delta y}{2}, z\right)\right] \tag{3.99}$$

Figure 19 presents the inclusion of a vertical thin-wire segment between the nodes *(i,j,k)* and *(i,j,k+1)* using the same indexes notation as in section 3.2. It is worth noting that the location of the components coincides with those obtained from the Umashankar's method but in this case for a general location point *(i,j,k)* in the discrete computational domain in order to use the FDTD scheme for the time-space discretization [31][40].

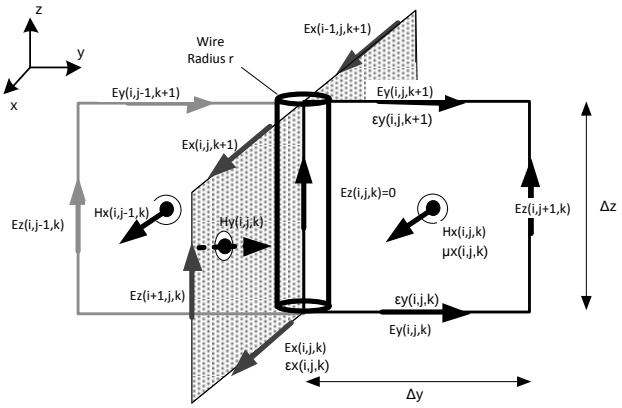

Figure 19 Thin-wire inclusion in the Yee´s cube

In order to discretize (3.99) and include it into the FDTD scheme, the time-updating equations for the magnetic fields presented in section 3.1 and section 3.4 must be modified for all magnetic components surrounding the wire. The discrete time-updating equation for the magnetic fields components around the wire shown in Figure 19, can be found applying the central difference approach to (3.99) leading to:

$$H_x^{n+1/2}(i,j,k) = H_x^{n-1/2}(i,j,k) + \frac{2\Delta t}{\Delta y \mu(i,j,k) \ln\left(\frac{\Delta y}{r}\right)} E_z^n(i,j+1,k) - \frac{\Delta t}{\mu(i,j,k)\Delta z}\left[E_y^n(i,j,k+1) - E_y^n(i,j,k)\right] \quad (3.100)$$

The UM model has been useful for the calculation of the radiated fields from an antenna; however its accuracy decreases for surge impedance calculations [40][41].

3.7.2 Noda-Yokoyamas's Model (NY)

As it was presented in the previous section, the thin-wire is included into the FDTD scheme modifying the time-updating equations for the magnetic field components around the wire. Noda and Yokoyama proposed a thin-wire model (NY) based on the concept of the *intrinsic radius* [41]. In this model, the electric field component along the wire is also forced to be zero in order to satisfy the perfectly conductive condition inside the wire. Besides, this model modifies not only the surrounding magnetic field components but also the electric field ones.

The NY thin-wire representation assumes an artificial wire with radius r_o surrounded by a modified media characterized by its electric permittivity and magnetic permeability, in order to reproduce the electric and magnetic field distributions around the actual wire. This artificial radius is called the *intrinsic radius.* The correction factor *m* applied to the electric permittivity and magnetic permeability around the artificial wire, can be found by equating the electrostatic distribution due to the actual wire to the distribution produced by the artificial wire. According to this, the correction factor can be calculated from [41]:

$$m = \frac{1.471}{\ln\left(\frac{\Delta s}{r}\right)} \tag{3.101}$$

where Δs is the side length as it is shown in Figure 20. Once the correction factor is calculated, the modified permittivity ε' and the modified permeability μ'around the wire can be obtained from (3.102) and (3.103) respectively.

$$\varepsilon' = \varepsilon m \tag{3.102}$$
$$\mu' = \mu / m \tag{3.103}$$

Figure 20 presents the permittivity and permeability components around the wire that must be modified by the factor *m* calculated in (3.101). These components have been highlighted in the figure.

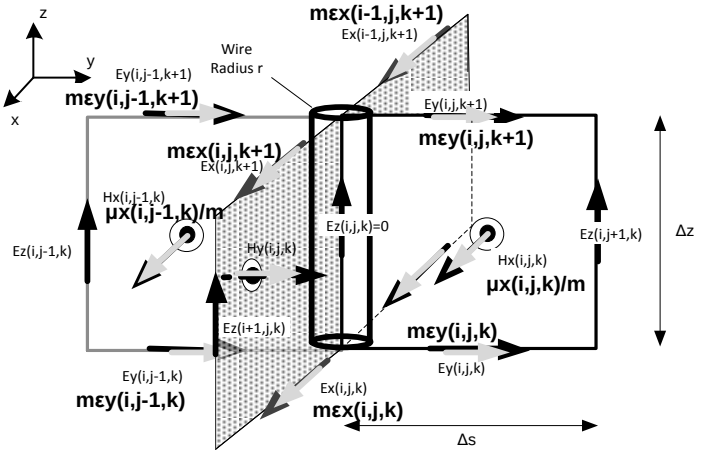

Figure 20 Permittivity and Permeability components modifications for the NY thin-wire model

An experimental setup is proposed in [41] where a horizontal wire was placed above a conductive plate with 50cm in height and 4m in length. The wire was excited by a voltage pulse in one of its ends and current and voltages where measured. Figure 21 depicts the experimental set-up.

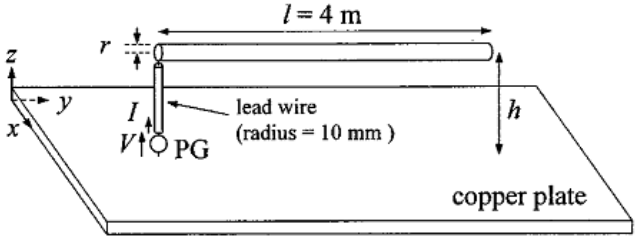

Figure 21 Experimental Set-up geometry for a Horizontal conductor above a Cooper Plate (from [41])

In order to verify the validity of the thin-wire implementation into the FDTD scheme developed in this thesis, the source waveform presented in [41] was assumed to have a ramp waveform with

10ns of time-rise and 60V of peak value. The used waveform for the simulation is presented in Figure 22(a)

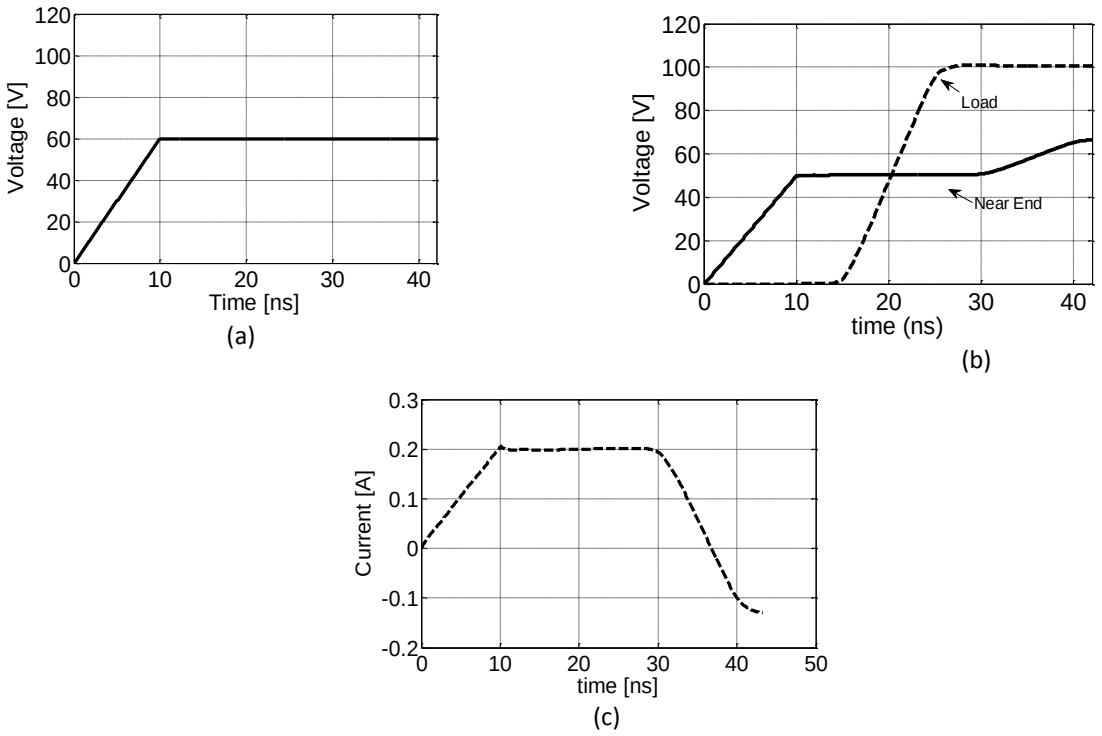

Figure 22 Thin-wire Representation (a) Voltage Source Waveform (b) Voltages at the near and far end of the line (c) Current Waveform at the source

Figure 22(b) shows the voltages at the end of the source vertical wire and at the end of the line. Figure 22(c) shows the current at the source. The results presented before have similar waveforms and magnitudes as those presented in [41]. Some differences are present in the predicted current and voltages because in this simulation the voltage waveform was approximated to a ramp waveform and in [41] it was included as piece-wise linear approximation of the actual measured voltage.

In order to validate the capability of the NY thin-wire model to represent wires, the voltages along the line were calculated using a TEM approach taking into account the frequency dependence of the parameters through the J-Marti model of the ATP/EMTP [43][44][45][46]. In Figure 23 the comparison between the two approaches is shown. It is worth noting that the source vertical conductor is strictly a non-uniform transmission line, then its representation by using the TEM approach and the J-Marti model cannot be in rigor performed. For the simulation the vertical wire a uniform horizontal transmission line with 10mm in radius and 50cm in height was used.

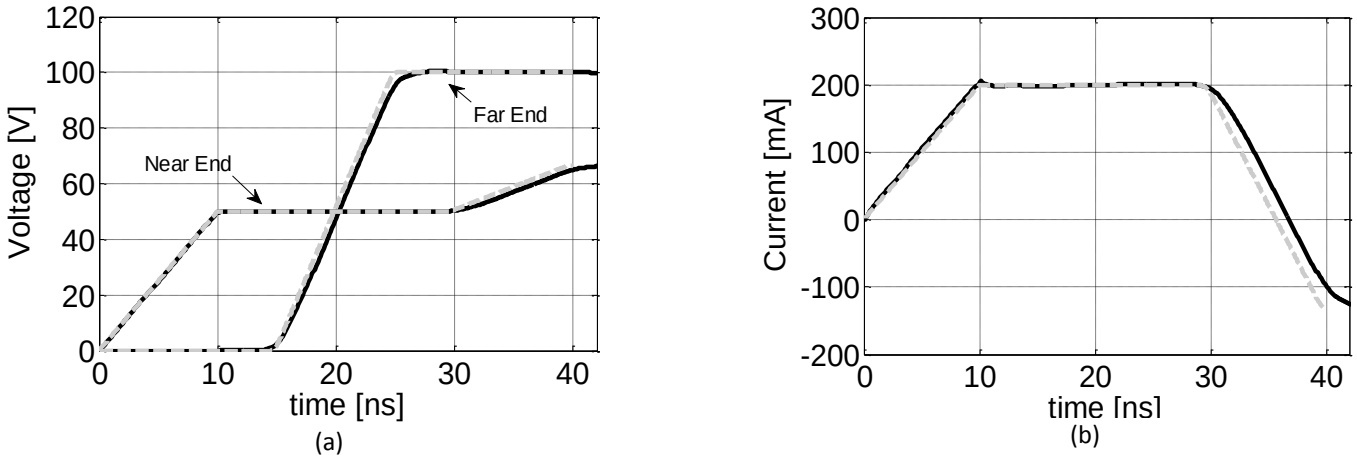

Figure 23 Comparison between the TEM approach and the FDTD calculations (dashed: TEM Approach, Solid: FDTD) (a) Voltages along the Line (b) Current at the source

As it can be seen from Figure 23(a), the voltage waveforms predicted by the thin-wire representation included into the FDTD method agree with those predicted by the TEM approach. Some differences are present in the waveforms mainly due to the representation of the vertical wire in the TEM approach, as it produces a different reflection coefficient for the back-propagating wave.

The results presented in Figure 23 show the validity of the thin-wire model for predicting surge-wave propagation along overhead lines.

3.7.3 Limit of Stability of the NY-Thin Wire

Using the thin wire formulation based on the modification of the surrounding permeability and permittivity of the wire as it was discussed in the previous section, the incident and scattered fields near the wire will be affected by the artificial media modification. Due to this, the Poynting´s vector around the wire will present different magnitudes when it is calculated for the magnetic components parallel to the wire. This difference occurs because the magnetic field modification leads to differences in the propagation wave constants around the wire [42]. It can be demonstrated that the NY thin-wire formulation leads into numerical instability when the side-cell size is larger than: r/0.15; being r the radius of the wire [42].

In order to validate the instability condition, the same set-up presented in Figure 21 will be analyzed. In this case, if the minimum radius is defined to be 10mm (which is the radius of the source vertical conductor) the maximum size of the cell must be about 6.67cm being at the limit of stability. In order to reach the numerical instability, the same simulation was performed using ΔS=8cm. The courant's factor is fixed to be 0.9. Figure 24 presents the voltage calculation along the line in order to validate the achievement of the instability condition.

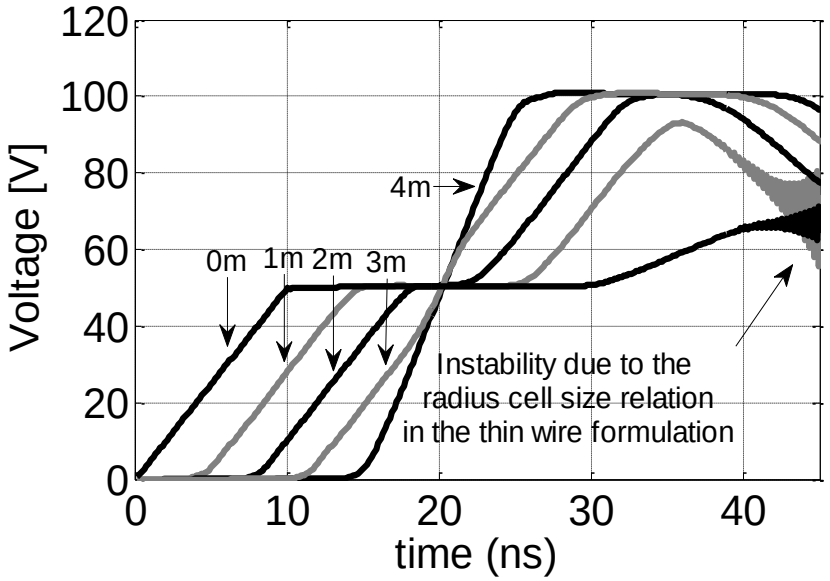

Figure 24 Instability condition for radius lower than 0.15 times the cell-side size

As can be seen from Figure 24 the voltages along the line are well reproduced for the first time instants. However, due to the error propagation caused by the Poynting's vector difference discussed before, the FDTD simulation becomes unstable at about 38ns.

3.7.4 Improved Noda-Yokoyama Model (INY)

The thin wire improvement proposed in [42], which will be referred as **INY**, proposes modifying not only the magnetic relative permeability around the wire but also the components in the vicinity in order to obtain the same Poyinting´s vector. The improved thin wire formulation was included in the simulation using ΔS=8cm and maintaining the geometry as was proposed in Figure 21. The instability problem presented in Figure 24 was solved as it is shown in Figure 25.

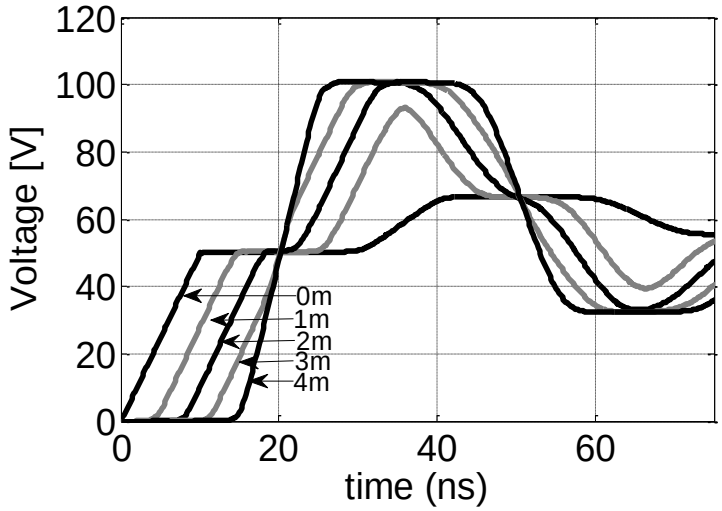

Figure 25 Voltages along the Line by using the Improved Thin-Wire Formulation

A comparison for the same simulation set-up using the **NY** thin-wire model and the **INY** thin-wire model was made. The results at the near and far end of the line are shown in order to validate that the modification proposed in [42] does not affected the performance of the NY thin-wire model. Figure 26 presents the comparison between the **INY** improved thin-wire formulation and the stable **NY** thin-wire model.

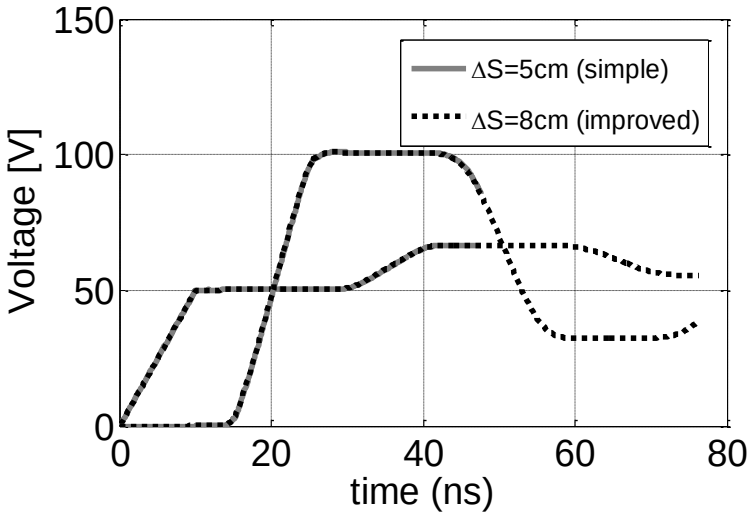

Figure 26 Voltages at the near and far end of the Line (a) Thin Wire placed on the X-axis direction

As can be seen from Figure 26 both models reproduce the same waveform for the voltages at the near and far end of the line. The **INY** model was implemented in all directions into the FDTD scheme developed in this thesis.

3.8 Non-Regular mesh into the FDTD method

When the case under study requires simulating detailed structures or small objects using cubic cells, regular meshing can be computationally restrictive because a large number cells must be included into the domain under study in order to perform the simulation. As it was explained in section 3.2, Maxwell´s equations relate the electromagnetic field components initially located on the sides of a cubic cell. However, based on the same central-difference approach and the recursive scheme for the time-domain electromagnetic field solution proposed by Yee, a non-regular mesh can be also be used in order to perform more detailed representations of complex geometries located in some regions inside de simulation space, and a coarser discretization for the rest of it [30].

Non-regular meshing presents important advantages over regular meshing. First, the formulation of the non-regular meshing does not modify the maximum quantization error in the central difference approach used in the FDTD method [30] and second, the matrix sizes used for saving the electromagnetic field components values can be reduced significantly. It reduces the memory allocated for the simulation and the total time spent to perform the simulation.

In this thesis a non-regular implementation of the FDTD method was implemented because the calculation of lightning induced voltages involves different detailed geometries that will not allow a simulation by means of cubic cells. It has been also proposed an algorithm for automatic mesh generation that will be explained in the following section.

3.8.1 The FDTD Method in a Non-regular Mesh

The FDTD method can be also formulated for a non-regular mesh as the Yee´s cell can be generalized to a prismatic volume. In this case, the components of the electric and magnetic fields will be located in the same fashion as the original ones. However, the length of the cell edges will be variable and the electric and magnetic field components location will be a function of it [30].

For the electric field component locations, the center of the edges and the length between them must be determined in order to modify the original time-updating equations for the magnetic field components. The edge lengths between the vertices in the non-regular mesh can be expressed by:

$$\Delta x_i = x_{i+1} - x_i \quad (3.104)$$
$$\Delta y_i = y_{i+1} - y_i \quad (3.105)$$
$$\Delta z_i = z_{i+1} - z_i \quad (3.106)$$

The edge centers can be defined by:

$$x_{i+1/2} = x_i + \Delta x_i/2 \quad (3.107)$$
$$y_{i+1/2} = y_i + \Delta y_i/2 \quad (3.108)$$
$$z_{i+1/2} = z_i + \Delta z_i/2 \quad (3.109)$$

For the magnetic field location and its time-updating equation based on the electric field component location, the lengths between the edge centers must be also determined. They will be denoted by the letter *h* as:

$$h_{ix} = \left(\frac{\Delta x_i + \Delta x_{i-1}}{2}\right) \tag{3.110}$$

$$h_{iy} = \left(\frac{\Delta y_i + \Delta y_{i-1}}{2}\right) \tag{3.111}$$

$$h_{iz} = \left(\frac{\Delta z_i + \Delta z_{i-1}}{2}\right) \tag{3.112}$$

Where $\Delta x_i, \Delta y_i$ and Δz_i are the lengths of the cell sides at the (i, j, k) location. Figure 27 shows the location of the electric and magnetic field components, and the cell lengths definition taking into account all of the expression presented before and using the same indexes notation as in section 3.2.

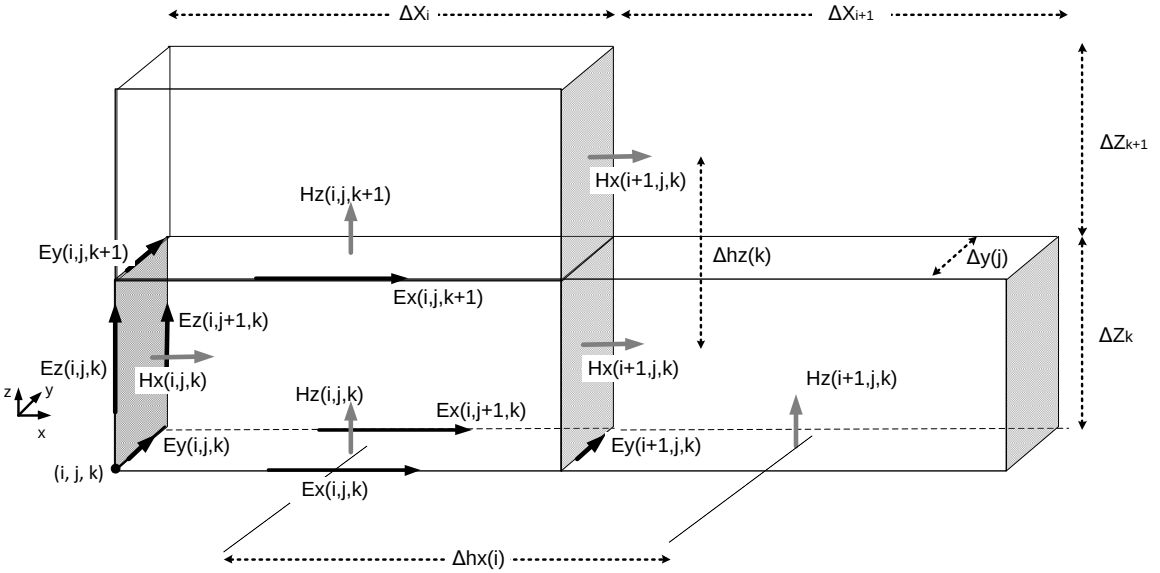

Figure 27 Location of the electric and magnetic field component in the non-regular cell

As it can be seen from Figure 27, the electric and magnetic field components are calculated at convenient locations in order to apply the finite difference formulation for the Maxwell's equations. This figure shows three Yee's cells adjacent to each other where different side lengths are considered for the cell located at the *(i,j,k)* node. It must be also note that due to the different cell-side lengths for each direction Δx_i, Δx_{i+1} and Δz_i, Δz_{i+1}, the distances Δh_x and Δh_z between the components will also change for each direction.

Finally, the electric field and magnetic field components can be found by similar time-updating equations presented in previous sections but taking into account the non-regular location of the edge centers, the variable cell-length and the distances between each edge center.

As an example, the central difference formulation for a non-regular cell applied to the x-component of the magnetic field is:

$$\frac{{H_x}^{n+1/2} - {H_x}^{n-1/2}}{\Delta t} = \frac{1}{\mu_x}\left(\frac{{E^n}_y(i,j,k+1) - {E^n}_y(i,j,k)}{2\Delta z(k)} - \frac{{E^n}_z(i,j+1,k) - {E^n}_z(i,j,k)}{2\Delta y(j)}\right) \quad (3.113)$$

3.8.2 Automatic-Mesh Algorithm

Several techniques can be proposed in order to generate the irregular mesh grid for the computational domain. In this section the performance for one of the algorithms that were taken into account is shown and a general formulation for defining the mesh grid is also presented. The procedure will be shown for the x-axis only. However, it can be used by the same fashion for the other the coordinate axes.

3.8.2.1 General Formulation

The aim of the meshing grid algorithm is to find the spatial coordinates when a spacing function is defined. There are two restrictions that must be imposed to the spacing function, the first one is that the derivative of the spacing function cannot be higher than 2; it means that the maximum change between two consecutive spacing sizes must twice as maximum [30]. The second restriction is that the coordinates of the mesh grid must be the cumulative sum of each of the spaces defined in the spacing function. In order to write these two restrictions in a mathematical form, consider $\Delta X(n)$ be the spacing function to be proposed, N the total of discrete points for the interval with $n = 0,1, \ldots . N$ and let be ΔX_{min} and ΔX_{max} the minimum and maximum spacing size respectively.

In order to include the minimum spacing restriction, the restriction $\Delta X(0) = \Delta X_{min}$ must be imposed. The minimum spacing parameter can be selected based on the dimensions of the geometry to be represented. For the maximum spacing selection in the coarser domain, the short-electric distance criteria must be satisfied. In this case, the maximum discretization step ΔX_{max} which can be defined as an input, must be less than $\lambda_{min}/10$ or $\lambda_{min}/15$ for more accurate solutions, where λ_{min} is the minimal wave-length corresponding to the upper frequency band component of the excitation source [30].

The number of the discrete points needed in the spacing-function are found given the restrictions to the spacing function imposed as:

$$\frac{d\Delta X(n)}{dn} \leq 2\Delta X_{min} \quad (3.114)$$

Finally, the second restriction can be written as:

$$\int_0^N \Delta X(n)dn = X_{max} - X_{min} \tag{3.115}$$

where, N is the upper limit of the integration interval.

Figure 28 presents an example of a spacing-function and its coordinates mesh distribution.

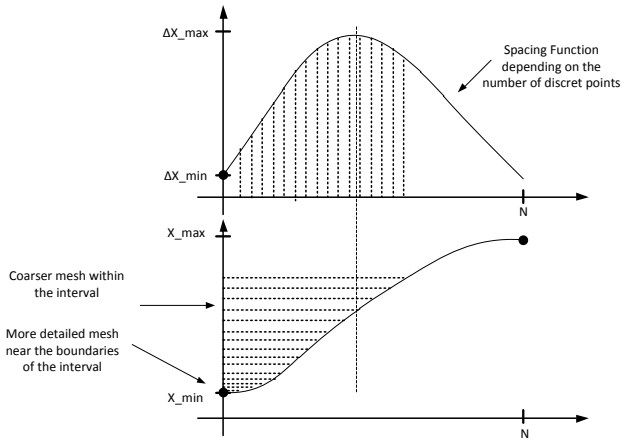

Figure 28 Spacing Function and Coordinate Points function

As it can be seen from Figure 28, there is a coarser spacing for the coordinate function in the middle on the interval and more detailed mesh can be found near its extreme values.

The mesh coordinates values can be found by evaluating the integral proposed for the second restriction. This can be done numerically by means of a first order approach. A recursive scheme for the coordinate points can be found as:

$$X(n_{i+1}) = X(n_i) + \Delta X(n_i) \tag{3.116}$$

Any spacing function can be used if the restrictions presented in (3.114) and (3.115) are satisfied; the recursive equation presented in (3.116) calculates the integral of (3.115) by a first order backward approach.

3.8.2.2 Parabolic Mesh

The parabolic meshing algorithm uses a linear equation for defining the spacing function. The maximum and minimum spacing values are required as inputs of the algorithm and also the limits of the interval to be meshed. This implementation leads to a parabolic mesh near to the limits of

the algorithm and a linear meshing within the interval; Figure 29 depicts the parabolic meshing algorithm.

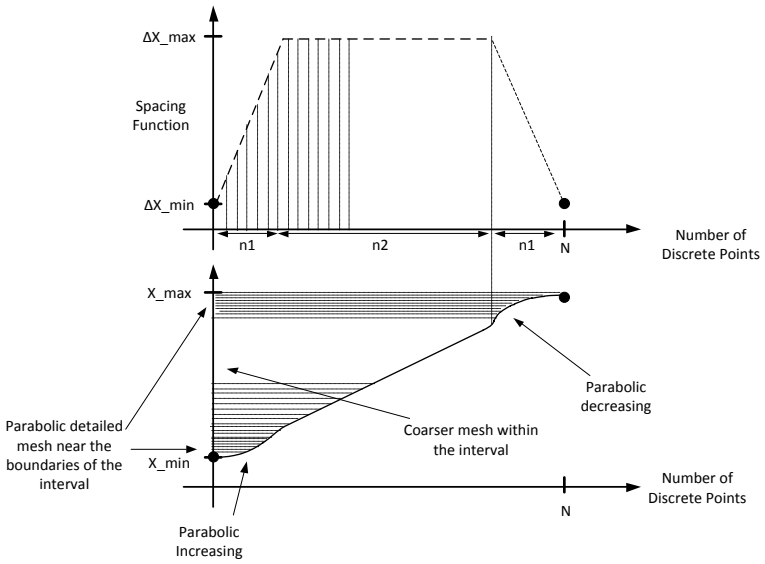

Figure 29 Parabolic Mesh based on a trapezoidal spacing function

The spacing function can be written as a piecewise function defined by:

$$\Delta X(n)\begin{cases} mn + \Delta X_{min} & n \leq n1 \\ \Delta X_{max} & n1 < n < n2 \\ -mn + m(n1+n2) + \Delta X_{min} & n \leq n1 + n2 \end{cases} \quad (3.117)$$

Where m is the slope of the straight line and $N = 2n1 + n2$.

In order to obtain n1, the restriction on the maximum spacing function derivative must be imposed. As the spacing function has the same linear variation on the increasing and decreasing sections, the derivative of the function can be evaluated in the first interval $n \leq n1$ as:

$$\frac{d\Delta X(n)}{dn} \leq 2 \quad (3.118)$$

$$m \leq 2\Delta X_{min} \quad (3.119)$$

$$n1 = (\Delta X_{max} - \Delta X_{min})/m \quad (3.120)$$

The slope m can be calculated from the desired spacing rate. In general $m = \alpha \Delta X_{min}$ where α can be set between $0 < \alpha \leq 2$ in order to consider the minimum and maximum slope respectively. The α factor can be understood as a decreasing or increasing factor for the spacing rate; α factors lower than 1 implies soft changes on the spacing mesh.

Using the definition of the second restriction for the spacing function we will have:

$$\int_0^N \Delta X(n)dn = X_{max} - X_{min} \tag{3.121}$$

Using this restriction it is obtained that:

$$2\frac{n_1(\Delta X_{max} - \Delta X_{min})}{2} + 2n_1\Delta X_{min} + n_2\Delta X_{max} = X_{max} - X_{min} \tag{3.122}$$

Where n_2 can be found by means of the expression:

$$n_2 = \frac{(X_{max} - X_{min}) - n_1(\Delta X_{min} + \Delta X_{max})}{\Delta X_{max}} \tag{3.123}$$

The spacing function has now been completely defined and the integration over the interval is performed numerically. Figure 30 show the automatic parabolic-mesh for an interval [100mm, 975mm] using a minimum spacing of 2.5mm and a maximum of 55mm. As can be seen from the Figure 30(b), 26 discrete points are needed for the entire interval using the irregular mesh instead of 350.000 discrete points required using the traditional regular meshing.

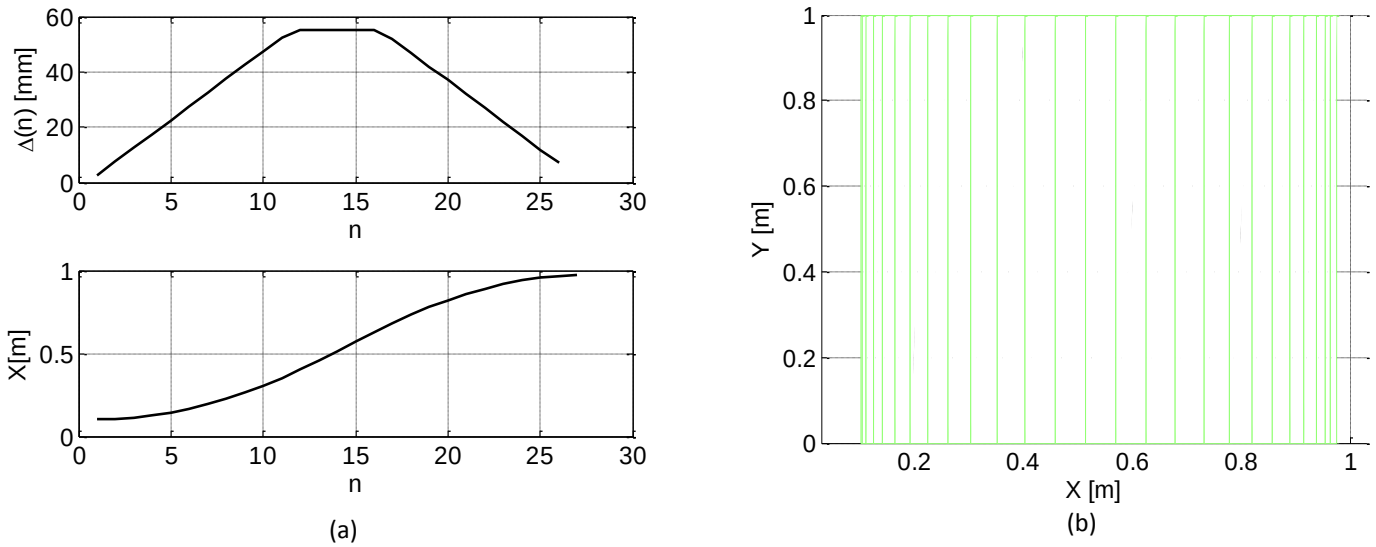

Figure 30 Parabolic Mesh Algorithm (a) Example of a Spacing Function (b) Coordinate mesh nodes

3.9 Experimental Validation Case: – The Cross-Talk Effect.

Crosstalk is an undesirable effect taking place when two or more transmission lines are close each other affecting their voltages and currents due to their strong capacitive and inductive coupling. This could lead to a corruption or distortion of their own transmitted signals [47][48].

Crosstalk is typically studied in transmission systems used in digital data at high frequencies, because the fast wave-fronts of the signals excites the frequency band where the capacitance and inductance coupling effect cannot be neglected. As Crosstalk could be higher enough for disabling the communication process between two points, this effect must be taken into account when the system is under operation. In cable manufacturing for example, crosstalk effect is commonly mitigated by braided cables and shielding techniques [47][48].

Despite the crosstalk effect is a near electromagnetic field problem and a rigorous solution must be performed using a full-wave solution of the electromagnetic problem [48], Multiconductor Transmission Line (MTL) theory assuming the transversal electromagnetic (TEM) propagation mode is an accurate way to deal with it [47][48].

The multiconductor transmission line model assumes a constant cross section along the length of the wires where the conductor and the return path are perfectly conductive. This is a good approximation when the MTL is larger than its height and when its non-uniformity is negligible. Another assumption is related to the uniform charge and current distribution along the line. As it is shown in Figure 31(a), there can be a proximity effect influence between conductors that create charge accumulation in some areas on the wire's surface. However, as can be demonstrated, when the distance S between wires is almost 7 times higher than the radius of the wire, the mutual influence is negligible.

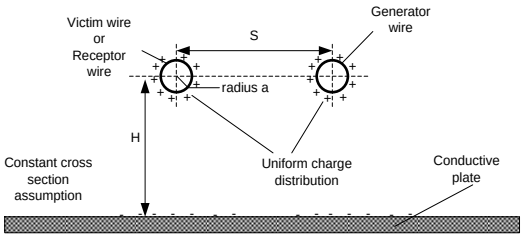

(a)

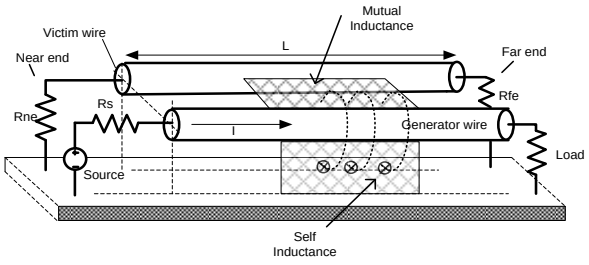

(b)

Figure 31(a) Schematic Representation of capacitive coupling for two wires above a conductive return plate (cross section). (b) Schematic Representation of inductive coupling for two wires above a conductive return plate (lateral section)

Current along the wire is assumed to be constant along an infinitesimal length allowing writing magnetic field expressions only from the geometric constants associated to the line conductors as it shown Figure 31(b). Finally, the consideration about a perfect conducting wire, can be easily overcome by the cuasi-TEM approximation where the electric field in the direction of propagation is neglected for low resistance values.

These assumptions allow having a transversal electromagnetic field along the line and voltages and current relation can be easily derived from this EM field formulation [47][48]. The well-known formulation for currents and voltages in the generator and receptor wire is presented as follows

$$\frac{\partial V_G(z,t)}{\partial z} = -l_G \frac{\partial I_G(z,t)}{\partial t} - l_m \frac{\partial I_R(z,t)}{\partial t} \quad (3.124)$$

$$\frac{\partial V_R(z,t)}{\partial z} = -l_m \frac{\partial I_G(z,t)}{\partial t} - l_R \frac{\partial I_R(z,t)}{\partial t} \quad (3.125)$$

$$\frac{\partial I_G(z,t)}{\partial z} = -(C_G + C_m) \frac{\partial V_G(z,t)}{\partial t} + C_m \frac{\partial V_R(z,t)}{\partial t} \quad (3.126)$$

$$\frac{\partial I_R(z,t)}{\partial z} = C_m \frac{\partial V_G(z,t)}{\partial t} - (C_R + C_m) \frac{\partial V_R(z,t)}{\partial t} \quad (3.127)$$

Where l_G, l_R and l_m are the self-inductance and mutual inductance and C_G, C_R and C_m are the self-capacitance and mutual capacitance for the generator and receptor wire respectively.

An experimental set up was implemented in order to compare the theoretically obtained results by computation and measured data. The set up was composed by two copper wires with a DC resistance per unit length of 84Ω/km located next to each other with a distance of 1.5cm between them. The radius of the wire was about 0.25mm. Each wire was horizontally at the same height of 5.5cm from a conductive plate. The resistivity of the plate was assumed to be 1.69×10^{-8}Ωm. The

victim wire was loaded at each end (Near End and Far End) with 50Ω resistances. The generator wire was excited by a ramp voltage source with 30ns of wave front and 20V in magnitude. The internal resistance of the source was 50Ω and the wire was also was also loaded with the same resistance value at the end. The experimental assembly is shown in Figure 32(a) and (b).

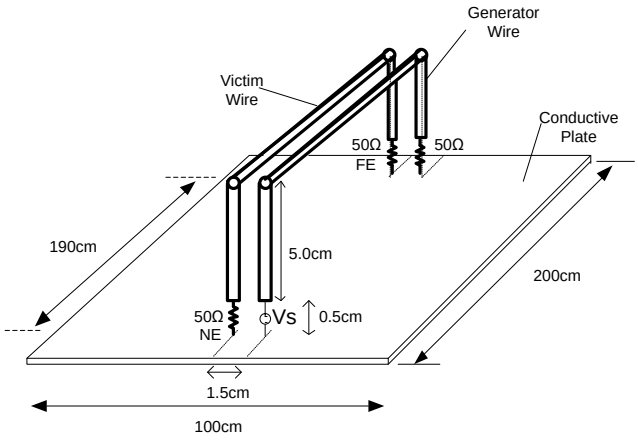

(a)

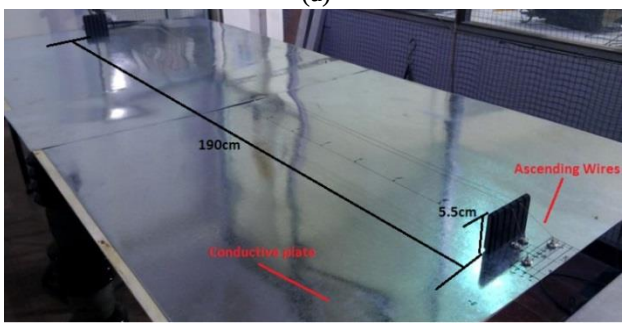

(b)

Figure 32 Typical Cross-talk Simulation scenario for two horizontal parallels wires (a) Schematic Representation of the experimental set-up (b) Experimental set-up.

The experimental set up shown in Figure 32(b) was used to compare the measured voltages at each extreme of the lines with simulated ones. The measurements were carried out with one oscilloscope at each extreme of the lines. The experimental waveforms are presented in Figure 33.

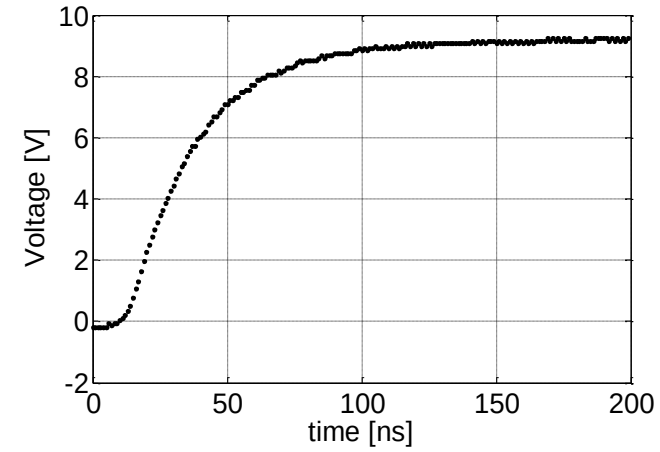

(a)

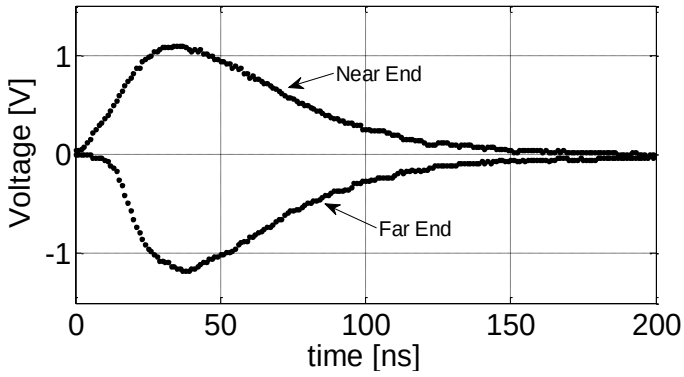

(b)

Figure 33 Measured Voltages on the Generator and the Victim Wire for the performed Cross-talk Experiment (a) Voltage on the load of the generator Wire (b) Victim Wire Voltages at the near and far end

Typically, the oscilloscope probes are compensated by a RC circuit that cannot be neglected in some frequency bands. Figure 34(a) shows the circuital model for the scope probe used in the experimental set-up and its frequency response is also shown in Figure 34(b). As can be seen from Figure 34(b), the probe response can be simplified at high frequencies as a resistive attenuation of almost 0.88 p.u. meaning that the scope probe will decrease the measured signal by 12% percent approximately; during the measurements, this effect was compensated.

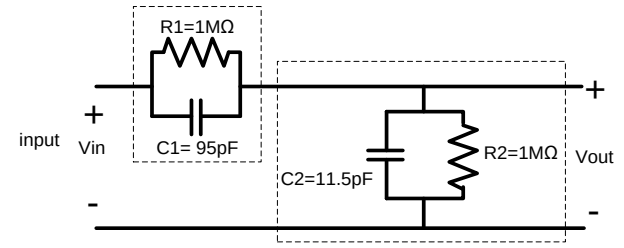

(a)

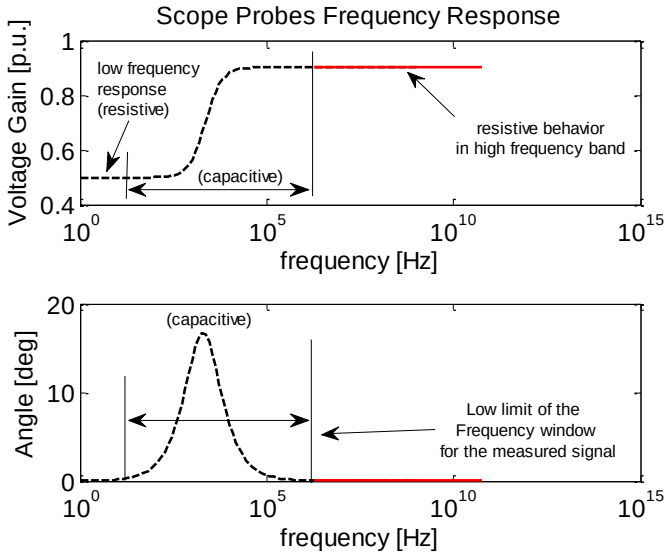

(b)

Figure 34 (a) Circuital model for the scope probe used in the measurements (b) Frequency response of the circuital model for the scope probe

The experimental set-up was modeled into the ATP/EMTP software, and into a FDTD method implementation. In order to validate the regular and non-regular performance for the FDTD simulations, two kinds of simulations were done: first, a regular mesh for the FDTD method was performed and second, a non-regular mesh obtained from the proposed automatic mesh algorithm presented in section 3.8.2.2 was implemented.

3.9.1 Simulation by FDTD using a Regular Mesh

The simulation set-up in FDTD was performed using a 1x2x0.2m^3 computational domain with a space cell discretization of 2.5mm. CPML absorbing boundary conditions were implemented in order to truncate the problem space. A total of 400x800x80 cells were used to represent the total problem space in the computational domain.

The ascending wire, also known as the riser wire, was simplified as a straight vertical wire as is shown in Figure 32(a). The results for the voltages on the generator wire and the victim wire (at the near and far end) were calculated by mean the TEM approach and the FDTD method. The results are shown in Figure 35 when a separation of 1.5cm between lines is considered.

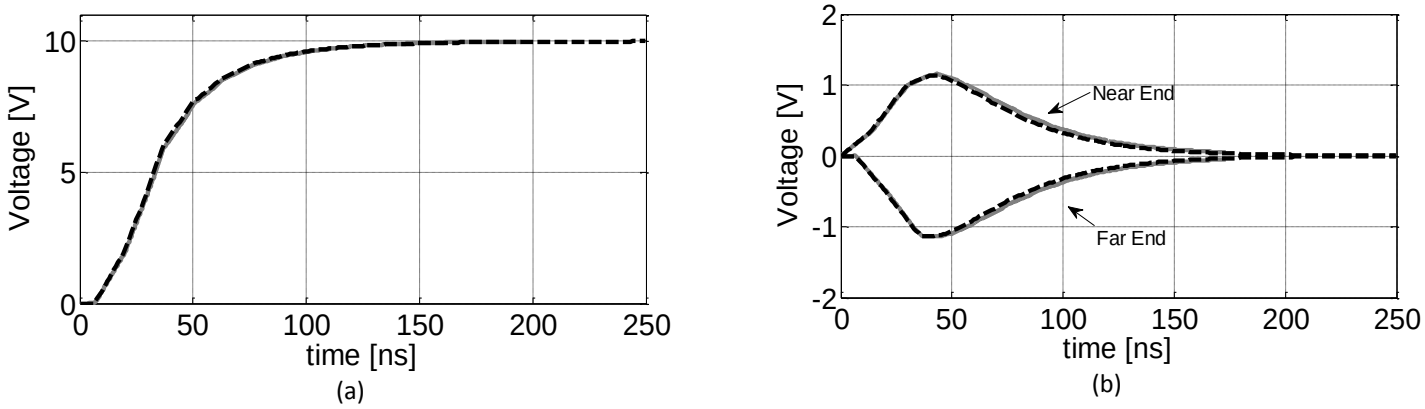

Figure 35 Voltages for a typical Cross-Talk set-up of two parallel conductor with 1.5cm of Separation (Dashed Line: ATP/EMTP, Solid Line: FDTD) (a) Voltages on Generator Wire (b) Voltages on Victim Wire at the near and far end.

Figure 36 shows the comparison between measured voltages and those predicted by the FDTD and TEM approach.

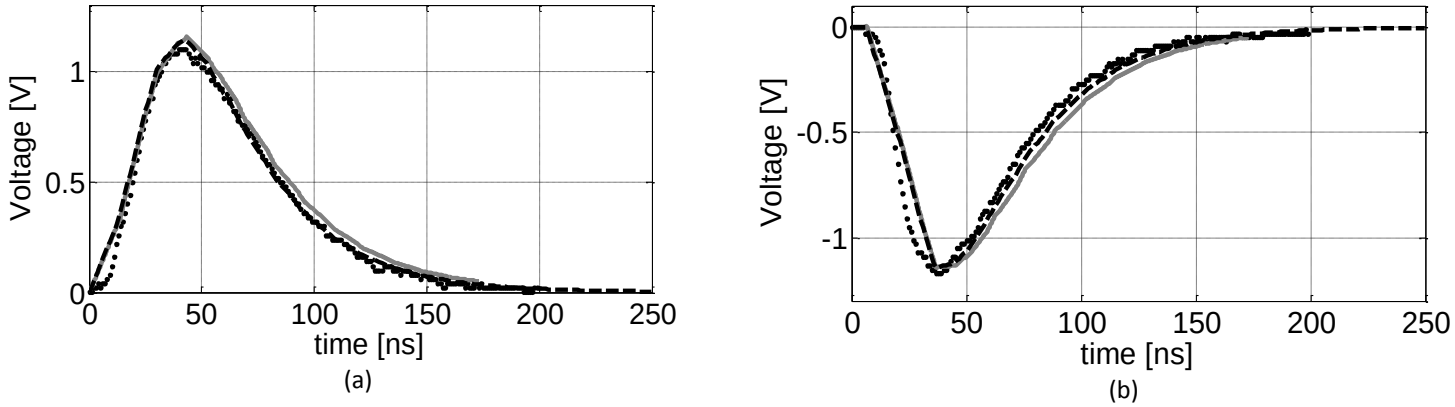

Figure 36 Victim Wire Induced Voltage (Dashed Line: ATP/EMTP, Solid Line: FDTD, Dotted: Measured) (a) Comparison between measured and TEM approach at source and load voltage (1.5cm of separation) (b) Comparison between measured and TEM approach at near and far end voltage (1.5cm of separation).

3.9.2 Simulation by FDTD using a Non-Regular Mesh

When a non-regular meshing is applied, longer physical dimensions can be represented using the same computational domain size. For this case a total cell domain 279x181x77 were needed for representing a total space of $4x1x1m^3$.

The FDTD non-regular simulation set up was truncated using 2nd Order Liao´s boundaries. Figure 37 shows the non-regular mesh for the simulation; the finer mesh was imposed near the line end locations.

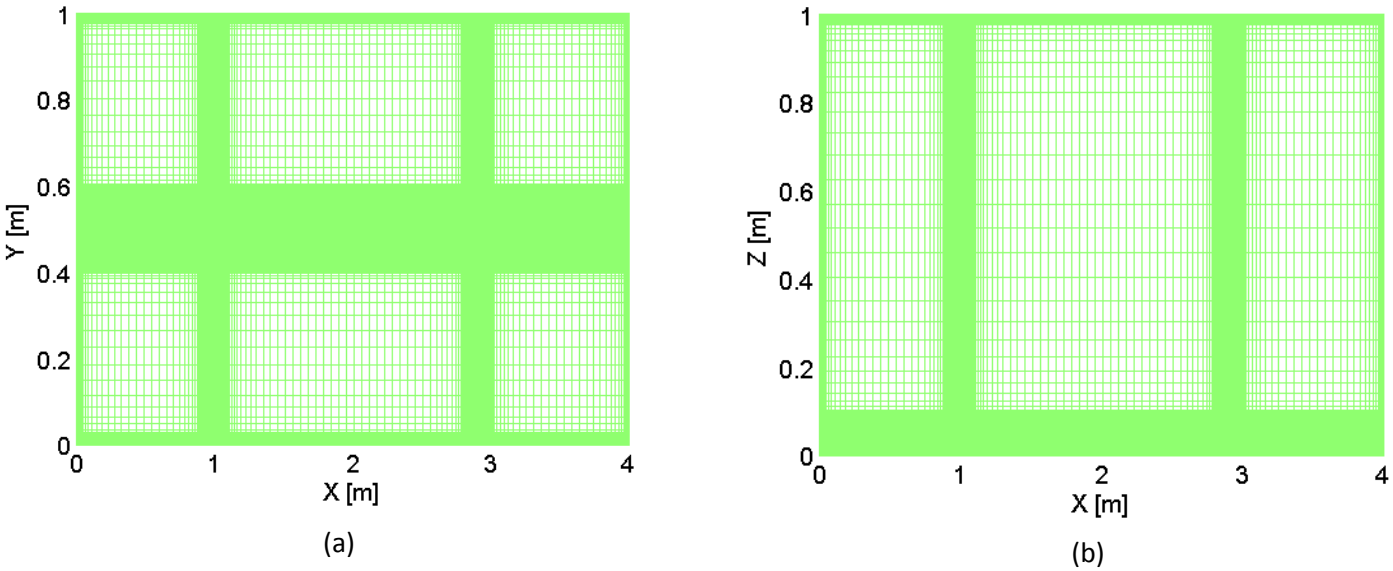

Figure 37 Irregular Meshing for the FDTD simulation (a) Top View (XY) (b) Lateral View (XZ)

The results for the FDTD non-regular mesh approach agree with those measured voltages as it is presented in Figure 38. These results validate the ability to represent by means of the FDTD method a uniform transmission line when a perfectly conducting ground is present.

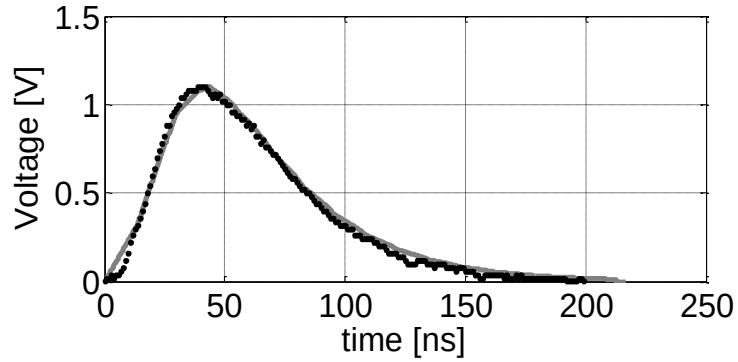

(a)

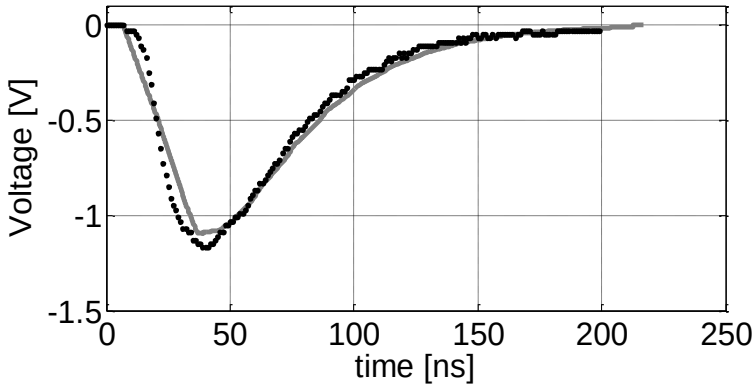

(b)

Figure 38 Voltages on the Victim Wire (dotted: Measured, solid: FDTD non-regular mesh) (a) Voltage at the Near End (b) Voltage at the Far End

4 Radiated Electromagnetic Field

Electromagnetic radiation occurs when a time-varying source is present in a region of the space, allowing the interaction of electric and magnetic fields in the medium and its propagation through the space [49]. Most of the analysis made on electromagnetic radiation are based on the Hertzian dipole concept in which a pair of wires of a finite length are excited at the middle by a voltage source as it is shown in Figure 39(a).

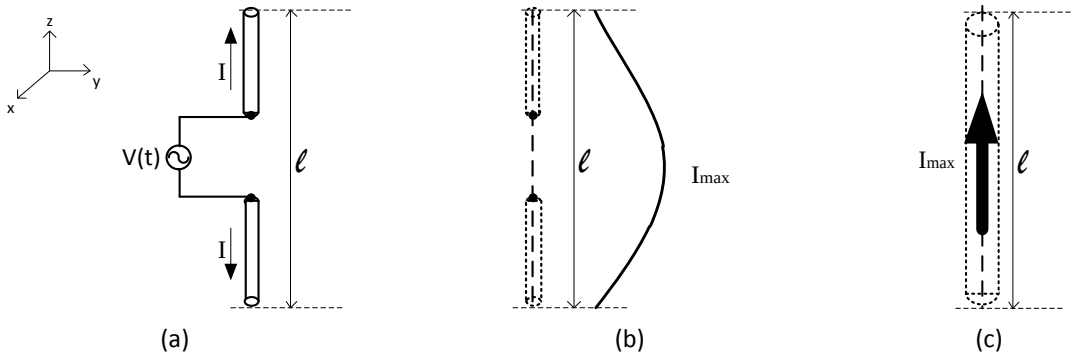

Figure 39 (a) Dipole Antenna (b) Current Distribution for a half-wave dipole (c) Current-Element Dipole

In order to calculate the radiation of the dipole, the distribution current along it must be known. This current distribution can be found by means of the scattered field formulation and the solution of the resulting integral equation. This integral equation can be solved by several numerical techniques being the Method of Moments (MoM) one of the most popular approaches for solving the current distribution along conducting wires in the frequency domain [49]. When the length of the wires is finite, the current distribution of the Hertizian dipole is maxima at the middle and decreases to the ends as is shown in Figure 39(b). The simplest representation of a radiating dipole is that known as the infinitesimal dipole or current dipole [16][49], where its current distribution along the segment is assumed to be constant even if it is finite in length as is shown in Figure 39(c).

This assumption simplifies enormously the calculation of radiated fields due to vertical current dipoles and it will be fundamental for the calculation of lightning electromagnetic fields as will be shown in chapter 5.

4.1 Radiating Vertical-Current Dipole over a homogeneous ground.

The geometry when a Cartesian coordinate system is assumed is shown in Figure 40.

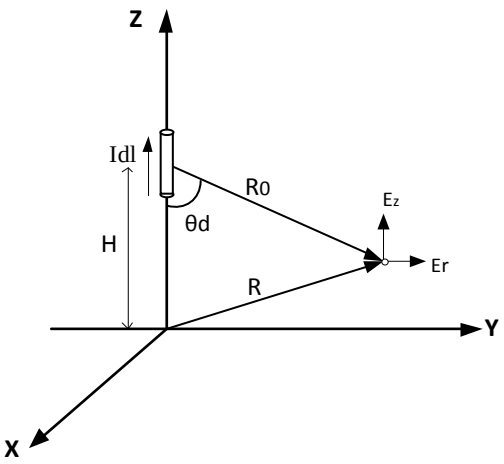

Figure 40 Vertical electric current dipole radiation in the free-Space

As the vertical dipole is defined to have z-directed current, the magnetic vector potential will have only z-axis component and will be given by:

$$A_z = \frac{\mu_0 Idl}{4\pi R_0} e^{-jk_0 R_0} e^{j\omega t} \tag{4.1}$$

The term $e^{j\omega t}$ will be omitted during the following. Once the magnetic vector potential is obtained, the magnetic field components can be also found [16] by using:

$$H = \frac{1}{\mu} \nabla \times A \tag{4.2}$$

The electric radiated fields due to a vertical current element in the free space can be calculated by the Maxwell equations. Selecting a cylindrical coordinates system as the most convenient for the vertical current dipole representation, the magnetic and electric field components can be calculated from:

$$H_{\phi 0} = \frac{jk_0 Idl}{4\pi R_0} \sin\theta_d \left(1 + \frac{1}{jk_0 R_0}\right) e^{-jk_0 R_0} \tag{4.3}$$

$$E_{r0} = \frac{jk_0 Idl Z_0}{4\pi} \sin\theta_d \cos\theta_d \left(1 + \frac{3}{jk_0 R_0} + \frac{3}{(jk_0 R_0)^2}\right) \frac{e^{-jk_0 R_0}}{R_0} \tag{4.4}$$

$$E_{z0} = \frac{-jk_0 Idl Z_0}{4\pi} \left(\sin^2\theta_d + (1 - 3\cos^2\theta_d) \left[\frac{1}{jk_0 R_0} + \frac{1}{(jk_0 R_0)^2}\right]\right) \frac{e^{-jk_0 R_0}}{R_0} \tag{4.5}$$

Expressions (4.3), (4.4) and (4.5) allow calculating the radiated electromagnetic fields in free space due to a vertical current dipole.

4.1.1 Radiation above a perfectly conductive Ground

This section deals with the radiation of a vertical current dipole located above a perfectly conducting ground. For simplicity the dipole coincides with the z-axis direction and it is located at a height H from the XY plane. Relevant geometry for the problem under analysis is depicted in Figure 41.

The radiation above a perfectly conductive ground can be addressed by means of the image theory [16][49]. In this case, the field at the receiver point is the superposition of the direct field produced by the source, and the field produced by an image source which represents the effect of the presence of the conducting ground.

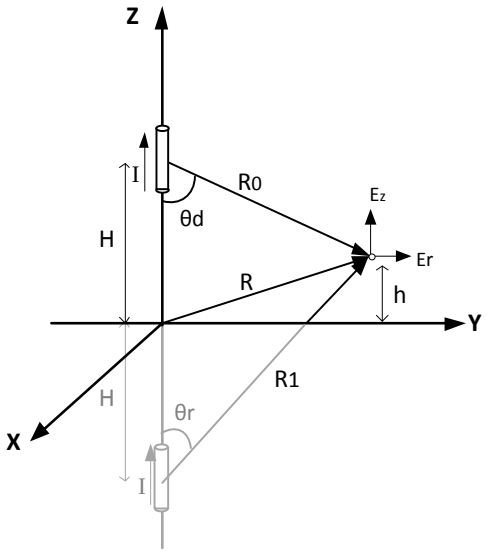

Figure 41 Radiation above perfectly conducting ground

Taking into account the geometry presented in Figure 41 the radiated electric field generated by the source and its image can be calculated respectively by:

$$E_{r0} = \sin\theta_d \cos\theta_d \left(1 + \frac{3}{jk_0R_0} + \frac{3}{(jk_0R_0)^2}\right)\frac{e^{-jk_0R_0}}{R_0} \tag{4.6}$$

$$E_{r1} = \sin\theta_r \cos\theta_r \left(1 + \frac{3}{jk_0R_1} + \frac{3}{(jk_0R_1)^2}\right)\frac{e^{-jk_0R_1}}{R_1} \tag{4.7}$$

The total horizontal component of the radiated electric field can be calculated by the sum of (4.6) and (4.7) by:

$$E_r = \frac{jk_0IdlZ_0}{4\pi}(E_{r0} + E_{r1}) \tag{4.8}$$

The same for the vertical radiated electric field component,

$$E_{z0} = \left(\sin^2\theta_d + (1 - 3\cos^2\theta_d)\left[\frac{1}{jk_0R_0} + \frac{1}{(jk_0R_0)^2}\right]\right)\frac{e^{-jk_0R_0}}{R_0} \quad (4.9)$$

$$E_{z1} = \left(\sin^2\theta_r + (1 - 3\cos^2\theta_r)\left[\frac{1}{jk_0R_1} + \frac{1}{(jk_0R_1)^2}\right]\right)\frac{e^{-jk_0R_1}}{R_1} \quad (4.10)$$

Finally, the total vertical component can be calculated adding (4.9) and (4.10):

$$E_z = \frac{-jk_0IdlZ_0}{4\pi}(E_{z0} + E_{z1}) \quad (4.11)$$

Next sections will consider a finite conductively ground where the image theory cannot be used as presented in this section.

4.1.2 Radiation above a Flat Homogeneous ground

In this section a finite conducting ground is taken into account for the radiated field calculations. The assumption of perfectly conducting ground is unpractical when poorly conductive grounds are present. Figure 42 depicts the scenario and the relevant geometry for this case.

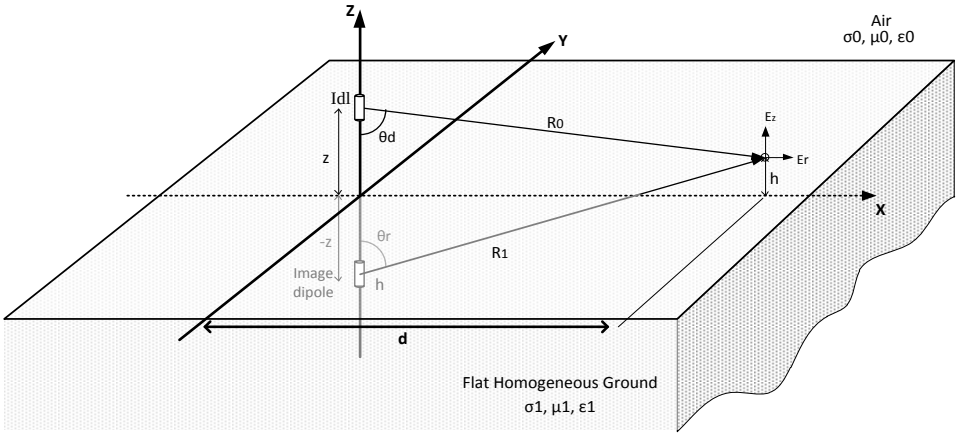

Figure 42 Vertical Current Dipole above Homogeneous Finitely Conducting Ground

Radiation above homogeneous ground represents a difficulty in evaluating the effect of the ground presence. This problem was addressed initially by Sommerfeld, who proposed a solution in order to calculate the radiated electric field for a current dipole [16].

4.1.2.1 Sommerfeld's Solution

The Sommerfeld´s solution consists on a plane wave expansion of the magnetic vector potential contribution due to the homogeneous ground presence. Once the boundary conditions are forced at the air-ground interface, the total magnetic vector potential leads to an expression where two terms of the total solution coincide with the case of the perfectly conducting ground, and a third term includes the finitely conductive ground effect [16]. This latter term has been historically named the surface wave term, referring to a wave that travels into the ground and modify the total fields above the ground [16].

The expression for calculating the magnetic vector potential by using the Sommerfeld's approach can be written as [16]:

$$A_z = \frac{\mu_0 I dl}{4\pi}\left(\frac{e^{-jk_0R_0}}{R_0} + \frac{e^{-jk_0R_1}}{R_1} - 2P\right) \tag{4.12}$$

Where, the surface wave term is determined by:

$$P = -{k_0}^2 \int_0^\infty \frac{\left(\lambda^2 - {k_1}^2\right)^{1/2}}{{k_1}^2\left(\lambda^2 - {k_0}^2\right)^{1/2} - {k_0}^2\left(\lambda^2 - {k_1}^2\right)^{1/2}} J_0\left(\lambda\sqrt{{R_0}^2 - (z-h)^2}\right) e^{-\left(\lambda^2 - {k_1}^2\right)^{1/2}(z+h)} \frac{\lambda d\lambda}{\left(\lambda^2 - {k_0}^2\right)^{1/2}} \tag{4.13}$$

The integrand of (4.13) is highly oscillatory and slow convergent. Hence, the Sommerfeld´s equations must to be solved by sophisticated numerical methods [16][53].

In literature, several techniques have been proposed in order to evaluate the Sommerfeld´s integrals by efficient numerical methods. However, when several frequencies must be taken into account, the rigorous solution becomes computationally prohibitive. Next subsection present one of the most popular approaches for the Sommerfeld´s integral solution.

4.1.2.2 Norton´s Approach

Norton's approach is one of the most used formulations in calculating radiated fields over a flat homogeneous ground. In this approximation, the electromagnetic field can be calculated taking into account the lossy-ground effects without solving directly the Sommerfeld´s integrals. By means of the Norton's approach, some considerations are made regarding the ground conductivity values and the geometrical distances in order to simplify the integral in the Sommerfeld's formulation [16][22][50].

For the horizontal electric field component, the direct field remains unaltered as in the free space [16]:

$$E_{r0} = \sin\theta_d \cos\theta_d \left(1 + \frac{3}{jk_0R_0} + \frac{3}{(jk_0R_0)^2}\right)\frac{e^{-jk_0R_0}}{R_0} \tag{4.14}$$

The contribution on the horizontal electric field due to the ground presence can be written as [16]:

$$E_{r1} = \sin\theta_r \cos\theta_r \left(\Gamma_r + (1-\Gamma_r)\frac{1}{jk_0R_1} + \frac{3}{jk_0R_1} + \frac{3}{(jk_0R_1)^2}\right)\frac{e^{-jk_0R_1}}{R_1} - (1-\Gamma_r)\Delta_0 \sin\theta_r \left[F(w) + \frac{1}{2jk_0R_1}\right]\frac{e^{-jk_0R_1}}{R_1} \quad (4.15)$$

Finally, the total horizontal field can be calculated by:

$$E_r = \frac{jk_0IdlZ_0}{4\pi}(E_{r0} + E_{r1}) \quad (4.16)$$

For the vertical electric field, the direct contribution can be also calculated as in free-space by:

$$E_{z0} = \left(\sin^2\theta_d + (1-3\cos^2\theta_d)\left[\frac{1}{jk_0R_0} + \frac{1}{(jk_0R_0)^2}\right]\right)\frac{e^{-jk_0R_0}}{R_0} \quad (4.17)$$

The contribution on the vertical electric field due to the ground presence can be written as [16]:

$$E_{z1} = \left(\Gamma_r \sin^2\theta_r + (1-\Gamma_r)F(w)\sin^2\theta_r + 2\cos\theta_r\,\Delta_0\left(\frac{1}{jk_0R_1}\right) + (1-3\cos^2\theta_r)\left[\frac{1}{jk_0R_1} + \frac{1}{(jk_0R_1)^2}\right]\right)\frac{e^{-jk_0R_1}}{R_1} \quad (4.18)$$

Finally, the total vertical field component can be calculated by:

$$E_z = \frac{-jk_0IdlZ_0}{4\pi}(E_{z0} + E_{z1}) \quad (4.19)$$

In expression (4.15) and (4.18), Γ_r represents the reflection coefficient and can be calculated by:

$$\Gamma_r = \frac{\cos\theta_r - \Delta_0}{\cos\theta_r + \Delta_0} \quad (4.20)$$

where,

$$\Delta_0 = u\sqrt{1-u^2\sin^2\theta_r} \quad (4.21)$$

and

$$u = \frac{k_0}{k_1} \quad (4.22)$$

$k_1 = \sqrt{-j\omega\mu_1(\sigma_1 + j\omega\varepsilon_1)}$ is the propagation constant for the lossy ground and $k_0 = \omega\sqrt{\mu_0\varepsilon_0}$ is the propagation constant for air. The Δ_0 function is also called the normalized surface impedance.

The $F(w)$ function also present in (4.15) and (4.18), is known as the *attenuation function* and can be calculated by:

$$F(w) = 1 - j\sqrt{\pi w}e^{-w}\,\mathrm{erfc}\left(j\sqrt{w}\right) \tag{4.23}$$

The function w is expressed by:

$$w = \frac{-jk_0R_1^3}{2d^2}(\cos\theta_r + \Delta_0)^2 \tag{4.24}$$

The attenuation function proposed by Norton has been compared with the rigorous solution from the Sommerfeld integrals and it has shown a good agreement for almost all far-field situations and for the near field when considerably good ground conductivity is assumed. It must be taken into account for calculations using the Norton´s approach, that the proposed results have used the approximation that $k_1^2 \gg k_0^2$ [18].

In Figure 43(a) there is a comparison of the attenuation function magnitude between the Sommerfeld's solution and the Norton´s approach when a vertical dipole is radiating at 1MHz over a flat ground, and with ρ=100Ωm and ε=10ε_0 in resistivity and permittivity respectively.

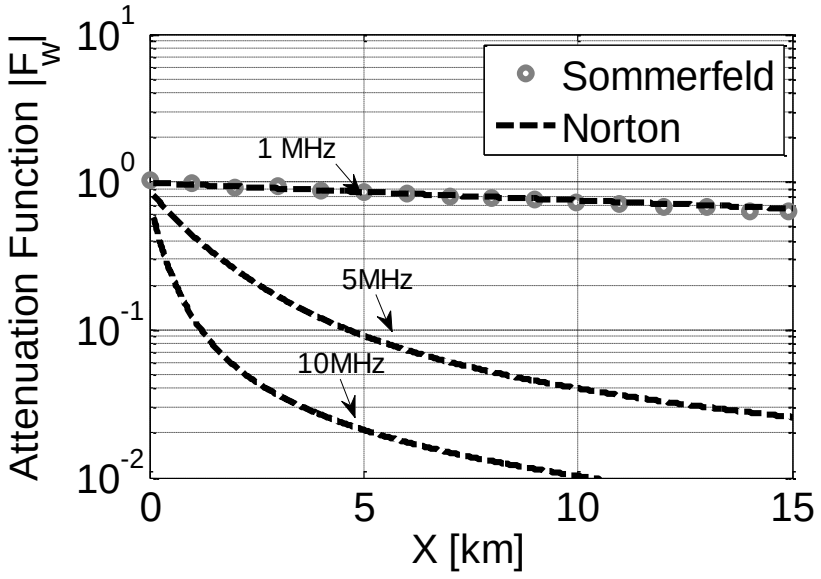

Figure 43 Attenuation Function Magnitude Comparison for a Vertical Current-Dipole above a Flat Homogeneous Ground. Norton Approach (dashed lines) and Sommerfeld's solution (circles) taken from [52]

Figure 43 shows that there is a good agreement between the two approaches. The effects on the attenuation function due to variations in the dipole excitation frequency were also calculated by using the Norton´s approach for the frequencies 5MHz and 10MHz.

Once the attenuation function has been calculated, the horizontal electric field can be evaluated assuming a current-dipole magnitude. For this case the current-dipole magnitude is 1A; the observation points for the radial-electric field calculations were assumed to be at 10m above the ground surface. Figure 44 presents the effect of the excitation frequency on the horizontal electric field. Near the source, the differences are representative.

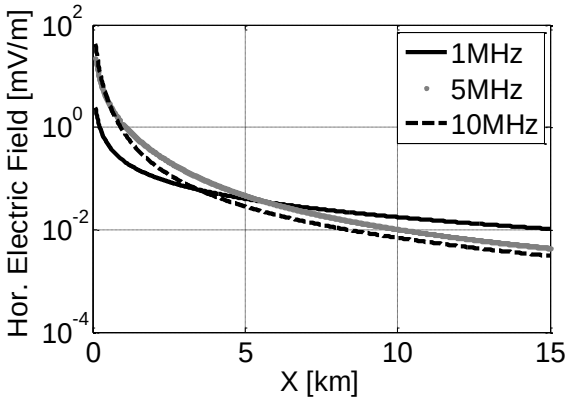

Figure 44 Radiated Horizontal Electric Field (10m in height) along the propagation path

4.2 Radiating Vertical-Current Dipole over an Inhomogeneous and Irregular Ground (far-field region).

Most of the popular approaches for calculating radiated electromagnetic fields in presence of irregular and in-homogeneous ground have been based on the Compensation theorem and on the Green´s theorem. Both of them lead to two-dimensional integral equation formulations for the field component under evaluation [16]. Once the two-dimensional integral equation has been formulated, an assumption of radial symmetry and the introduction of elliptic coordinates allow the formulation of a one-dimensional integral equation along the radial direction. Some of the main results will be presented in this section. A complete deduction can be found in [16][53].

4.2.1 Green´s Theorem Approach

Consider a vertical current dipole above an irregular ground as presented in Figure 45.

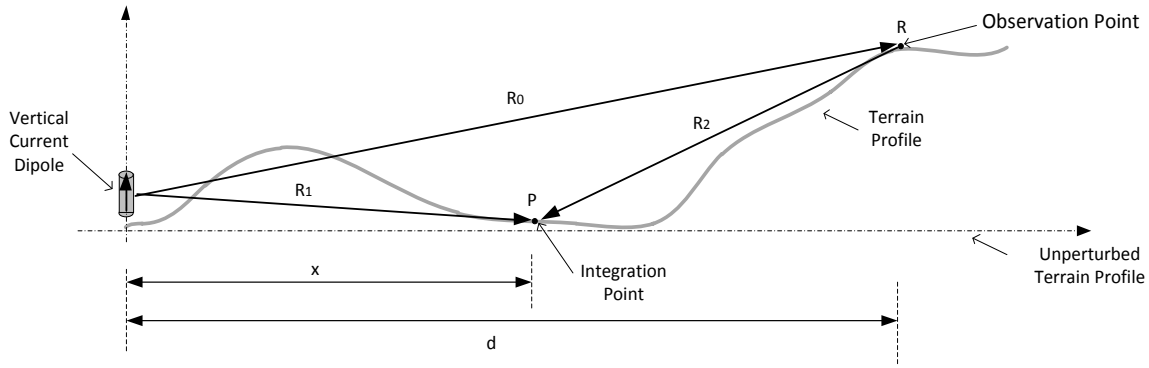

Figure 45 Relevant Geometry Irregular Terrain profile.

In general, the solution of the electromagnetic field must satisfy the non-homogenous Helmholtz equation with a set of boundary conditions related to the ground conductivity inhomogeneities and its height profile. Consider the non-homogenous Helmhotlz equation for a scalar field ψ:

$$\nabla^2\psi + k_0^2\psi = -4\pi\tau(x,y,z) \tag{4.25}$$

where ψ will represent the vertical electric field component, $k_0 = \omega/c = \omega\sqrt{\mu_0\varepsilon_0}$ is the propagation constant in the air and $\tau(x,y,z)$ is the vertical dipole current density in the space, which is defined to be zero at every point of the region except at the current-dipole location. The scalar function ψ will include in its solution the influence of the ground characteristics once the boundary conditions have been applied. This influence can be interpreted as a modification of the free-space solution due to the presence of the ground characteristics; It is usually called the path-gain function or the attenuation function. The scalar field ψ at the observation point can be calculated as:

$$\psi(R) = \mathrm{W}(R)\frac{e^{-jk_0R_0}}{R_0} \tag{4.26}$$

where $\mathrm{W}(R)$, represents the path gain function calculated at the observation point. Function $\mathrm{W}(R)$ will contain all the modifications introduced by the presence of non-homogeneities and irregularities of the ground and its effects on the observation point.

The free-space solution ψ_0, is calculated by:

$$\psi_0(R) = \mathrm{g}(R)\frac{e^{-jk_0R_0}}{R_0} \tag{4.27}$$

Where $\mathrm{g}(R)$ represents the radiation pattern of the transmitter dipole. As ψ represents the vertical electric field due to a vertical current dipole, the radiation pattern function and its contribution to the observation point can be found for the far-field region by:

$$g(R) = \frac{-jk_0 IdlZ_0}{4\pi}(\sin^2\theta_d) \tag{4.28}$$

Boundary conditions must be applied depending on the component that the scalar function ψ is representing. When ψ is representing the vertical electric field due to a vertical-current dipole, the boundary condition at the interface air-ground can be derived by the Leontovich´s method. The normal continuity condition for vertical polarization can be written as [16]:

$$\frac{\partial\psi(P)}{\partial n} = jk_0\Delta_0\psi(P) \tag{4.29}$$

where Δ_0 the normalized surface impedance presented in section 4.1.2.2 and is given by:

$$\Delta_0 = \frac{k_0}{k_1}\sqrt{1-\left(\frac{k_0}{k_1}\right)^2} \tag{4.30}$$

Using the Green's theorem and rearranging some terms of the equations (a complete deduction can be found in [53]), the unknown path function at the observation point $W(R)$ can be calculated by:

$$W(R) = g(R) - \frac{jk_0}{4\pi}\iint_{\substack{\text{ground's}\\ \text{surface}}} W(P)e^{-jk_0[R_1+R_2-R_0]}\frac{R_0}{R_1R_2}\left[\Delta(P) + \left(1+\frac{1}{jkR_2}\right)\frac{\partial R_2}{\partial n}\right]ds \tag{4.31}$$

Using elliptical coordinates and considering the inhomogeneities and irregularities in radial direction only, the two-dimensional integral equation presented above can be reduced to a one-dimensional equation as:

$$W(d) = g(d) - \left(\frac{jk_0 d}{2\pi}\right)^{\frac{1}{2}}\int_0^d W(x)\left[\Delta(x) + \frac{dR_2}{dn}\right]e^{-jk_0[R_1+R_2-R]}\left(\frac{1}{\sqrt{x(d-x)}}\right)dx \tag{4.32}$$

The expression presented before, is a general formulation for taking into account in homogeneities and irregularities along the propagation path in the far-field region. From this expression, the mixed-path condition can be also derived simplifying some terms [53].

4.2.2 Radiation fields over an inhomogeneous ground.

The propagation path to be considered in the following corresponds to a vertically stratified ground or well-known as a ***mixed-path*** [18]. This in-homogeneity is described as vertical abrupt change of conductivity along the propagation path as is shown in Figure 46. There can be several configurations for mixed paths depending on the number of conductivity changes. Figure 46(a)

depicts the general geometry for a mixed-path of two-sections and Figure 46(b) for a mixed-path of three-sections.

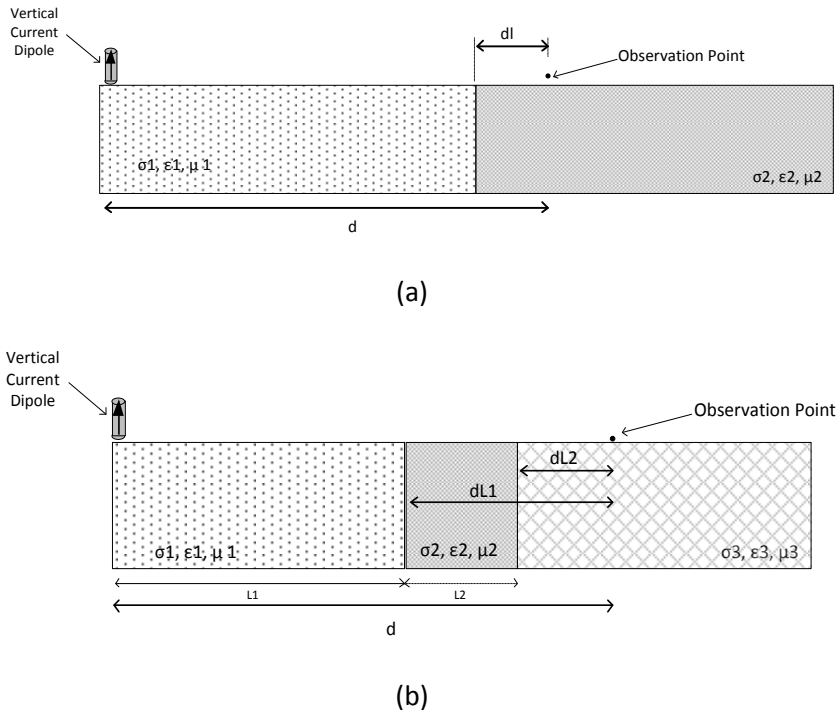

Figure 46 (a) Two-Sections Mixed-Path Condition (b) Three-Section Mixed-Path

One of the most popular analysis of the propagation effect due to the presence of a mixed path is that proposed by Wait based on the compensation theorem approach [55][56][57][58], where the attenuation function at the observation point can be expressed by:

$$W(d) = W_1(d) - \left(\frac{jk_0 d}{2\pi}\right)^{1/2} [\Delta_2 - \Delta_1] \int_0^{dl} \frac{W_1(d-x)W_2(x)}{\sqrt{x(d-x)}} dx \qquad (4.33)$$

The attenuation functions W_1 and W_2 are the attenuation functions for regions 1 and segment 2 respectively. The solution proposed by Wait assumes that both the vertical-current dipole and the observation point are located at the ground surface and the observation point must be in the far field region.

The attenuation functions W_1 and W_2 are obtained using the same idea as the attenuation function proposed by Norton when a homogeneous ground is considered. Nevertheless, in this case W_1 and W_2 will be dependent on the normalized impedance at each position in order to take into account the longitudinal change of the ground conductivity. Some variables presented in the attenuation function derived in the Norton's approach have been redefined with the aim for maintaining the same notation from Wait. The attenuation function can be written as:

$$W(d) = 1 - j\sqrt{\pi P_n}e^{-P_n}\,\mathrm{erfc}\left(j\sqrt{P_n}\right) \tag{4.34}$$

Where the function P_n, is described by:

$$P_n = \frac{-jk_0 d}{2}(\Delta_n)^2 \tag{4.35}$$

It is worth noting that the expression for P_n corresponds to the expression for w in the Norton approach when the radiating dipole is on the ground leading to $R = d$, $\cos\theta_r = 0$ and $\sin\theta_r = 1$.

For each region, the normalized impedance must be calculated as:

$$\Delta_n = u\sqrt{1-u^2} \tag{4.36}$$

Where,

$$u = \frac{k_0}{k_n} \tag{4.37}$$

When multiples vertical changes on conductivity occur along the propagation path, the expression proposed by Wait can be extrapolated by taking into account the presence of each mixed path and their mutual interaction along the path until reaching the observation point. As an example, the attenuation function for a three-section mixed-path such as presented in Figure 46(b) can be calculated by [57]:

$$\begin{aligned} W(d) = W_3(d) - \left(\frac{jk_0 d}{2\pi}\right)^{1/2}\Bigg[&\left([\Delta_1 - \Delta_3]\int_0^{L1}\frac{W_3(d-x)W_1(x)}{\sqrt{x(d-x)}}dx\right) \\ &+\left([\Delta_2 - \Delta_3]\int_{L1}^{L1+L2}\frac{W_3(d-x')W_{1-2}(x')}{\sqrt{x'(d-x')}}dx'\right)\Bigg] \end{aligned} \tag{4.38}$$

where $W_{1-2}(x')$ is the attenuation function for the first mixed-path of two sections, which can be calculated as presented before:

$$W_{1-2}(x') = W_1(x') - \left(\frac{jk_0 d}{2\pi}\right)^{1/2}\left[[\Delta_2 - \Delta_1]\int_0^{x'}\frac{W_1(x'-\alpha)W_2(\alpha)}{\sqrt{x'(x'-\alpha)}}d\alpha\right] \tag{4.39}$$

In order to validate the implementation of Wait´s proposal for the mixed-path problem, Figure 47 presents its comparison with the approach presented by Ott for a frequency of 10MHz [54]. For this case, a three-section mixed-path (sea-land-sea) is used. Geometrical parameters are shown in Figure 47(a). The results of the comparison are shown in Figure 47(b) and Figure 47(c) respectively.

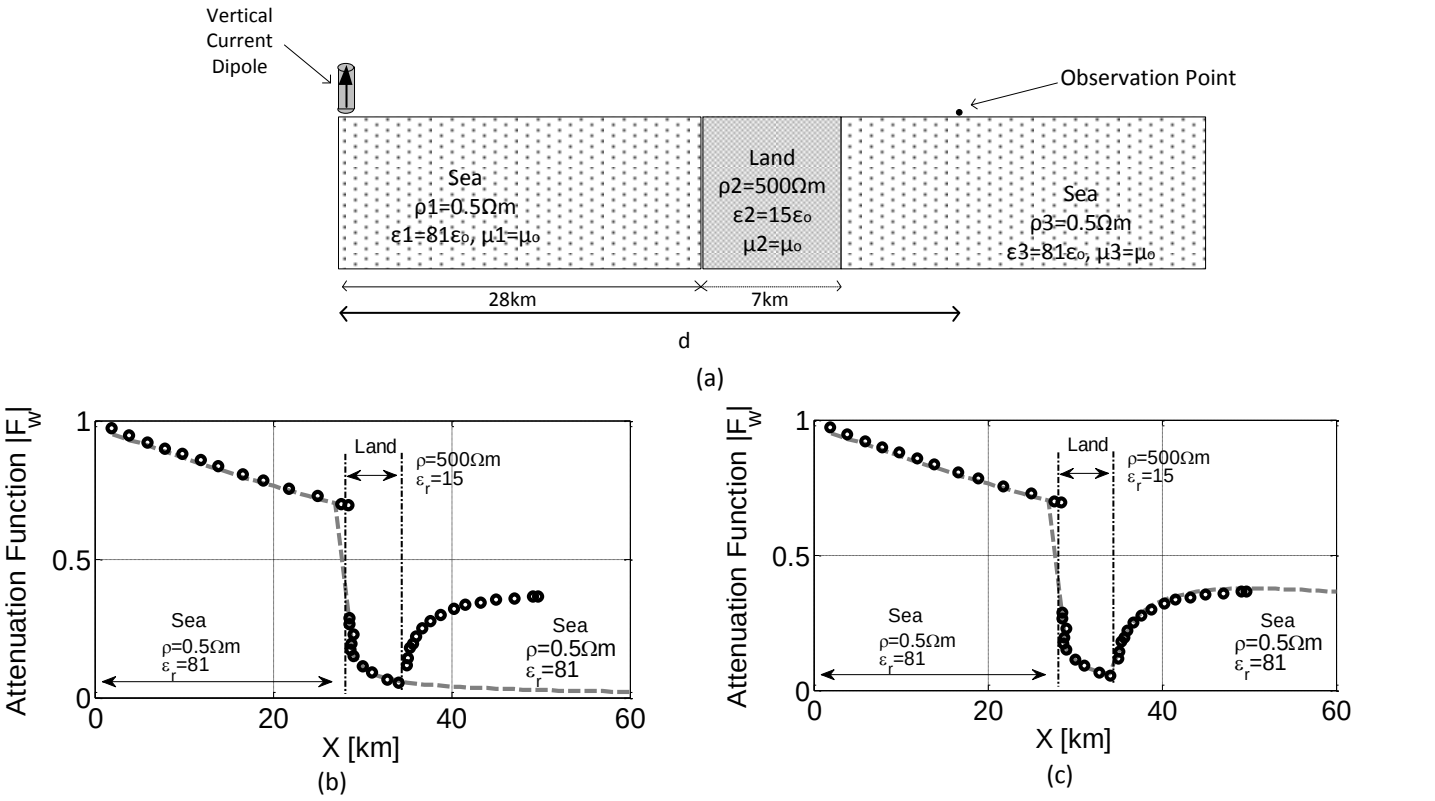

Figure 47 Attenuation Function for a Mixed-Path (dashed: Wait´s Approach, circles: Ott's integral presented in [54]) (a) Relevant Geometry for three section Mixed-Path (b) Wait's Attenuation Function for Two Sections ρ1=0.5Ωm/ ρ2=500Ωm (c) Wait's Attenuation Function for Three-Sections ρ1=0.5Ωm/ ρ2=500Ωm / ρ3=0.5Ωm

Once the attenuation function has been calculated, the radiated fields can be evaluated along the path for different frequencies. Figure 48 presents the calculation of the electric field components along the three-section mixed-path when three frequencies are taken into account.

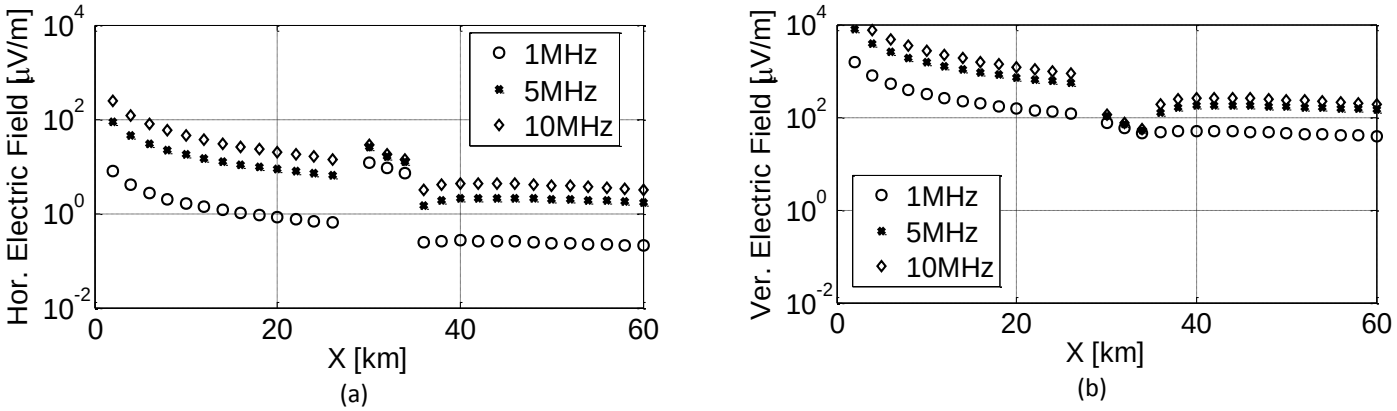

Figure 48 Radiated Electric Field Components along the Path at 10m in height (a) Horizontal Electric Field Component (b) Vertical Electric Field Component

As can be seen from Figure 48, the electric field components are affected by the presence of the mixed path. For this case, the change from a higher conductivity ground to a lower one, increases the field magnitude for the horizontal electric field component and decreases the magnitude of

the vertical one. The effect of increasing the magnitude is also called as the “recovery effect” and it has been evidenced experimentally [18][56].

4.2.3 Radiation fields over an irregular ground.

An alternative integral equation was proposed by Ott [54] for the calculation of the attenuation function not only when ground homogeneities are present, but also when irregular terrain is present along the propagation path. By using the Ott´s approach [54], several terrain profiles can be taken into account. In order to analyze the effects of the irregular ground on the electric field components a Gaussian shape was used as an obstacle. This kind of shape has the advantage of having a continuous derivative function over distance and soft changes. The function that describes the profile of the irregularities was defined by:

$$y = He^{-\left(\frac{x-x_0}{b}\right)^2} \tag{4.40}$$

and its derivate function can be calculated as:

$$y' = -2H\left(\frac{x-x_0}{b^2}\right)e^{-\left(\frac{x-x_0}{b}\right)^2} \tag{4.41}$$

where, x_0 represents the center of the Gaussian curve, H represents the height and b is an input parameter for controlling the base-length.

The first path under analysis was a Gaussian ridge and the second one a Gaussian cliff with 500m in height and deep respectively. The center of the Gaussian shape was located at $x_0 = 7.5km$ with a base-length parameter $b = 1km$. Figure 49(a) and Figure 49(b) depicts the terrain profiles under analysis.

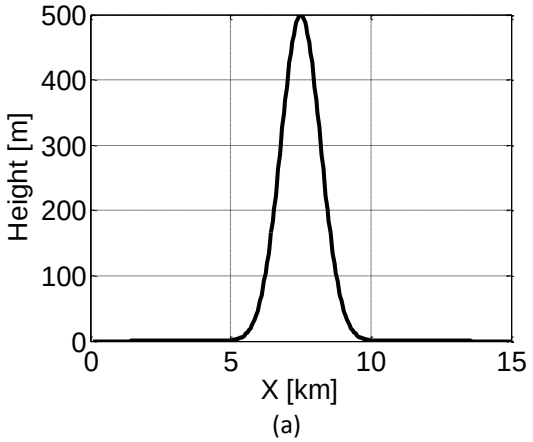

(a)

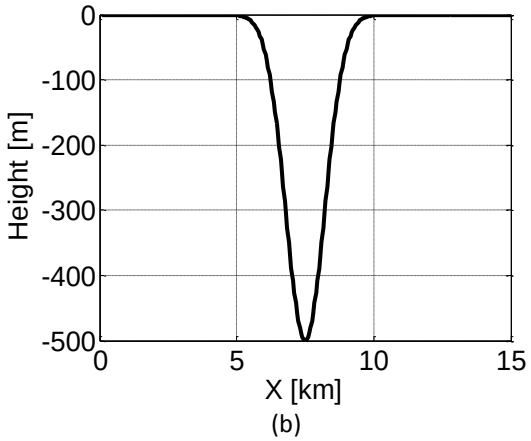

(b)

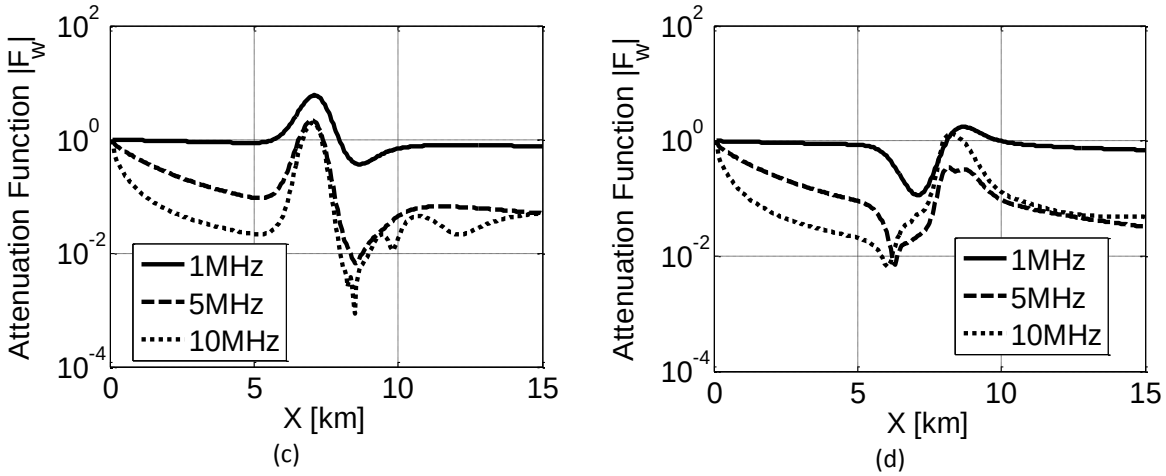

Figure 49 Irregular Propagation Path and their Attenuation Function Magnitude. (a) Ridge Terrain Profile (b) Attenuation Function for a Ridge Terrain Profile (c) Cliff Terrain Profile (d) Attenuation Function for a Cliff Terrain Profile

The attenuation function magnitudes were calculated for both profiles at 1MHz, 5MHz and 10MHz for the current dipole frequency. Depending on the irregularity, the attenuation function changes. As can be seen in Figure 49(b), the attenuation function related to the Gaussian ridge has an attenuation magnitude greater than the unity along the first part of the ridge (where the derivative of the profile is positive) and decreases after the top of the ridge. The frequency dependence of the attenuation function shows that for higher frequencies the attenuation function raises and decreases faster than for lower ones.

Figure 50 presents the calculated radiated electric field components when the ridge and the cliff described before are present along the propagation path. As can be seen from Figure 50(a) and (b), the ridge presence along the propagation path increases the field magnitude along the positive slope for each geometry.

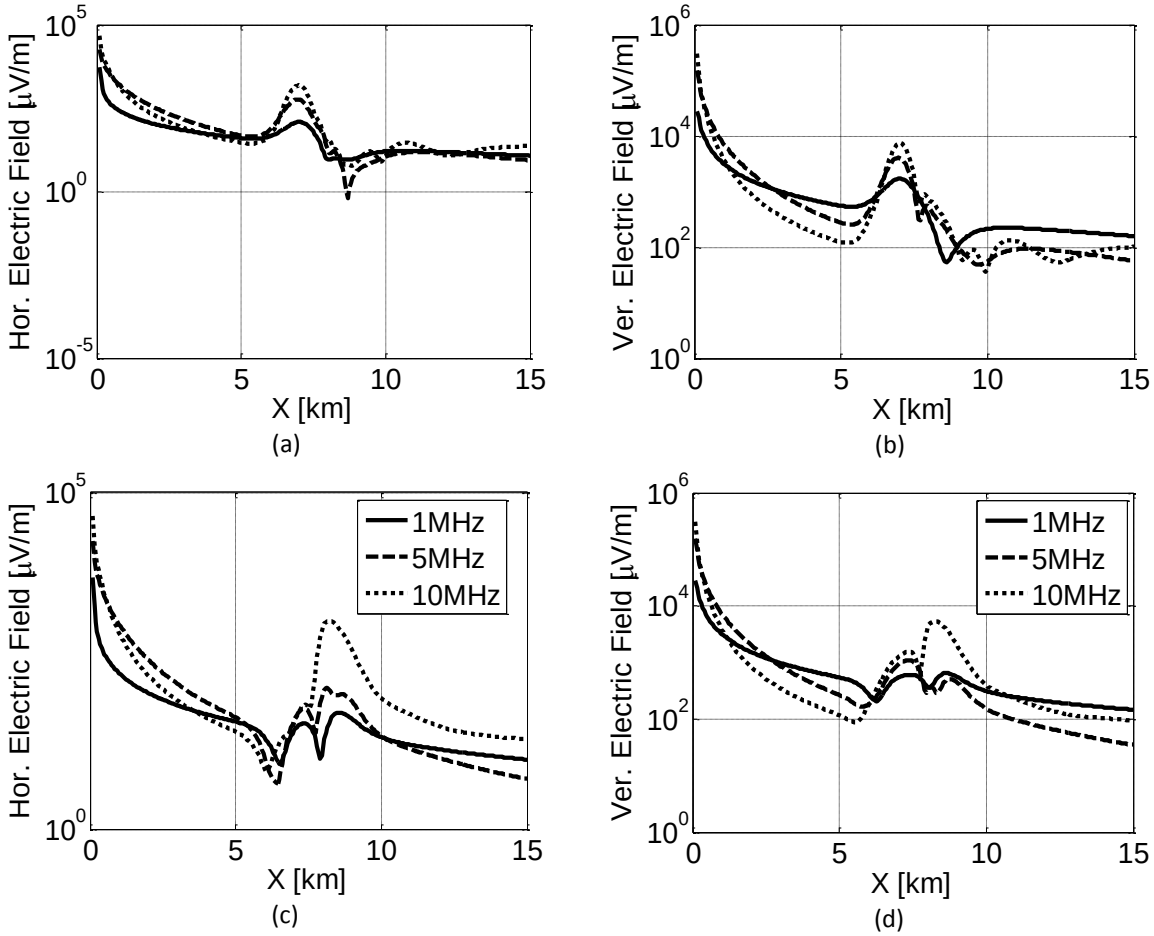

Figure 50 Irregular Ground Effect on Radiated Electric Fields. Gaussian Ridge: (a) Horizontal Electric Field (b) Vertical Electric Field. Gaussian Cliff: (c) Horizontal Electric Field (d) Vertical Electric Field

It can be also seen, that the effect is more representative as the excitation frequency increases. As it is shown in Figure 50, the electric fields components are more affected for the excitation frequency of 10MHz. This occurs because the wave-length becomes comparable with the geometrical dimensions of the terrain irregularity.

4.3 Radiating Vertical-Current Dipole over an Inhomogeneous and Irregular Ground (near-field region).

As it was discussed before, the calculation of the near field radiation could be carried out using the Sommerfeld's formulation. However, the Norton's approach has shown its validity for calculating radiated electric fields within a close range distance from the radiating dipole. Next sections show the effects of the propagation path in the near field.

4.3.1 Radiated Fields over Homogeneous and Inhomogeneous Flat Ground

The solutions presented before have been derived under several assumptions, especially the azimuthal symmetry of the mixed-path problem and the far field assumption for the radiated fields. In order to analyze the validity of the FDTD method in the near field region, a comparison was made with the Norton´s and Wait's approaches for the calculation of radiated fields above a homogeneous and over a mixed-path structure. A three section mixed-path condition (sea/land/sea) was assumed. The ground conductivity changes were ρ_1=0.5Ωm/ρ_2=500Ωm/ρ_3=0.5Ωm with a relative permittivity of ε_{r1}=81/ ε_{r2}=15/ε_{r3}=81 respectively. The boundaries of the vertical stratification were located at X_1=492.5m X_2=842.5m.

A non-regular mesh for the FDTD simulation was performed using the non-regular parabolic-meshing algorithm proposed in this thesis. The parameters were set to 5m and 20m for the minimum and maximum spacing size respectively with a maximum spacing-rate factor of 1. The Z-axis was meshed by regular discretization. The total space of simulation was 4000x4000x1000m^3 with the dipole located at 2.5m in height above the ground at the coordinate X_0=1000m, Y_0=1500m. The simulation space truncation was achieved by using absorbing 2nd order Liao´s boundaries. The ground was simulated by means of a 200m height conductive block and the total computational domain was 236x186x200 of non-regular Yee's cells. Horizontal electric fields were evaluated at 10m above the ground when the radiating source is represented by a voltage source with 50Ω in internal resistance and a sinusoidal waveform of 1MHz in frequency.

As the implementation of the excitation source was different in both methods, the current magnitude of the vertical dipole in the Norton´s and Wait's approach was adjusted in order to match the radiated electric field values for the homogeneous condition in the FDTD simulation. The results are shown in Figure 51.

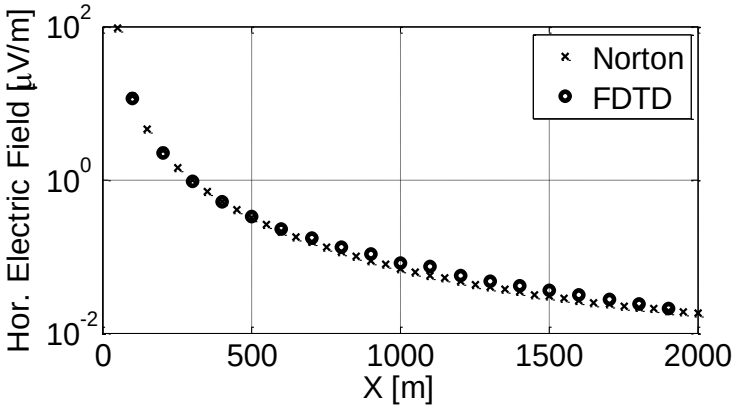

(a)

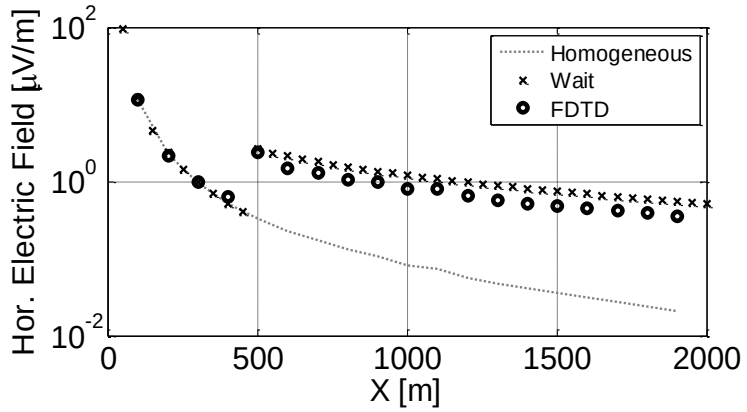

(b)

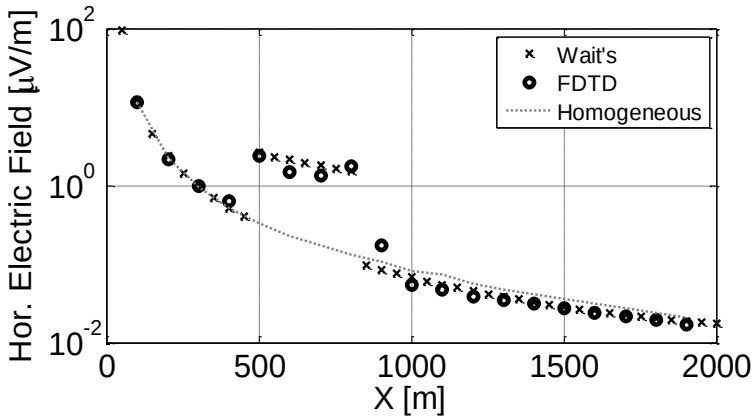

Figure 51 Horizontal Electric Field Component due to a vertical current dipole within the Near Field Range (circles: FDTD, cross: Wait´s Approach) (a) Homogeneous Case (b) Two-Section Mixed path (c) Three Section Mixed-path

The results presented in Figure 51 show that the FDTD method results are in good agreement with those results obtained by Norton's and Wait´s approaches for the considered ground conductivities.

The expressions used to calculate the radiated electric field components presented by Norton [16] were corrected by King [50] by means of two different factors calculated at the observation point: the reflection coefficient due to the local impedance surface, and the attenuation function which can be seen as an accumulated effect due to the presence of the ground.

In order to show the influence of the attenuation function on the horizontal radiated electric field, Figure 52 presents the radiated horizontal electric field component calculated taking into account the attenuation function, and the results assuming the attenuation function to be equal to the unity. As it can be seen, the attenuation function does not represent an important factor on the calculation of the electric radiated fields for relative low frequencies such as 1MHz. However, its effect becomes important for higher frequencies values.

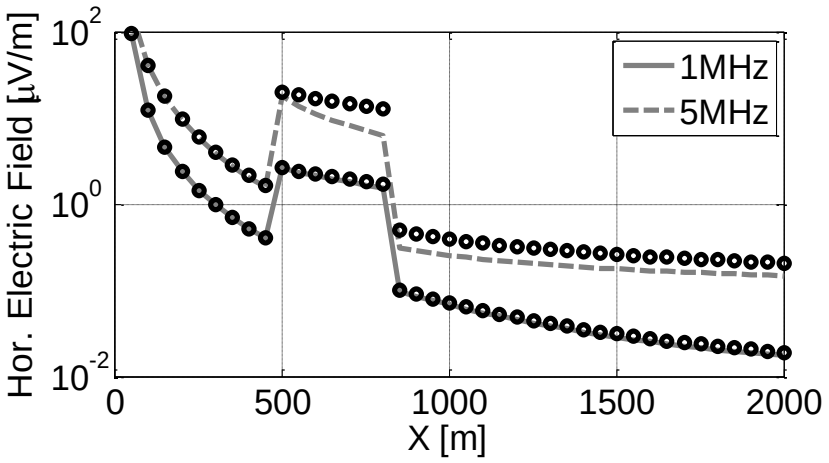

Figure 52 Attenuation Function influence in the near-field Horizontal Electric Field Calculation

Other important factor influencing the attenuation function values is the ground resistivity. Figure 53 presents the frequency response of the attenuation function magnitude when two ground resistivity values: 100Ωm and 1000Ωm are considered for the homogeneous ground. The frequency response has been calculated at four different distances: 100m, 500m, 1000m and 2000m from the radiating dipole.

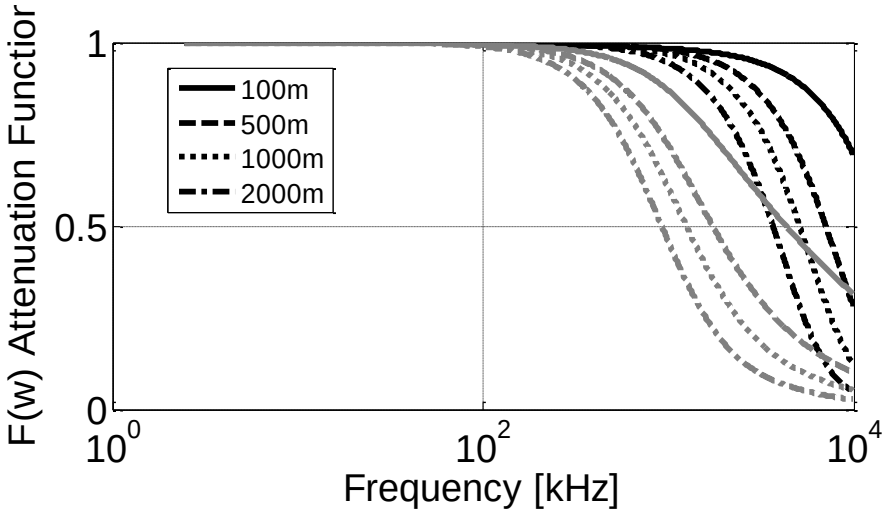

Figure 53 Attenuation Function Magnitude Frequency Response at different distances from the radiating dipole (gray lines: 1000Ωm, black lines: 100Ωm)

As can be seen from Figure 53 the attenuation function not only presents lower cut-off frequencies but also a different behavior at higher frequencies.

An additional simulation for a three section mixed-path was performed by means of the FDTD method, in order to observe the behavior when the ground conductivity change occurs near the current dipole location. In this case the boundaries between the ground sections were located at

X_1=250m and X_2=450. A voltage dipole oscillating at 1MHz was placed at 1m above a mixed-path of three sections; calculations of the e peak value were obtained once the steady-state of electric field waveforms was achieved. The simulation in the FDTD was performed using regular meshing with cubic cells with 5x5x2m^3 in volumes. The total simulation volume space was 50x900x2000m^3. The computational domain was truncated by means of CPML boundaries.

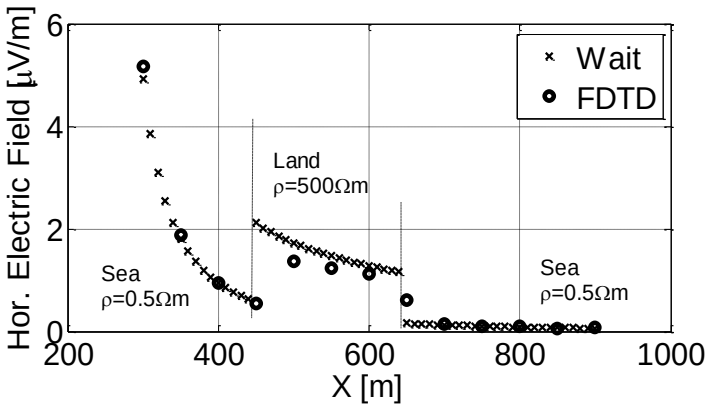

(a)

Figure 54 Validity of the Wait formula for Mixed-Path of Three sections (a) Horizontal Electric Field

As can be seen from Figure 54 there is a good agreement between the results.

4.3.2 Radiated Fields over Irregular Ground

As it was discussed before, by means of the integral equation proposed by Ott [54] it is possible to calculate the attenuation function in the far field region when there are irregular profiles along the propagation path.

In order to evaluate this effect, a monochromatic oscillating voltage source with 50Ω in internal resistance was placed at 2.5m above the ground and an obstacle with 50m in height and 400m in length was included in the propagation path. A non-regular mesh FDTD simulation was performed using the non-regular parabolic-meshing algorithm proposed in this thesis. The parameters were set to 5m and 20m for the minimum and maximum spacing size respectively with a maximum spacing-rate factor of 1. The Z-axis was meshed by regular discretization. The total space of simulation was 4000x3000x1000m^3 and the dipole was located at the coordinate X_0=1000m, Y_0=1500m. In order to truncate the simulation space, absorbing 2nd order Liao´s boundaries were implemented. The ground was simulated assuming 0.5Ωm in ground resistivity and ε_r=81 in relative permittivity. Figure 55(a) shows the inclusion of the terrain irregularity in the FDTD method. A finer mesh that can be seen near 1000m was included for a better representation of the source.

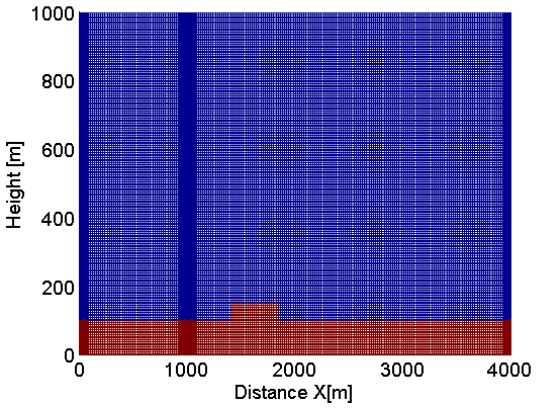

(a)

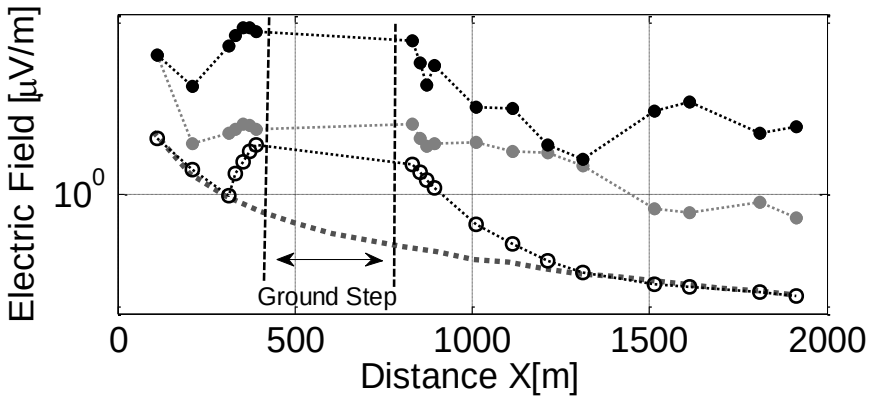

(b)

Figure 55 Irregular ground effect on radiated field in the near field (a) Ground Profile along the x-axis included into the FDTD method (b) Horizontal electric field from the current dipole location along an abrupt profile change for different oscillating frequencies (dashed: Homogeneous, black empty circle: 1MHz, gray filled circles: 5MHz , black filled circles: 10MHz)

As can be seen from Figure 55(b), the horizontal component of the radiated electric field increases its magnitude before the terrain irregularity is reached. This effect is caused by the wave reflections due to the presence of the ground step. In Figure 55(b) the electric field magnitude for the homogeneous case is also shown in dashed line. As it can be seen for the 1MHz case, the magnitude of the electric field changes when compared to the homogenous case value, then it increases its magnitude closer to the ground step and once it is surpassed, the magnitude of the electric field component returns to the homogeneous case value. A different behavior is observed for the frequencies of 5MHz and 10MHz. As it can be seen, the first section of the path differs from the homogeneous case due to the reflected wave magnitude and once the step ground is overcome, the electric field magnitude presents different maxima and minima along the path. This is mainly due to the interaction between the wave and the obstacle at the frequencies under analysis.

5 Lightning Return-Stroke Modeling

The lightning return-stroke modeling is one of the most important factors in determining the induced voltages on overhead lines because there is a strong dependence between the radiated fields and the current propagation features along the lightning return-stroke channel. For lightning radiated field analysis, several lightning return stroke models [58] have been proposed in order to reproduce the typical behavior of measured lightning electromagnetic fields [6]. Depending on the mathematical formulation and the physical assumptions made for each lightning return stroke models, the current distribution along the channel is predicted or imposed, taking the current waveform at the base of the channel as an input [59].

Depending on the approach used for representing the current distribution along channel, these models are classified as: Engineering Models, Electromagnetic Models (HEM) and Circuital Models [6][8]. Following sections will present different lightning return-stroke models that have been proposed in literature.

5.1 Engineering Models

The engineering models assume the current propagation along the channel as a function of a known current waveform at its base and at a given constant propagation velocity. The current propagates either without any distortion, or considering very simple attenuation functions. The most common expressions that are used in order to include the amplitude attenuation along the channel are: linear-current decaying (Modified Transmission Line Model with Linear decay, MTLL) and exponential-current decaying (Modified Transmission Line Model with Exponential decay, MTLE) [61][62][63]. The expressions for the amplitude variation are shown in Table 1 [63].

Longitudinal Current Expression		
TL	$i\left(0, t-\frac{z'}{v}\right)$	Being v the current velocity of propagation.
MTLL	$\left[1-\frac{z'}{H}\right] i\left(0, t-\frac{z'}{v}\right)$	Being H the length of the lightning channel.
MTLE	$e^{-(z'/\lambda)} i\left(0, t-\frac{z'}{v}\right)$	Being λ the current-decay height constant.

Table 1 Longitudinal Current Expressions depending on the return-stroke model

From these models, it is possible to represent the lightning channel as a set of current sources each one of them having a current waveform given by the expressions presented before. Figure 56 shows the current distribution when a MTLE model with a current-decay height constant λ=2km and velocity of propagation $v = c/2$ is used.

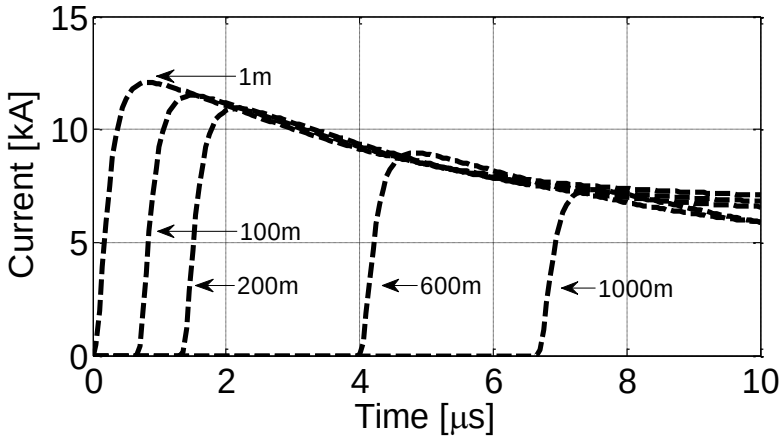

Figure 56 Current Propagation by means of the MTLE with λ=2000, v=c/2

The mathematical expression used for the base-current corresponds to a superposition of exponential Heidler´s functions, which is a typical waveform used for subsequent return-strokes:

$$I(0,t) = \frac{I_1}{\eta_1}\left(\frac{t}{\tau_{11}}\right)^n \left[\frac{e^{-\frac{t}{\tau_{12}}}}{1+\left(\frac{t}{\tau_{11}}\right)^n}\right] + \frac{I_2}{\eta_2}\left(\frac{t}{\tau_{21}}\right)^n \left[\frac{e^{-\frac{t}{\tau_{22}}}}{1+\left(\frac{t}{\tau_{21}}\right)^n}\right] \quad (5.1)$$

Where η_1 and η_2 can be calculated using the expression:

$$\eta_m = e^{-\left(\frac{\tau_{m1}}{\tau_{m2}}\right)\left(n\frac{\tau_{m2}}{\tau_{m1}}\right)^{1/n}} \quad (5.2)$$

Where the value of the parameters for the channel base current were assumed to be: $I_1 = 10.7\ kA, I_2 = 6.5\ kA,\ n = 2, \tau_{11} =\ 0.25\ \mu s, \tau_{12} =\ 2.5\ \mu s,\ \tau_{21} = 2\mu s, \tau_{22} = 280\ \mu s$.

5.2 Electromagnetic Models

As in natural lightning, a charge transfer take place between the ground to the cloud and lightning return-stroke models must approach to represent this process. A vertical thin wire transporting current from ground to cloud establish an adequate scenario to achieve this [59]. The thin-wire model corresponds to the simplest electromagnetic model for a return-stroke in which the current distribution along the channel results from the solution of the Maxwell´s equations along the vertical thin wire, when a current waveform is imposed at the channel base. The solution of the Maxwell's equations for can be found by several methods.

Two numerical techniques were used in order to solve the current distribution for a vertical thin-wire. One of the techniques addresses the problem in the frequency-domain and the other one in the time-domain.

One of the most popular solutions consists in dividing the channel into several segments and the resulting integral equation for the scattered field is solved by the Method of moments (MoM) [66]. The current distribution along the channel is obtained solving the integral equation for each segment in the frequency-domain and then by applying the inverse Fourier transform, the current distribution along the channel can be obtained in the time-domain [64].

In order to solve the integral equation a computer program called the Numerical Electromagnetics Code (NEC-4) was used [67]; this well-known program allows evaluating several setups for predicting conducted and propagated electromagnetic fields. For the time-domain solution, the full-wave equations were solved by means of the Finite Difference Time Domain (FDTD) algorithm implemented in this thesis. The return-stroke model can be included by using the Noda and Yokoyama thin-wire representation as it was discussed in section 3.7.

Figure 57 shows a comparison of the current distribution along the channel when two different methods for solving the electromagnetic equations are used.

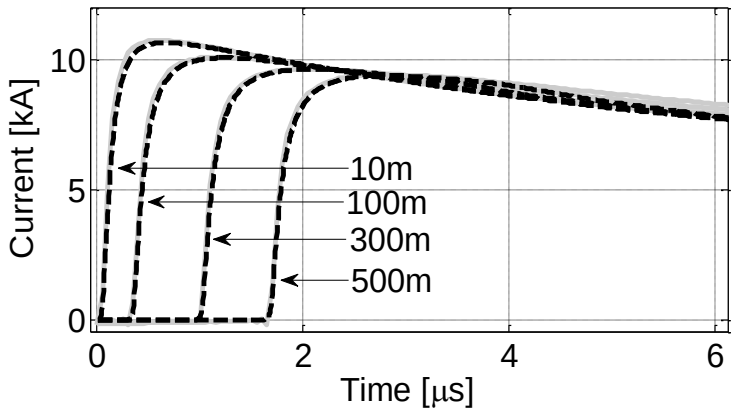

Figure 57 Longitudinal Current Propagation for a Vertical Thin-Wire with radius 0.3m (solid line: NEC-4, dashed: FDTD)

As it can be seen from Figure 57 there is a good agreement between the two formulations for the thin-wire model and as it is discussed in [59], the attenuation of the current along the lightning channel describes the current distortion as it occurs in the natural return stroke.

Despite of the lightning return-stroke model using a perfectly conducting thin-wire reproduces the current distortion along the channel, the upwards velocity of propagation cannot be controlled and it is near the speed of light.

5.3 Lightning Channel as a Loaded Thin-wire

In order to control the propagation velocity, distributed lumped elements that are able to storage energy are included long the channel. By means of this approach the current propagation can be delayed in time, achieving slower apparent phase-velocities [6][64].

In this case, a lightning channel having a radius of 0.23 m was placed in an air working volume of $60 \times 60 \times 2300$ m^3 divided into $1 \times 1 \times 10$ m^3 cells, above a perfectly conducting ground. The channel was loaded with a series inductance L = 2μH/m and excited by a 10 m lumped current source. Absorbing CPML boundaries were placed at the top and all sides of the working volume. Figure 58 shows the calculated currents at different heights contrasted with those presented in [6].

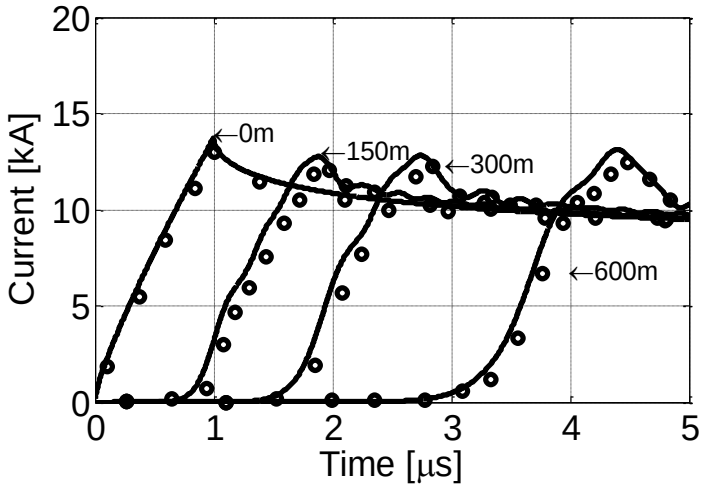

Figure 58 Current Distribution along a Thin-Wire inductance-loaded (Solid line: FDTD implementation, circles line: Results presented in [6]).

As it can be seen from Figure 58, the calculated current distribution along the channel exhibits distortion as in the perfectly conducting thin-wire model, but in addition the velocity of propagation is controlled about 0.6 times the speed of light.

The thin wire model can be also loaded with a series resistive-inductive per unit length in order to reproduce not only the phase-velocity of the propagating current as it was shown with the inductive load, but also to obtain more attenuation whereas the current propagates.

In order to analyze the effect of loading the thin-wire by RL-series load, a simulation in NEC-4 by means of a wire loaded by lumped RL series branches and a thin-wire implementation into the FDTD method was performed. The thin-wire had 2000m in length and 0.23m in radius. In order to obtain a current propagation velocity of near one-third of the speed of light a series resistive-inductive (RL) load value of 1Ω/m and 2μH/m was used. The current waveform used was the one proposed by Chen as illustrated in [10].

The results of the current distribution along the channel using the two methods described above are shown in Figure 59 where both approaches are in good agreement with the current wave propagation prediction.

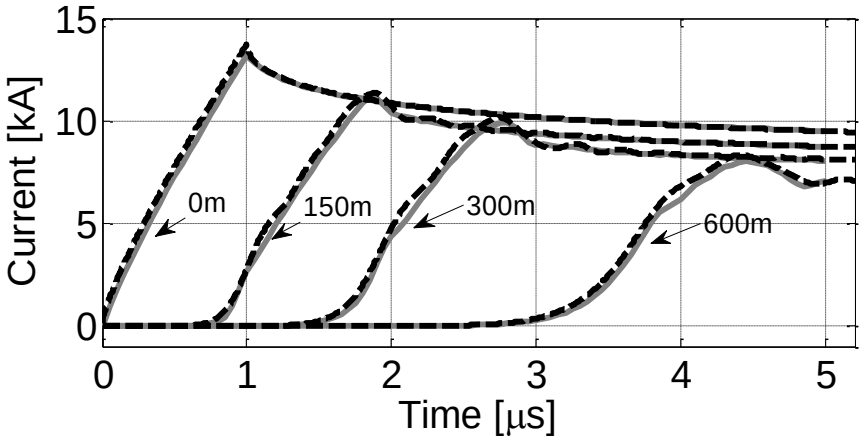

Figure 59 Current Propagation along the Lightning Channel (solid line: NEC-4, dashed: FDTD)

As can be seen from Figure 59, the lightning channel model represented by a loaded thin-wire allows the control of the phase velocity of the current wave and produces distortion on its waveform.

As a result, obtaining the current distribution by means of an electromagnetic models instead of impose it by means of an engineering model, differences can be seen among current waveforms along the channel. In Figure 60 there is a comparison between the current distribution along the return-stroke for the MLTE model and the RL loaded thin wire. As can be seen, despite the phase-velocity for both models is about a half of the speed of light, there is more current-dispersion along the channel when the RL loaded thin-wire model is considered.

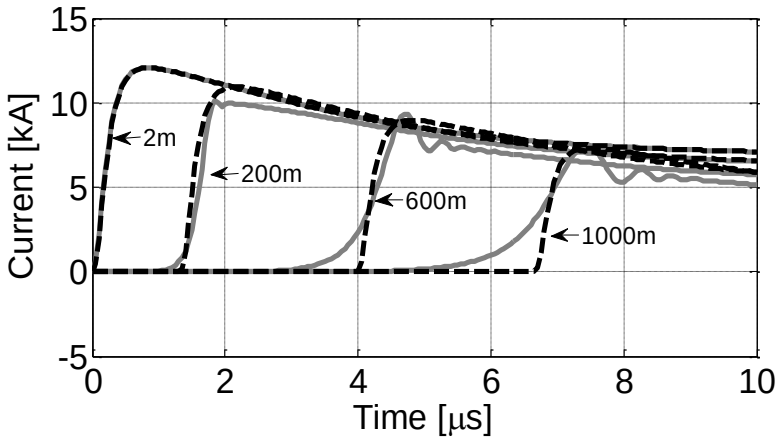

Figure 60 Comparison between the MLTE and RL loaded thin-wire for return stroke models (solid: base channel current, solid grayed: RL-loaded thin-wire, dashed: MTLE λ=2km)

Besides, depending on the return stroke model different current distribution waveforms along the lightning channel are found. The selection of the lightning return-stroke model can be done depending on the case under study. Although the MLTE and the series RL-loaded thin-wire model present different current distributions, both models are able to reproduce similar lightning radiated electric field characteristics of natural and rocket-triggered lightning.

6 Propagation Path Effects on Lightning Radiated Fields

This section addresses the effects of the presence of different ground structures on the lightning-radiated fields. As it was presented before for a current dipole, the characteristics of the propagation path can affect the electric radiated fields in a considerable magnitude. These effects were analyzed not only in the far-field region but also it was demonstrated to have an important contribution in the near field region.

As it was shown before, the lightning return-stroke channel can be modeled by means of several approaches. All of those models reproduce the most important characteristics of the natural return-stroke current distribution and any could be used for calculating lightning radiated fields. As it was discussed in section 5, the characteristics of the current propagation in a natural return-stroke can be reproduced when electromagnetic models are used.

Based on this approach, the results discussed before for a vertical-current dipole above different ground structures in the frequency domain can be extended, using the superposition theorem, by means of a set of vertical-current dipoles along the channel and the evaluation of its contribution at the observation point. Once the frequency response at an evaluation point has been calculated including all the sources that represent the lightning channel, the inverse Fourier transform can be used in order to determine the time-domain waveform for a determined channel-base current.

6.1 Perfectly Conducting Ground

The perfectly conducting ground effect can be taken into account by the theoretical formulation based on the image theory method. The perfectly conducting ground can be seen as a reference condition for cases where the lossy, inhomogeneous and irregular ground conditions are present.

A comparison between the theoretical predictions and those results calculated by a full-wave solution for the near field region were carried out in order to validate the FDTD method for calculating lightning radiated fields from return-stroke modeled by means of a RL-loaded thin-wire. Using the FDTD implementation with non-regular meshing, a more detailed mesh was specified near the lightning channel location whereas a coarser domain was assumed for the rest of the region.

The minimum spacing size was assumed to be 5m. The maximum spacing was about 50m for the x and y direction and 7.5m for the z direction. The z-direction domain was meshed as regular up to 150m above the ground interface. The non-regular mesh was calculated by means of the proposed parabolic meshing using an attenuation factor α=0.1 for soft spacing change along the z-axis and α=0.5 and for the x and y axis. Figure 61 presents the mesh distribution for the simulation scenario. The lightning channel modeled as a loaded thin-wire was placed at the coordinate

X_0=1500m, Y_0=1500m. It was simulated with 1500m in height and 0.3m in radius. In order to control the propagation velocity of the current along the channel to be a half of the speed of light, it was loaded with a RL series load with 1Ω/m and 3μH/m in resistance and inductance values respectively.

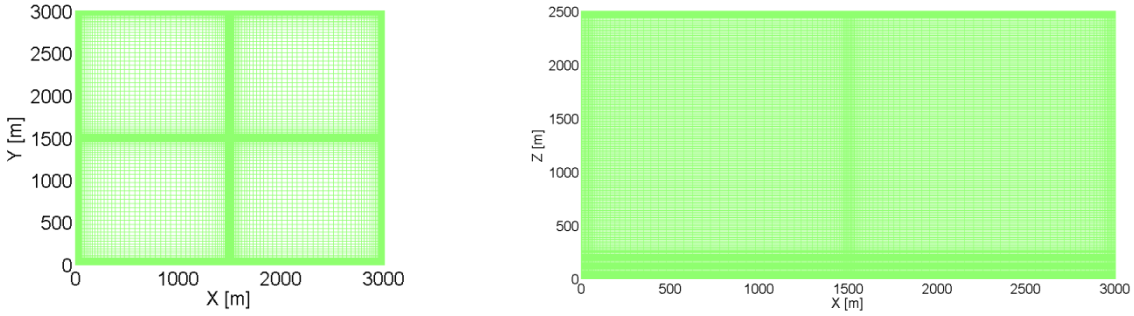

Figure 61 FDTD Non-regular mesh distribution (a) Top View (Plane XY) (b) Side View (Plane XZ)

A typical waveform used for representing subsequent return-strokes is assumed at the base of the channel given by:

$$I(0,t) = \frac{I_1}{\eta_1}\left(\frac{t}{\tau_{11}}\right)^n \left[\frac{e^{-\frac{t}{\tau_{12}}}}{1+\left(\frac{t}{\tau_{11}}\right)^n}\right] + \frac{I_2}{\eta_2}\left(\frac{t}{\tau_{21}}\right)^n \left[\frac{e^{-\frac{t}{\tau_{22}}}}{1+\left(\frac{t}{\tau_{21}}\right)^n}\right] \tag{6.1}$$

Where η_1 and η_2 can be calculated using the expression:

$$\eta_m = e^{-\left(\frac{\tau_{m1}}{\tau_{m2}}\right)\left(n\frac{\tau_{m2}}{\tau_{m1}}\right)^{1/n}} \tag{6.2}$$

The parameters that were used for the simulations were assumed to be: $I_1 = 10.7\ kA,\quad I_2 = 6.5\ kA, n = 2, \tau_{11} = 0.25\ \mu s, \tau_{12} = 2.5\ \mu s,\ \tau_{21} = 2\mu s, \tau_{22} = 280\ \mu s.$

Figure 62 presents the current distribution along the lightning channel for both different approaches, one of them is based on the antenna theory model with fixed inductive load and when the RL loaded thin-wire model is considered into a non-regular mesh FDTD simulation. As it can be observed, the current distributions obtained from the FDTD method agree well with those obtained from the MoM solution using the NEC-4 code.

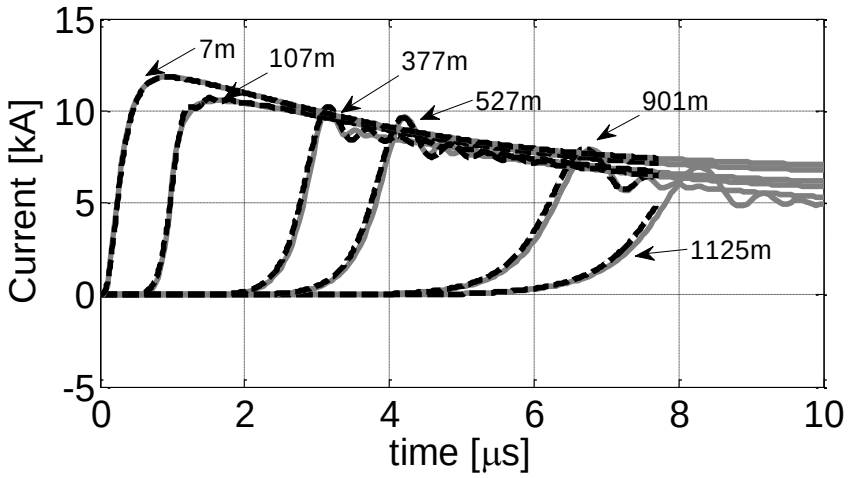

Figure 62 Current Distribution along the Lightning Channel RL loaded Return-Stroke model (solid grayed: NEC-4, dashed line: FDTD-Thin Wire RL loaded)

In Figure 63 there is a comparison for the horizontal electric field calculation by means of the FDTD in the near field region and those results using the theoretical calculation by means of the image theory. Two different distances from the lightning channel base to the observation point were analyzed. **Range I:** distances closer than 200m and **Range II:** distances longer than 500m.

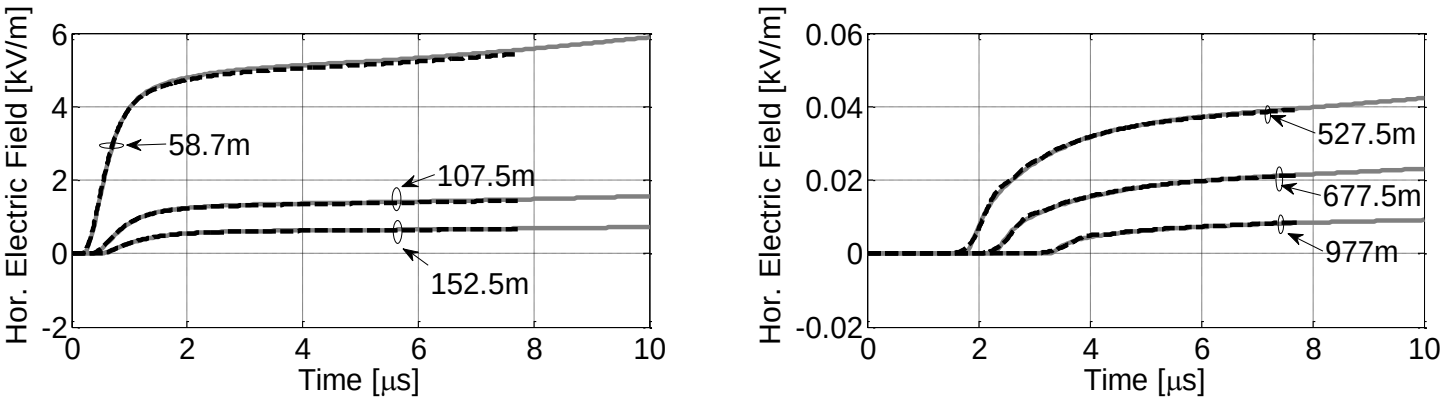

Figure 63 Lightning Radiated Fields above Perfectly Conducting Ground, Horizontal Electric Field (Solid Line: Theoretical, Dashed Line: FDTD) (a) Hor. Electric Field Range I (closer distances than 200m to the Channel Base) (b) Hor. Electric Field Range II (longer distances than 500m to the Channel Base)

As can be seen from Figure 63 the FDTD results are in a good agreement with those using the theoretical calculation. The maximum error between both results is about 2%. This is a tolerable

error taking into account the considerable decreasing on the total simulation time and the maximum space volume when a non-regular mesh is used.

6.2 Homogeneous Lossy Ground

The presence of lossy ground has been demonstrated to be a very important factor in lighting radiated field waveforms, especially for the horizontal electric field component within the near field region.

Norton´s approximation has been tested for lightning radiated field calculations in multiple scenarios of distance and ground conductivities, concluding about its validity in the near-field only when relatively good ground conductivities values are present. Even for some cases, the Norton´s approximation provides reasonable results for ground resistivity values lower than 1000Ωm and for distances within 50m up to 200m from the channel base. It has been also showed that the Norton´s approach leads to better results in the case of subsequent return strokes.

In order to validate the lightning radiated fields. Figure 64 presents a comparison between the rigorous solution of the Sommerfeld´s equations taken from [20] and the Norton´s approach implemented in this thesis for the horizontal electric field component above a homogeneous ground with a resistivity ρ=1000Ωm at 200m from the lightning channel. The return-stroke current corresponds to a typical subsequent stroke and the same parameters presented in [15] were used.

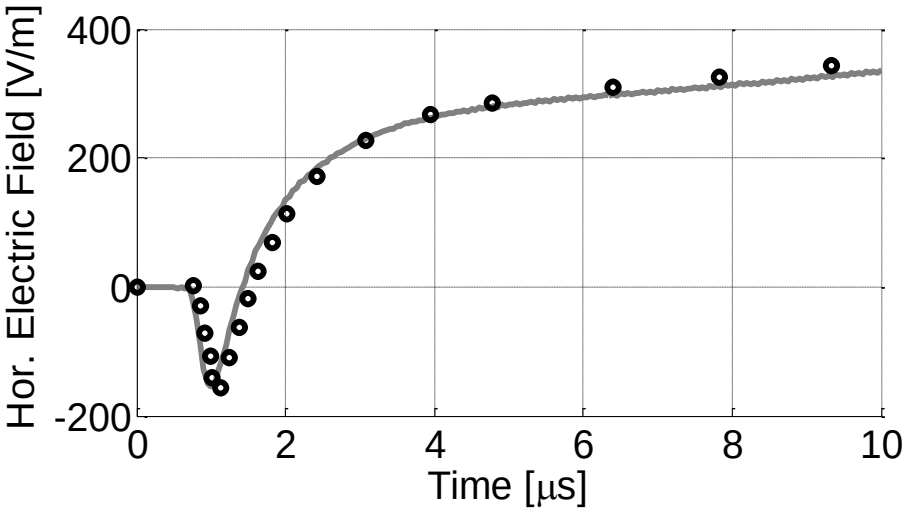

Figure 64 Horizontal Electric field at 10m height above a lossy ground of resistivity 1000Ωm at a distance of 200m from the stroke modeled by MLTE (dashed: Norton Approach, circles: Sommerfeld's taken from [20])

As can be seen from Figure 64 Norton´s approach is in well agree with the rigorous solution of the Sommerfeld´s integrals as most of the principal characteristics of the radiated waveform are

reproduced. The negative excursion that is present in the horizontal electric field component has been shown to be highly dependent on the resistivity of the ground and the vertical electric field component.

In order to analyze the effect of the ground resistivity on the lightning radiated field magnitudes and waveforms, a set of simulations with different ground conductivities were performed by using the Norton´s approach. In Figure 65 a comparison for the electric radiated field components for 10Ωm, 100Ωm and 1000Ωm resistivity values is presented. The return stroke was modeled by a straight wire loaded with a lumped RL load of 1Ω/m in resistance and 3μH/m in inductance respectively. The current distribution along the channel was obtained by means of the antenna theory approach by using the NEC-4 code as it was discussed in section 5.3. The electric fields were calculated at 10m above the ground.

As it can be seen from Figure 65(a), the vertical component of the radiated electric field is less affected by the resistivity ground values than the horizontal one. Figure 65(b) and Figure 65(c) shows that the waveform shape of the horizontal component is highly affected by the resistivity changes. The negative excursion is the most evident distortion especially for distances greater than 500m from the lightning channel base. However, for all the cases radiated electric fields tends to the same maximum value.

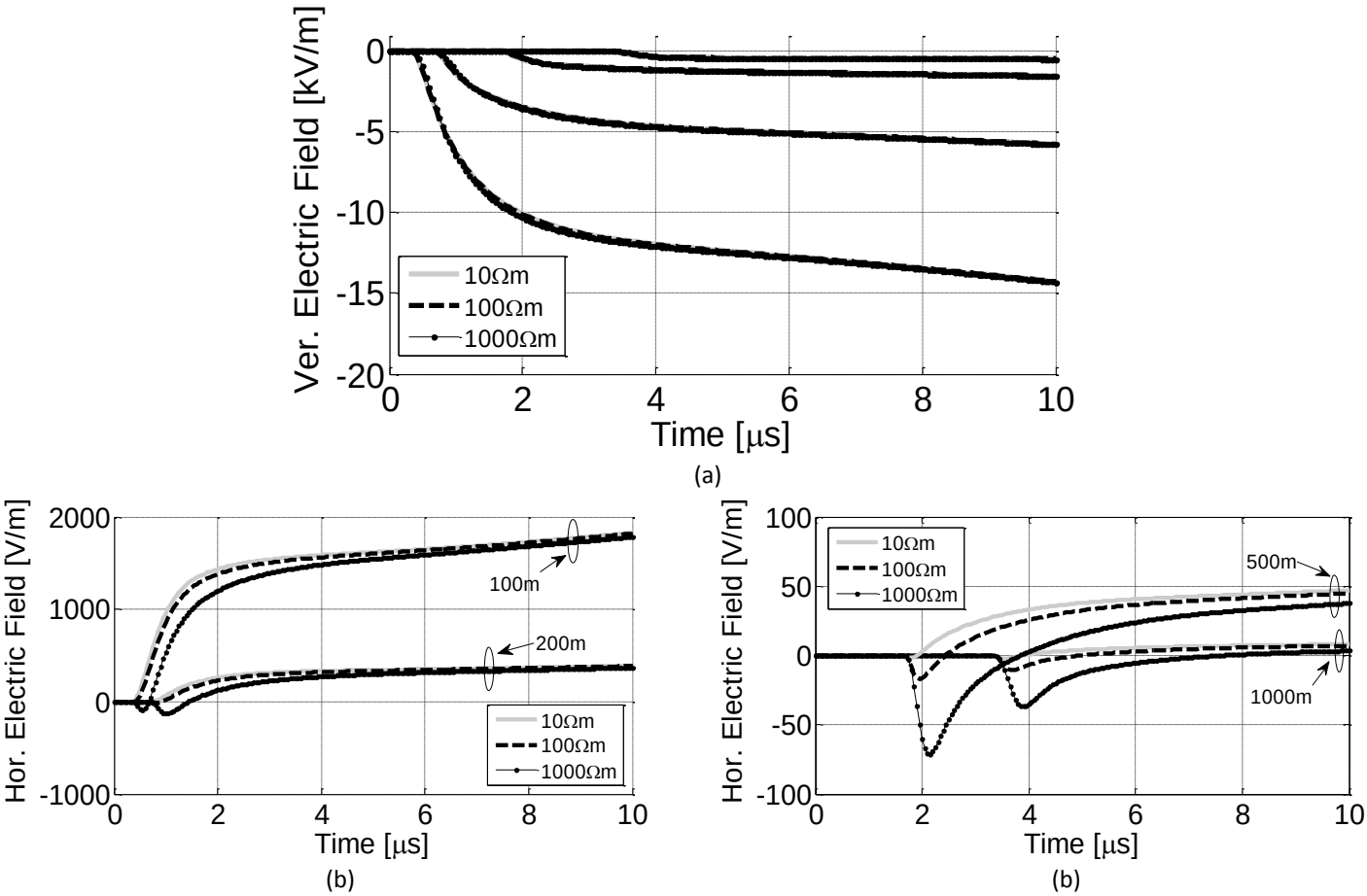

Figure 65 Radiated Electric Fields above different Ground Resistivity values (a) Vertical Electric Field (b) Horizontal Electric Field for distances closer than 200m (c) Horizontal Electric Field for distances further than 500m

As it was presented in section 5, the current distribution along the channel depends on the lightning channel model. In order to verify the influence on the lightning radiated fields due to the current distribution along the channel, a comparison between the horizontal and vertical component due to a MLTE model and RL-Thin-wire was performed. For the lightning channel model represented by the loaded vertical wire the current distribution along the channel was calculated by the NEC-4, however the radiated fields are in both cases calculated by the Norton´s approach. In Figure 66 there is a comparison between the current distribution along the channel and their radiated fields above lossy ground with 1000Ωm in resistivity and $10\varepsilon_0$ in permittivity when two different lightning return-stroke models are used, the MLTE model with λ=2km and the RL loaded thin wire with 1Ω/m in resistance and 3μH/m in inductance.

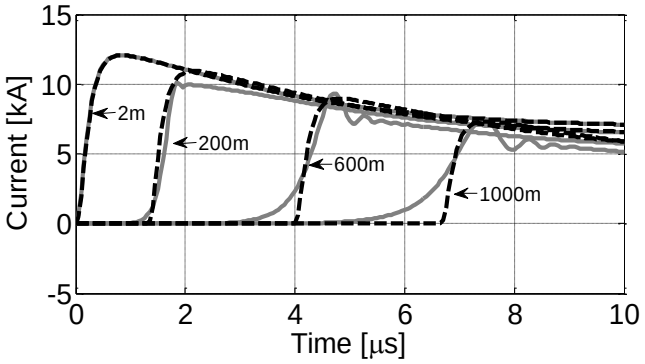

(a)

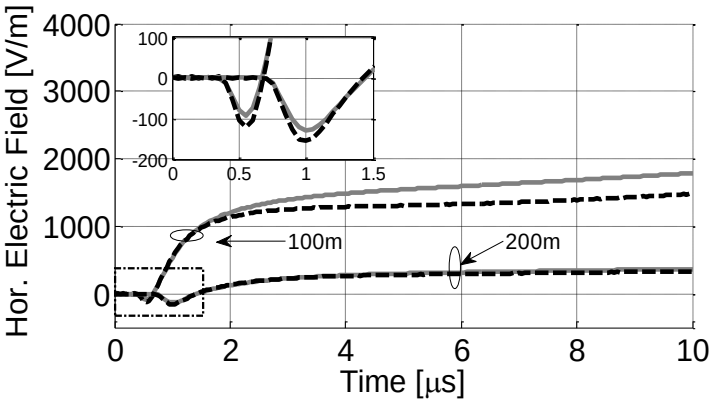

(b)

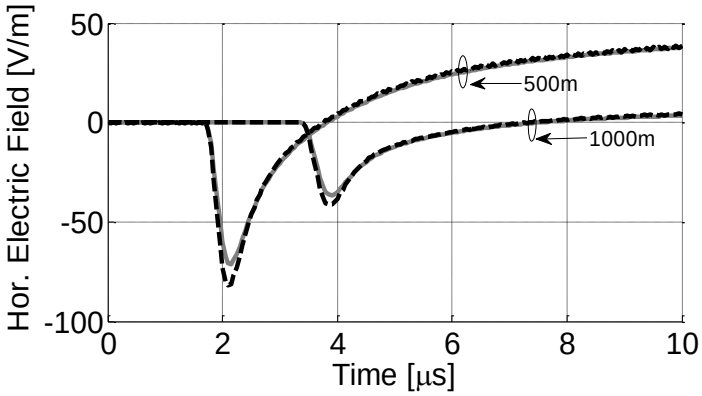

(b)

Figure 66 Horizontal Electric Field Component with different lightning return-stroke model (solid: RL Thin-Wire, dashed: MLTE) (a) Current distribution along the Channel (b) Electric Field Component at distances closer than 200m (c) Electric Field Component at distances further than 500m

As can be seen from the comparison presented in Figure 66, the waveforms of the radiated fields are similar to each other but it can be also found some important differences at closer distances from the lightning channel base. For further distances from the lightning channel base the

negative excursion is the most affected characteristic of the waveform by the current distribution [69].

As it has been shown by several authors, Norton´s approach can be applied for some near field situations of lightning radiated fields. However, this approach is not valid for all the distance ranges and its intrinsic assumption of cylindrical problem space symmetry is normally invalid for general cases of lightning induced voltages. The FDTD method can be used for those situations where the Norton's approach assumptions are not valid or more general simulation scenarios must be simulated.

In [70] a FDTD simulation with a fine mesh was performed in order to validate the popular CR formula for the horizontal radiated field above lossy ground [21][22]. Figure 67 presents a comparison between the results presented in [70] by a very fine-mesh FDTD and the Norton´s approach implemented in this thesis. The comparison is presented for the near field range at 100m and 1000m from the lightning channel base.

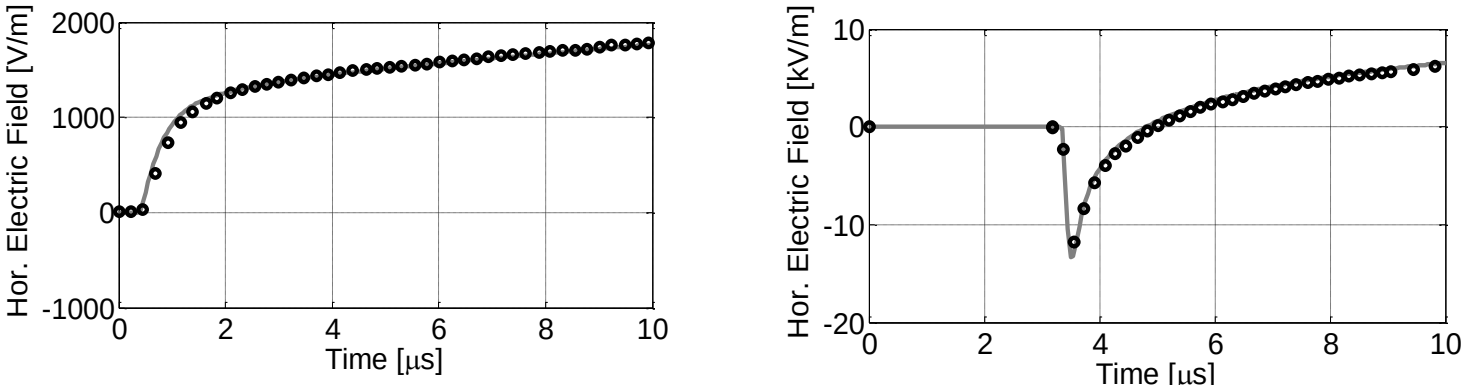

Figure 67 Horizontal Electric field at 10m height above a lossy ground of resistivity 100Ωm at two-different distances from the channel modeled by RL Loaded Thin-Wire (a) at distance of 100m (b) at distance of 1km (dashed: Norton Approach, circles: FDTD taken from [70])

In order to validate the Norton´s approach for calculating lightning radiated fields above a relative high ground resistivity (ρ=1000Ωm), a simulation set-up using a full-wave solution by means of the FDTD method with non-regular mesh was performed.

The lightning channel was modeled by means of the MTLE model assuming λ=2km and a velocity of propagation of c/2 and 1500m in height. The ground conductivity was assumed to be 1000Ωm along with a Non-regular mesh with a maximum space discretization of 17.5m in the coarser domain. In the region of interest a delta space of 5m was used. In Z-directed coordinates regular spacing was considered and the lightning channel was placed in the center of the XY plane. Radiated fields were calculated along the x-axis in order to coincide with those radial electric fields calculated from the Norton´s approach. Figure 68 shows the non-regular mesh used for the simulation.

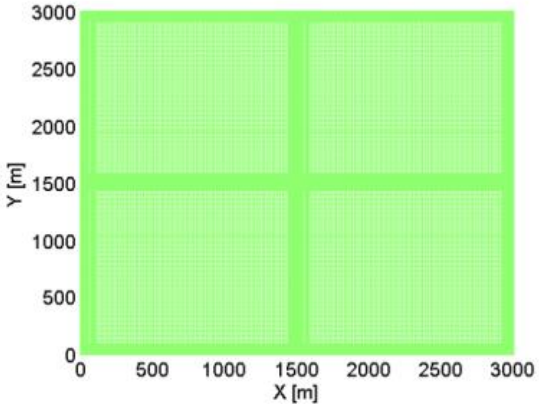

Figure 68 Top View of the non-regular FDTD Meshing of the Problem Space

The total volume was 3000x3000x2500m^3 which corresponds to 209x209x501 non-regular cells in the computational domain. Figure 69 shows the radiated horizontal electric field component.

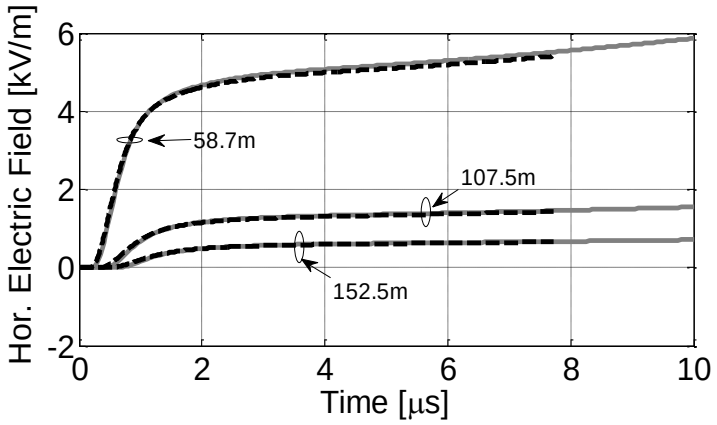

(a)

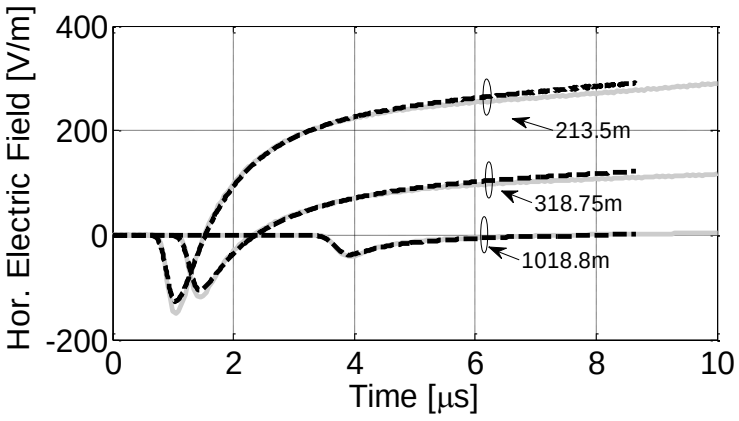

(b)

Figure 69 Horizontal Electric field at 10m height above a lossy ground of resistivity 100Ωm (dashed: FDTD non-regular Mesh, Solid: Norton´s Approach) (a) Distances closer than 200m (b) Distances further than 200m

By several simulations, it was evident that in the FDTD method the horizontal electric field component is highly affected by the ground conductivity, mainly in the negative excursion portion of the waveform. However, for closer distances to the lightning channel base, the Norton´s approach and the FDTD are a very good agreement and for further distances the error is less than 2%.

6.3 Non-homogeneous Ground

As it was presented before, a lossy ground presence can modify the waveforms and peak values of the lighting radiated fields. It has been shown that radiated electric field waveforms are dependent on the distance and particularly, the horizontal electric field component can present changes of polarity for some close distance ranges. This section shows other effects that can be present on the radiated field when non-homogeneities are present along the propagation path.

6.3.1 Mixed-Path ground

In order to analyze the effects of a mixed path on the lightning electromagnetic field, first the Norton's and Wait's approaches are compared. The path parameters were set to ρ_1=0.5Ωm with relative permittivity ε_{r1}=81 for the first section, and ρ_2=500Ωm with relative permittivity ε_{r2}=15 for the second section. The boundary for the first section was located at X_1=750m from the lightning channel base. Figure 70(a) depicts the simulation problem space. Horizontal and vertical electric field components were calculated at 10m in height above the ground.

The lightning return stroke was modeled as a RL loaded thin wire with 3km in length and it was represented as a loaded vertical thin-wire in the NEC-4 code, once the current distribution along the channel was available, the calculation of the radiated fields was performed by using the Wait´s formula. The RL series parameters were set to be 1Ω/m and 3μH/m in lumped resistance and inductance respectively in order to obtain a velocity of propagation about one half of the speed of light. There were used 1500 segments with 2m in height to represent the lightning channel.

Figure 70(b) and (c) presents the comparison between the lightning radiated fields along the two section mixed path and the homogeneous case assuming a lossy ground with constant resistivity value of ρ_1=0.5Ωm and relative permittivity ε_{r1}=81. As can be seen from Figure 70(c) the vertical electric field remains practically unmodified by the mixed path presence, however the horizontal electric field component shown in Figure 70(a) presents the same waveform characteristics as in the high resistivity homogeneous ground analyzed in the previous section.

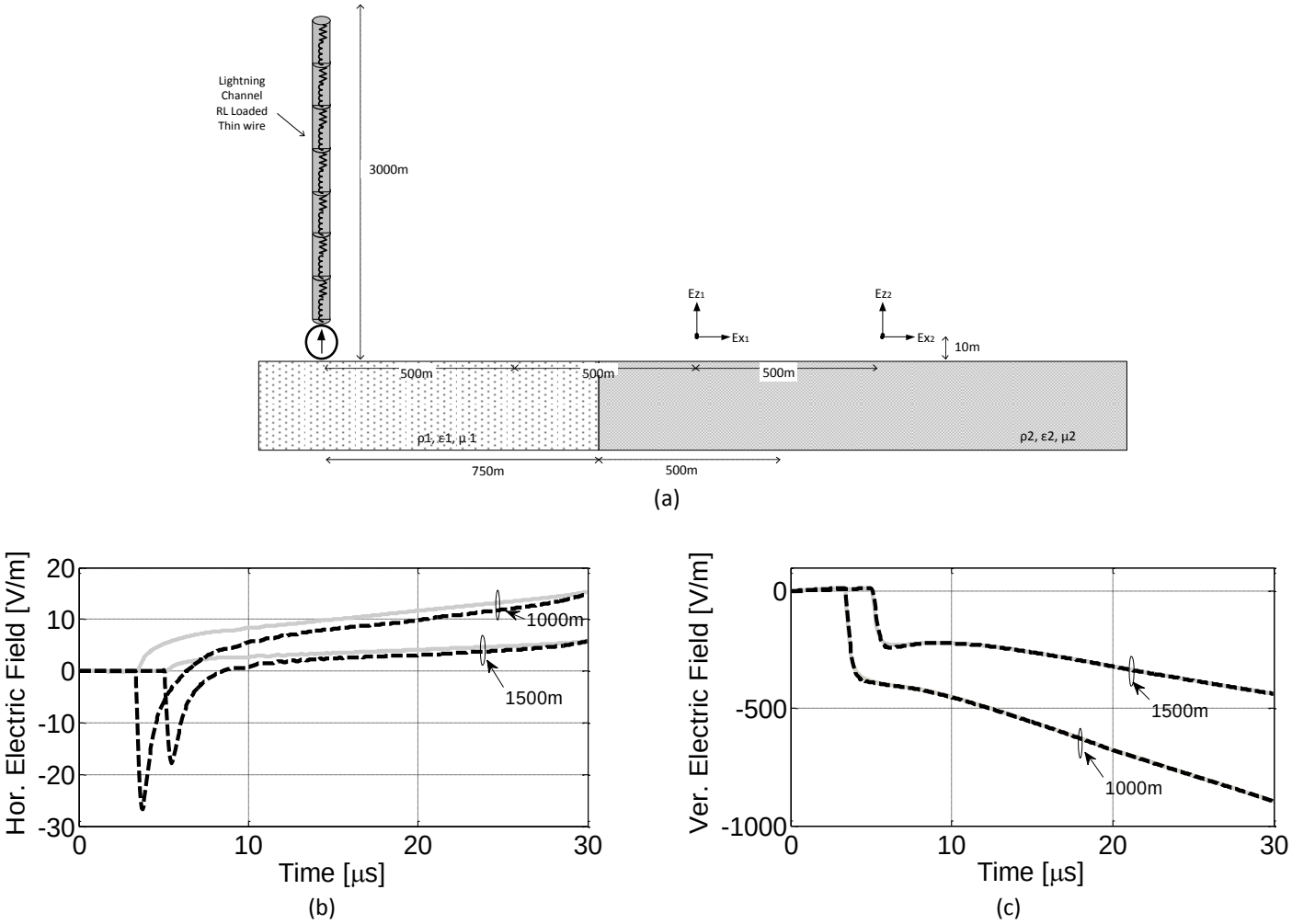

Figure 70 two-section mixed-path (solid: Homogeneous Case, dashed: Mixed-path condition) (a) Relevant geometry of the Mixed-path of two section under analysis (b) Horizontal Electric field (c) Vertical Electric field

The recovery effect mentioned before takes place when the traveling wave goes from a low conducting ground to a high conductivity one. In order to validate the recovery effect on the lightning radiated fields a third section was placed at 500m after the boundary X_1 with the same ground parameters as those assumed before for the first two sections of the mixed-path. Figure 71(a) shows the simulation geometry set-up.

As can be seen from Figure 71(c) the vertical electric field component also remains with no appreciable modifications of its waveform when it is compared with the homogeneous case. The horizontal component presents a negative excursion when it is calculated over the second path which is characterized by a high resistivity ground value. However, when it is calculated above the low resistivity value the horizontal electric field component “recovers” the magnitude as in the homogeneous case. The same effect was validated for the vertical radiating dipole in chapter 5.

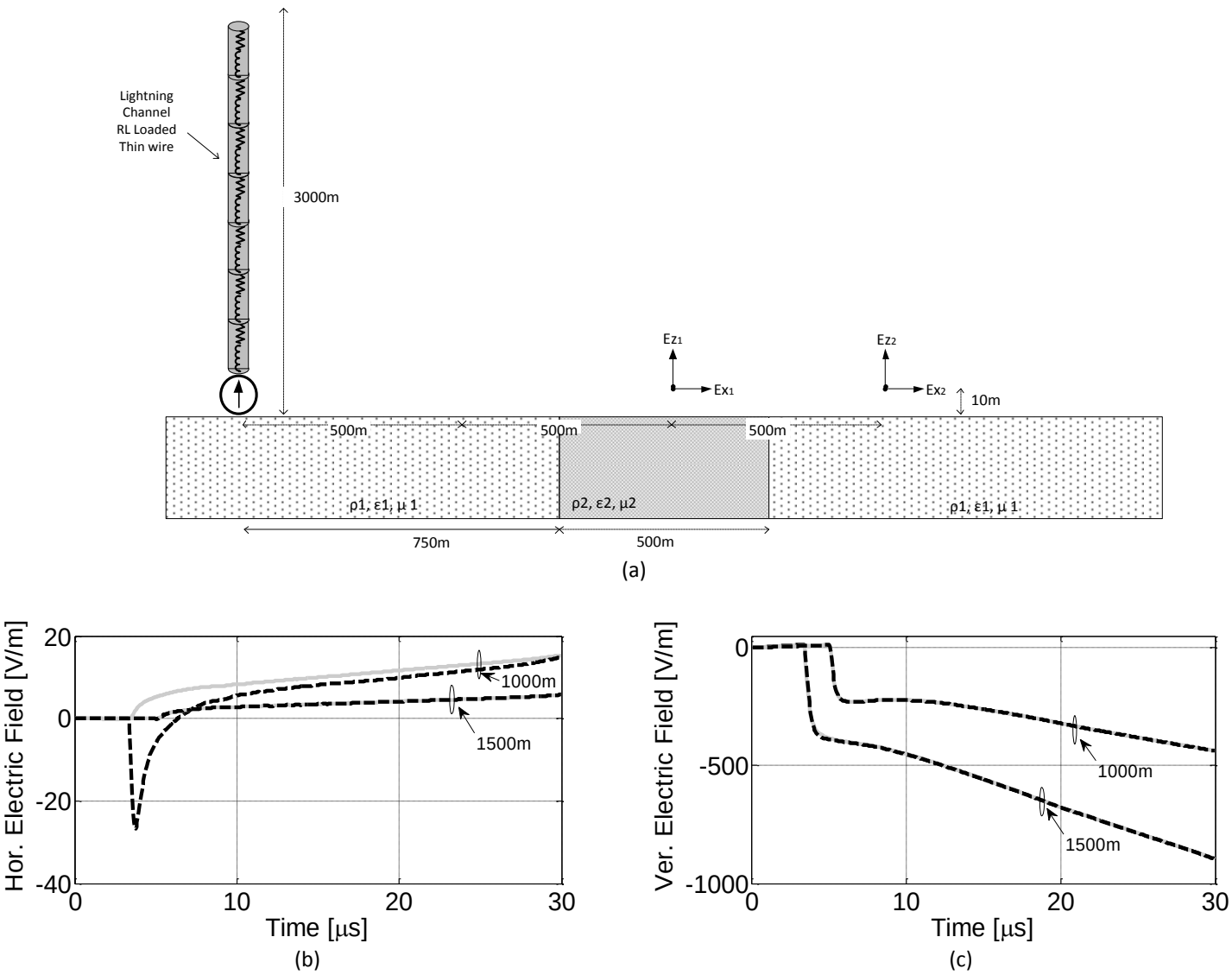

Figure 71 Mixed-Path of three sections for lightning radiated fields (solid: Homogeneous Case, dashed: Mixed-path condition) (a) Relevant geometry of the Mixed-path of three sections under analysis (b) Horizontal Electric field (c) Vertical Electric field

As it was discussed in previous sections, the Wait´s approach for the propagation along a mixed-path sections is based on several considerations that in general cannot be assumed on several scenarios. The FDTD method allows simulating multi mixed-path sections without specific assumptions about the section lengths and geometric symmetry. In order to compare the results obtained with the Wait approach with those obtained with the FDTD method, a simulation set-up of a mixed-path was performed and its results were compared with those calculated by means of the Wait´s formulas.

The Mixed Path was located at 205m from the lightning channel base and electric field components have been calculated along the propagation path at 10m above the ground. Figure 72(a) depicts the simulation scenario. The lightning channel was simulated in the FDTD by means

of a MTLE model with a velocity of propagation set to be one half of the speed of light and attenuation factor λ=2km. The lightning channel length was assumed to be 1.5km in length.

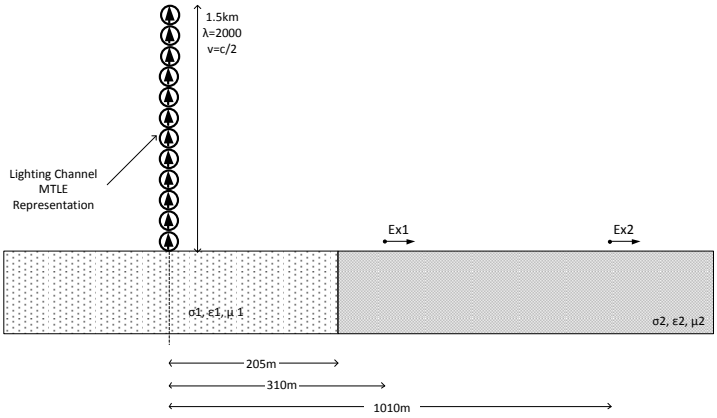

(a)

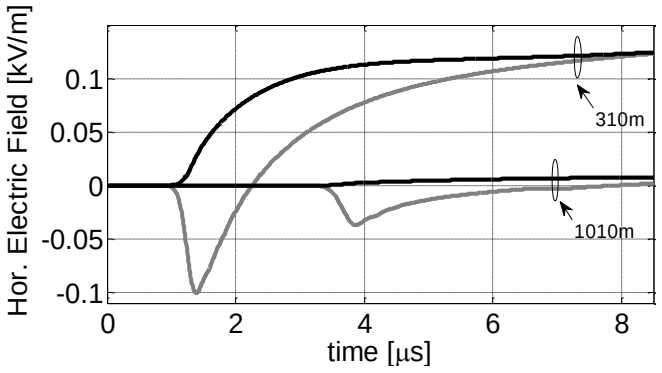

(b)

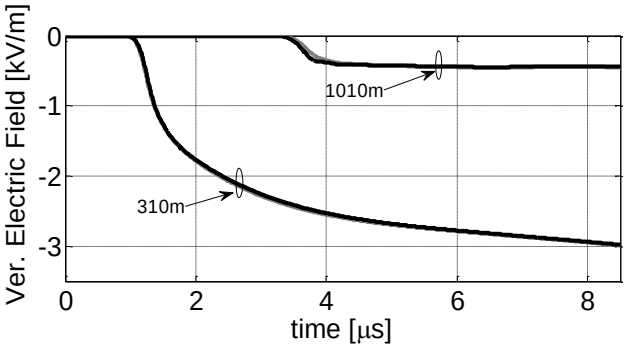

(c)

Figure 72 Lightning Radiated Fields Mixed-Path of Two-Section calculated by the FDTD method. Case 1 (Gray line): 10Ωm / 1000Ωm, Case 2 (Black line): 1000Ωm / 10Ωm (a) Simulation Set-Up (b) Horizontal Electric Field (c) Vertical Electric Field

As it can be seen from Figure 72(b) and Figure 72(c), the change of ground conductivity affects mainly the horizontal electric field component. The vertical electric field component can be assumed as undisturbed by the ground conductivity changes; this result is in agreement with the analysis presented in section 6.2 where different ground conductivity and distances from the channel base were considered. As in Figure 70, similar waveforms for the horizontal electric field can be seen in both simulations.

In order to validate the effects of the mixed-path on the lightning radiated fields and the validity of the Wait´s formulas within the near field range, the same simulation set-up proposed in Figure 72(a) was used for the calculation of the radiated fields by using the Wait´s formulas and the results are compared with those presented in Figure 72(b) and Figure 72(c) by means of the FDTD.

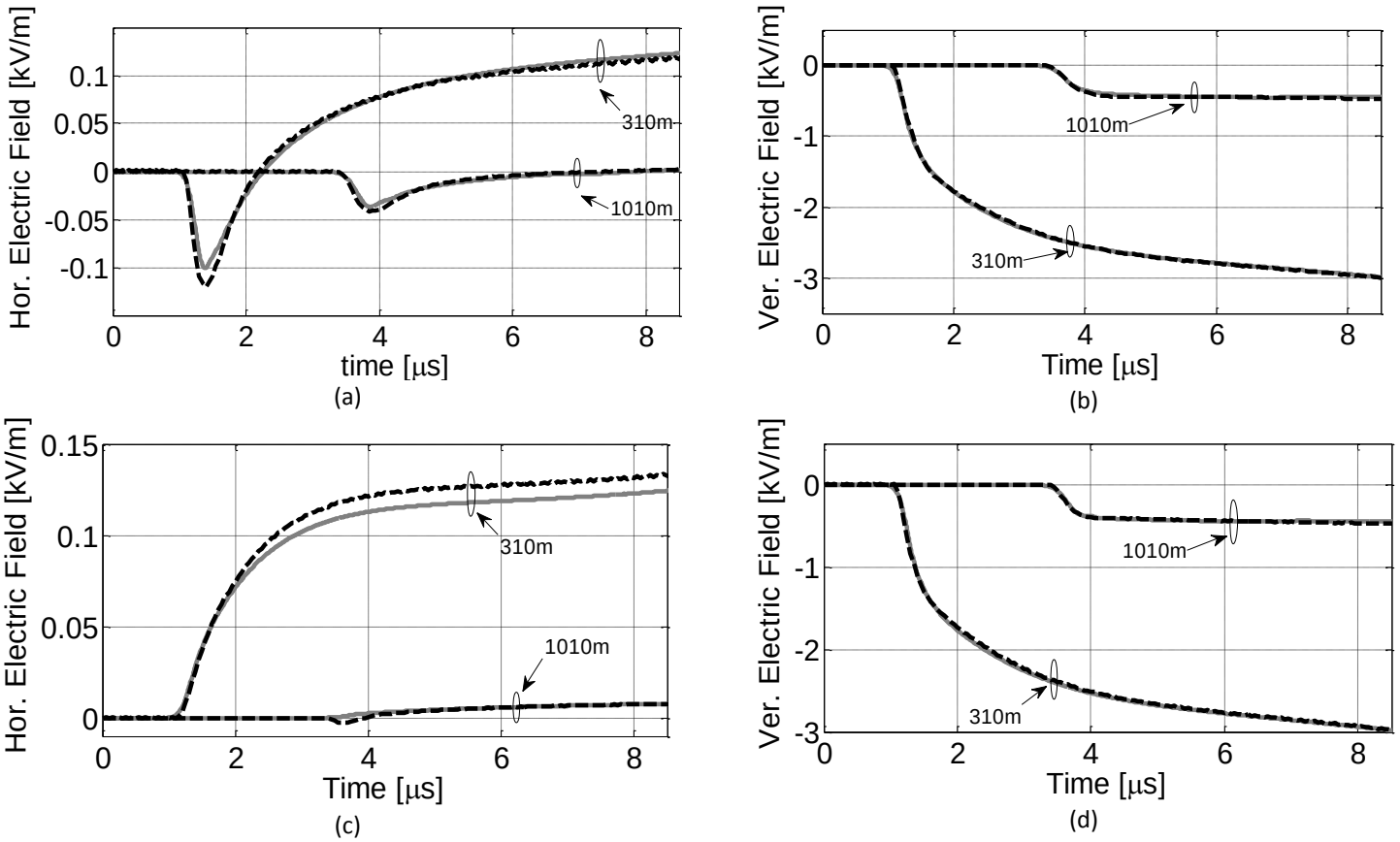

Figure 73 Radiated Electric Field Components along a Mixed-Path of two-sections. (Dashed Line: Wait's Formulas, Solid Line: FDTD Method) Case 1: 10 Ωm / 1000 Ωm (a) Hor. Electric Field (b) Ver. Electric Field, Case 2: 1000 Ωm / 10Ωm (c) Hor. Electric Field (d) Ver. Electric Field Case

As it can be seen in Figure 73(b) and Figure 73(d) the vertical electric field can be well reproduced by the Wait´s formula within the near field range. In both cases , the vertical electric field component prediction by the Wait´s formula agrees with the FDTD predictions with a relative error under the 1%. This validity has been also examined recently in [58] with different channel-base current waveforms for first and subsequent return stroke representations showing

reasonably accuracy for predicting the vertical electric field component at closer distances. However, Figure 73(a) and Figure 73(c) present important differences for the horizontal electric field calculation, especially for the case when the traveling electromagnetic wave goes from a lower conductivity ground to a higher one.

As it was presented in section 4.2.2 the Wait´s formula is valid for the far field range only and the vertical inhomogeneity boundary must be far enough from the radiating dipole. The differences observed in the horizontal electric field component can be caused by those approximations. As it can be seen from Figure 73(a) the results predicted by the Wait´s formula are in good agreement for most of the simulation time interval except for the peak calculation which is overestimated by the Wait's approach.

7 Lightning Induced Over-voltages

This section deals with the induced over-voltage calculation on the overhead lines due to a nearby lightning strike. At this point several effects on the lightning radiated fields due to the propagation path characteristics have been analyzed. One of the most common applications on the study of lightning radiated fields is the induced over-voltages on overhead lines, that is why the understanding of the propagation path effects on the lightning radiated fields are highly important to be characterized and accurately calculated in order to determine their effects on power quality due to the induced voltages adverse effects.

The electromagnetic coupling between lightning radiated fields and the overhead line has been typically analyzed by the incident-scattered field formulation. One of the most popular is that proposed by Agrawal [2], where the transmission homogeneous line equations are modified by external electromagnetic source due to the incident field. By means of this coupling model, the vertical and horizontal component of the radiated electric field can be included into the transmission line equations as external sources in a straightforward way. The incident-scattered field formulation has been one of the most used methods to calculate lightning induced voltages, in this formulation the induced voltages can be calculated using the electric field components [71] or using the magnetic field components [72] depending directly on the assumptions made for the lightning radiated fields calculation [73].

As it has been shown in previous sections, all of the approaches for the lightning radiated field calculations are based on far-field assumptions and cylindrical symmetry which is not adequate for most of the practical scenarios. Although, the far-field approaches can be used showing a good agreement with experimental results [23][23].

This section analyzes different effects on the lightning induced voltages that cannot be addressed by the approaches presented in literature and discussed in previous sections. To achieve this, the FDTD method will be used combined with the non-regular meshing algorithms developed in this thesis in order to represent typical configurations of overhead lines. As several simulation scenarios are not available to be compared with existent results in literature, a basis scenario of a flat lossy ground will be simulated in order to compare the effects on the lightning induced voltages due to the inhomogeneities and non-uniformities of the ground.

7.1 Overhead Line Modeling and Electromagnetic Coupling

As it has been discussed along this thesis, there are many factors that can contribute to the radiated electromagnetic field components behavior. However, there is a last step in calculating the induced voltage on overhead lines; this step consists on exposing an overhead conductor to its influence in order to calculate not only the induced voltages along it, but also the induced currents that will be propagating along the line and reaching its ends. Lightning induced voltages has been characterized by many authors in order to determine the most considerable factors that influence the power quality indicators of overhead distribution networks [75].

7.1.1 Perfectly Conducting Ground and Homogeneous Ground

There has been shown that the presence of a homogeneous conductive ground, when a nearby lighting return-stroke occurs, is able to modify the induced voltages waveforms and its peaks value on an overhead line. A FDTD simulation set-up was performed using the representation of an overhead line by means of a horizontal thin wire with 1km in length and 10m in height. The radius of the overhead line was assumed to be 5cm. Figure 74 shows a comparison of a lightning induced voltage calculation by means of the FDTD method implemented in this work and those results presented in [76] also using the FDTD method.

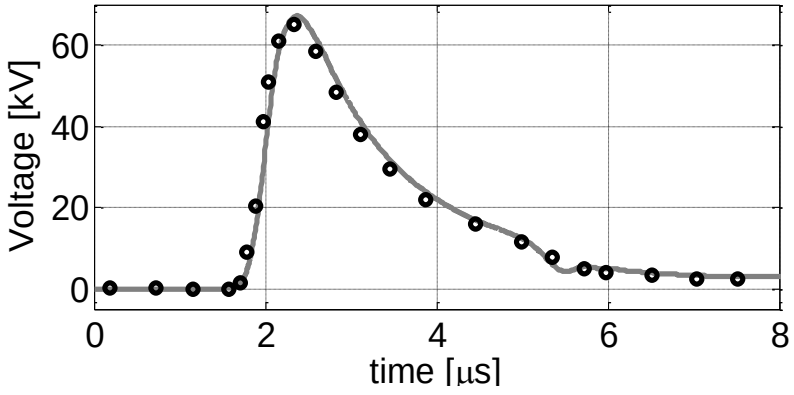

(a)

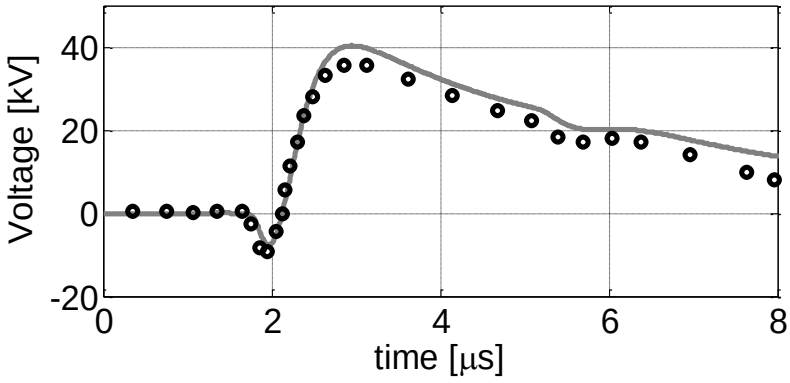

(b)

Figure 74 Calculated Induced Voltages on a 1km at 50m from the lightning strike (solid: FDTD, circles: presented in [76])

As it can be seen from Figure 74, the induced voltages are highly modified by the presence of a finite conducting ground. Figure 74(a) presents the induced voltage assuming a perfectly conducting ground and when these results are compared with those obtained for a lossy ground of 1000 Ωm shown in Figure 74(b), several differences in the waveform can be evidenced.

One of the most interesting results between Figure 74(a) and Figure 74(b) is that the presence of the lossy ground can include a change the polarity of the induced voltage. This effect is caused by the incident lightning radiated field waveform, especially due to the same change of polarity present in the horizontal electric field. As it was presented in section 6.2, the lossy ground affects mainly the horizontal electric field component and its resulting waveforms exhibit a negative excursion for the first time instants. These polarity changes interact with the overhead line yielding to induced voltages having a similar behavior.

7.1.2 In-homogeneous Ground

This section pretends to evaluate some of the effects of the inhomogeneities on the lightning induced voltages.

7.1.2.1 Mixed-Path condition

The Mixed path condition was demonstrated to contribute representatively to the lighting radiated field waveforms in section 6.3.1. Hence, the induced voltages waveforms related to those incident fields will be also affected. In order to analyze the effects of the non-homogenous ground on induced voltage calculations, an overhead transmission line illuminated by the electromagnetic field produced by a lightning channel striking at 50 m from one of its ends is considered. The calculation was performed using a regular mesh implementation of the FDTD method as

mentioned before. A schematic draw of the simulation set-up is depicted in Figure 75. This case of study was also presented in [77].

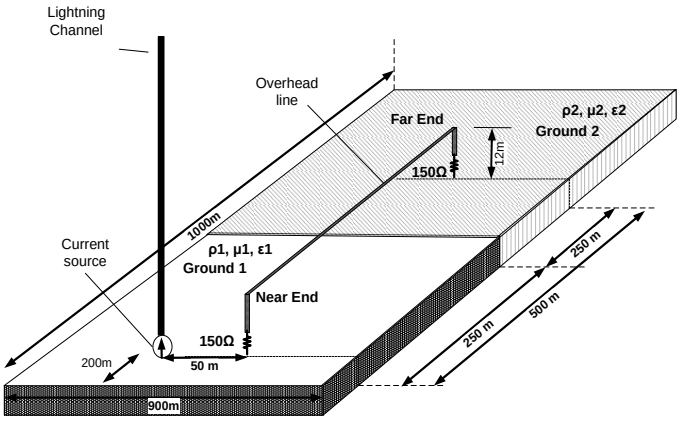

Figure 75 Simulation setup for the induced voltage calculation on an overhead transmission line above vertically stratified ground due to a lightning channel at 50m of one of the ends (near end NE) and both ends connected to a resistor of 150Ω.

The lightning return-stroke was modeled by means of a RL-series loaded thin-wire conductor as presented in section 5.3. The radius of the channel was 0.3 m with 1.5 km in length; the distributed inductance value used was of 3 μH/m and the value for the series resistances 1 Ω/m in order to obtain a velocity of propagation about one half of the speed of light. The total working volume of $1000 \times 900 \times 2000$ m^3 was divided with cell sizes of $5 \times 5 \times 2$ m^3 and CPML boundaries were placed at the top and all sides of the domain in order to simulate an unbounded medium. The distribution overhead line under study has been assumed to be at 12 m above ground with a radius of 15 mm and 500 m in length terminated at each extreme with a 150Ω resistance. The Umashankar's thin-wire model was used for the overhead conductor as discussed in detail in chapter 3. [40]

The ground is first assumed to be homogeneous (case I and case II). Then, a mixed-path is analyzed (case III and case IV) and induced voltages at the line ends are compared with those obtained for the homogeneous condition. The ground relative permittivity and permeability have been assumed to be for all simulations as ε_r=10 and μ_r=1 respectively and the lightning strike location was defined to be always on one side of the mixed-path. A resume of the simulated cases is referred in Table 2.

Case	Ground resistivity configuration		
	Ground along Propagation Path	**Ground 1 ρ1[Ωm]**	**Ground 2 ρ2[Ωm]**
I	Homogeneous	10	10
II	Homogeneous	1000	1000
III	In-Homogeneous (mixed path)	10	1000
IV	In-Homogeneous (mixed path)	1000	10

Table 2 Simulated Cases Description

Figure 76 shows the horizontal electric field components for the second section of the mixed-paths considered in the simulation. As it is shown in Figure 76(b), the presence of the mixed path section does not influence in a representative way the vertical electric field component. However, the horizontal electric field component is markedly affected by the mixed-path structure.

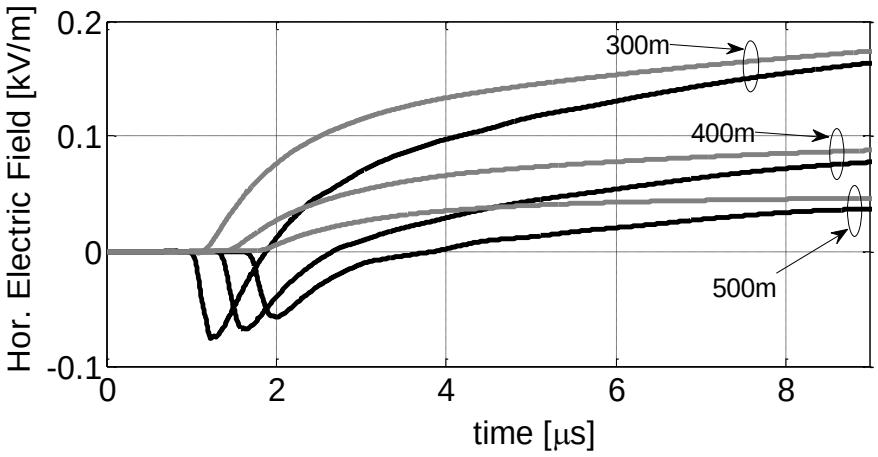

(a)

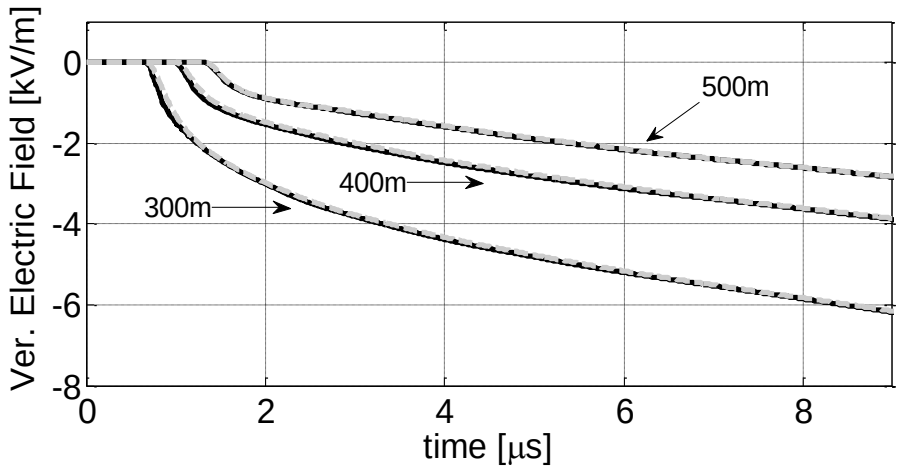

Figure 76 Electric field components above the second mixed path section (Black: 10 Ωm / 1000 Ωm case, Gray 1000 Ωm / 10 Ωm case) (a) Horizontal electric field over a mixed-path ground (b) Vertical electric field over a mixed-path ground

As it can be seen from Figure 76(a) for case III, when the wave propagates initially along a ground of 10 Ωm it suffers almost no distortion when compared to a propagation along a perfectly conducting ground. Once it starts to propagate along the 1000 Ωm ground, it is strongly distorted changing its polarity for the first microseconds (black line). On the opposite case (case IV), the wave starts to propagate above a highly lossy ground but when it enters to the 10 Ωm section, it recovers the features of a propagation above an almost ideal ground. This leads to the differences between the induced voltages calculated for the homogeneous and the in-homogeneous cases as is presented in Figure 77.

Figure 77(a) presents the induced voltages at the near end. It is worth noting that the mixed-path under the overhead line changes the surge impedance along the line, resulting in a wave reflection; the wave front maintains the same behavior as its homogeneous counterpart until the wave arrives at the mixed-path division between the two grounds.

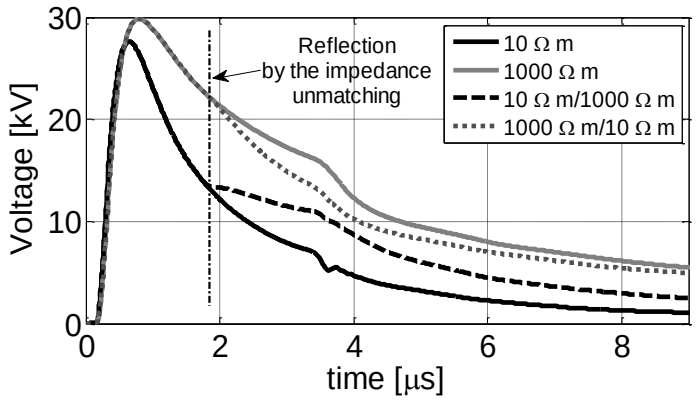

(a)

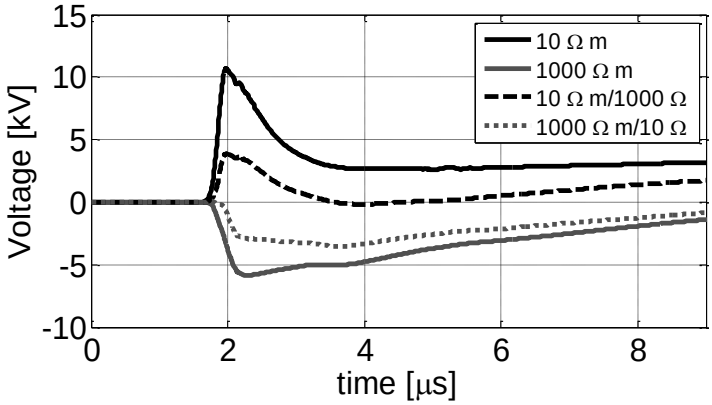

(b)

Figure 77 (a) Induced voltage at near end (b) Induced voltage at far end.

As it has been discussed along this thesis and taking as reference the Agrawal´s formulation, the lightning induced voltage on overhead lines is highly dependent of the incident radiated electric field generated by nearby lightning strikes, and it has been demonstrated that there is an important effect on those radiated electric field components due to the ground conductivity changes, especially for the horizontal component. Due to this, some differences on the induced voltages are expected. However, once the overhead line is reached by the incident radiated field, the induced voltages are also dependent on the line parameters which can play an important role of the voltage waveforms at the line terminations.

Figure 78 shows the variation of the reflection factor along the overhead line for each considered mixed-path case assuming a TEM propagation mode. Despite the magnitudes of the reflection factor are the same for both cases, it can be seen an important difference on the phase of the reflection factor, being almost zero degrees for the 10 Ωm / 1000 Ωm case and about ±180°for the

1000 Ωm / 10 Ωm case; this means that the reflection for the latter case is negative at the division between the two grounds. This situation reduces the voltage reflected at the near end of the line once the reflected traveling wave reaches it (dotted line on Figure 77(a)). For the first case (10 Ωm / 1000 Ωm) the reflection factor results positive, increasing the voltage at the near end (black dashed waveforms on Figure 77(a)).

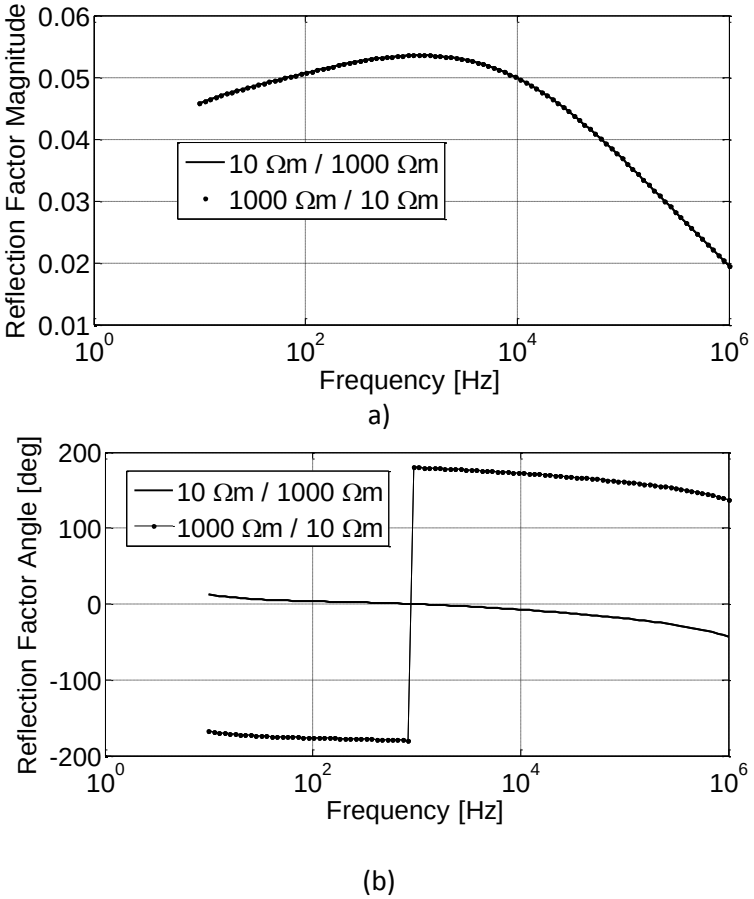

Figure 78 (a) Reflection factor magnitude (b) Reflection factor phase.

As it is shown in Figure 77 (b) the far end induced voltages have been highly affected by the mixed path condition when they are compared with the homogeneous case. Although their polarity coincide with the polarities obtained for the homogeneous case, the magnitude of the induced voltages is reduced to almost two to three times compared to those voltages obtained from the homogeneous case. This effect can be understood by the horizontal electric field behavior presented in Figure 76(a)). For case III, the lightning electromagnetic field initially travels above a low resistivity ground; as this value changes on the second half of the line to a high resistivity value, the contributions of the horizontal electric field coupled to the line tend to reduce the induced voltage due to the negative polarity presented on them (Black waveforms on Figure 76(a)). For Case IV the same occurs, the horizontal electric field coupled to the line also tends to reduce the induced voltage; in this case the induced voltage results in a lower magnitude due to

the positive polarity contributions of the horizontal electric field coupled on the second section of the line (Gray waveforms on Figure 76(a)).

Recently, the mixed-path effects on lightning induced voltages has been addressed by using full-wave approaches in order to validate several approximations and the examination of their consequences on the induced voltage waveforms characteristics [19][78]. An additional case of the mixed-path condition is presented in Figure 79(a), this scenario was also presented in [78] as a representation of a river-crossing overhead line. The results were obtained using the finite element method (FEM) for the solution of the magnetic vector potential representation in the time-domain.

In this case, the scenario was implemented into the FDTD method by using the non-regular mesh algorithm developed in this thesis. The lightning channel was simulated by the MLTE model using a typical double-exponential function for the subsequent return-stroke current representation; the parameters of the lightning return-stroke current were the same as those used in [78]. The three-section mixed-path effects were calculated for three cases. The first case represents the homogeneous case with a ground resistivity of 1000 Ωm and a relative permittivity of 10. The second case was assumed as a river-crossing overhead line where the ground conductivities were assumed to be 1000 Ωm/0.25 Ωm/1000 Ωm with relative ground permittivities of 10/30/10 respectively. A last simulation case represents a dry-sand-crossing overhead line where the ground conductivities were assumed to be 1000 Ωm/10000 Ωm/1000 Ωm. For the case under study the relative permittivities remained unaltered with the same values as in the second case. Table 3 presents a summary of the cases taken into account.

Case	**Ground resistivity configuration**			
	Propagation Path	**Ground 1 ρ1[Ωm]**	**Ground 2 ρ2[Ωm]**	**Ground 3 ρ3[Ωm]**
I	Homogeneous	1000	1000	1000
II	River-crossing representation	1000	0.25	1000
III	Dry Sand-crossing representation	1000	10000	1000

Table 3 Three-section mixed path cases resume

As it can be seen from Figure 79(b) both methods are in good agreement for the induced voltage predictions at both line terminations. Some of the differences between the predicted waveforms could be explained by the overhead line representation used in both simulations.

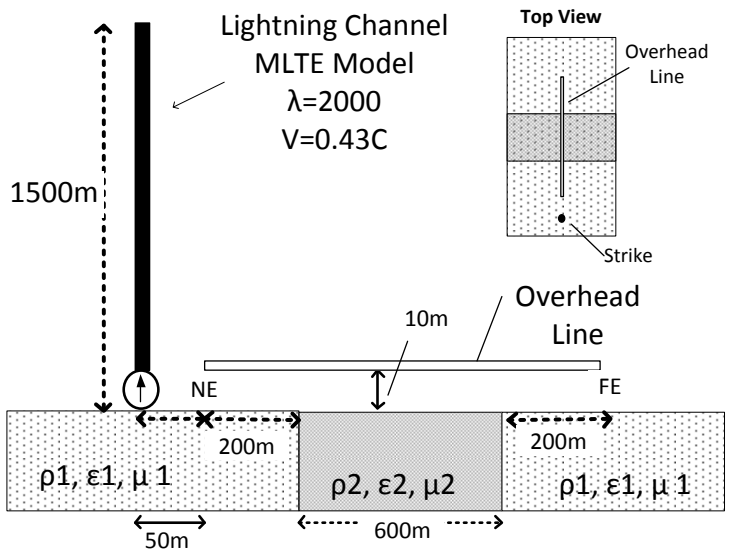

(a)

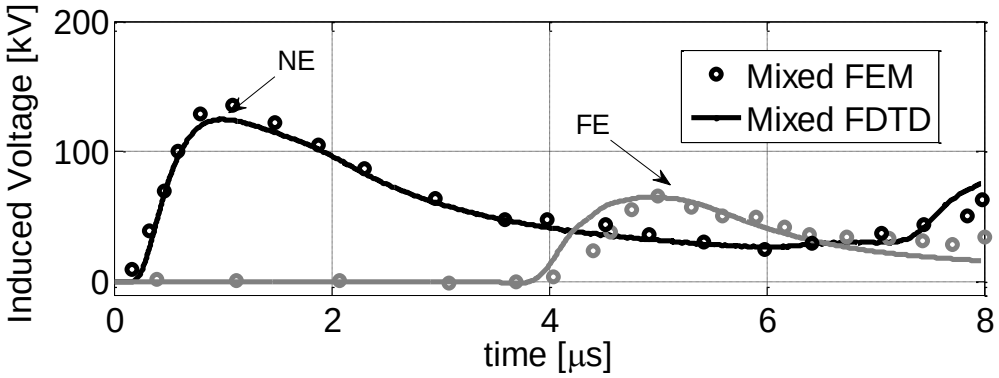

(b)

Figure 79 (a) Relevant geometry of the simulation set-up (b) Comparison of the induced voltages by using the FEM method and the FDTD method (circles: FEM, solid: FDTD)

The results presented in Figure 79(b) are compared with the homogeneous case and the comparison is presented in Figure 80 for the near and far end. The results at the near end are in agreement with the analysis presented before for the two-section mixed path; As in the two-section mixed path the reflected wave from the first impedance change in the case II (1000 Ωm/0.25 Ωm/1000 Ωm) leads to a decrease of the near end induced voltage (dashed line in Figure 80(a)). However, the increasing of the ground conductivity due to the second mixed-path affects representatively the far end induced voltage. This behavior can be related with the behavior of the horizontal electric field component as in the simulation set-up presented before. As it was presented in section 6.3.1, there is a "recovery effect" (there is no a bipolar waveform above the high conductivity section) of the horizontal electric field component when traveling from a high resistivity soil to a low resistivity one, increasing the contribution of this component on the electromagnetic coupling with the overhead line and leading to a higher induced voltage at the far

end. In the other hand, the third case represents a positive reflection coefficient at the first mixed path section leading to a higher voltage at the near end, being again in agreement with the results presented for the two-section mixed-path analysis (dotted line in Figure 80(a)). As the middle section presents a higher resistivity ground value, the horizontal electric field component decreases its contribution on the induced voltages at the far end due to the change of polarity evidenced in section 6.3.1.

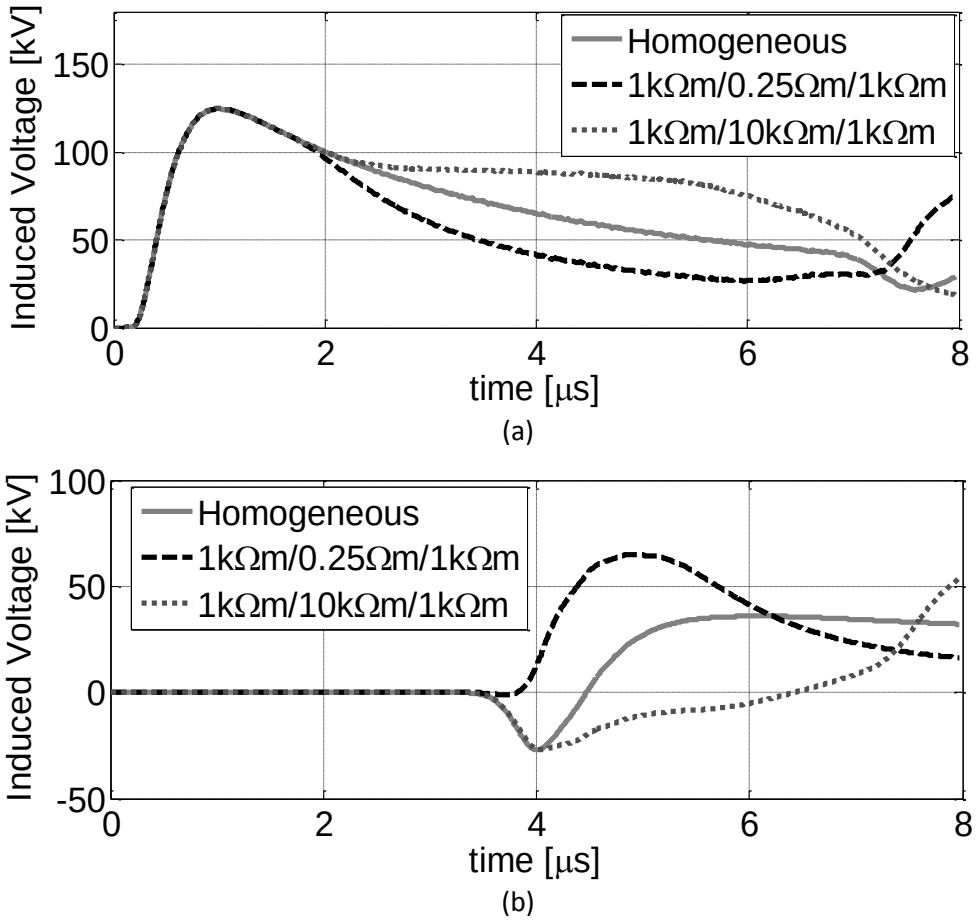

Figure 80 Induced Voltages for a Three-section mixed-path (a) Near End (b) Far End

As it has been presented in this section, the mixed propagation path for the lightning radiated fields, could lead to a variation of the induced voltage waveforms and magnitudes when compared with the homogeneous lossy ground case. The effects that have been evidenced are multi-variable dependent and the total result is obtained by several contributions, however two main features can be derived from the induced voltage characteristics in presence of a mixed-path: First, the calculation of the surge impedance of the overhead line can be useful for a qualitative description of the reflected waves at the division of the mixed-paths and their contribution to the induced voltages at the line terminations and second, the effects of the mixed-path on the components of

the lightning radiated electric fields lead to strong variations on the induced voltages due to the electromagnetic coupling with the overhead line.

7.1.3 Non-Uniform Ground Effect

This section presents some results of lightning induced voltages due to a typical subsequent return stroke current waveform where different ground irregularities are present. The non-uniform ground effect on the induced voltages was taken into account by means of the full-wave solution based on the FDTD method and using the non-regular meshing method developed in this thesis and discussed in detail in section 3.8.

The first simulation case corresponds to a lightning striking at the top of a step mountain which induces an overvoltage on a single overhead line located at the bottom of it; Figure 81(a) depicts the geometry for the case under study. The lightning return stroke current was simulated by means of a MTLE model with velocity of propagation of 0.3 times the speed of light and a constant decay λ=1700. The overhead line is 1km in length and 10m in height, and was represented as a thin-wire with 1cm in radius by using the INY model presented in section 3.7.4. The line has been terminated with a 330Ω resistor at each end. The ground resistivity was assumed to be 1000Ωm and a relative permittivity of $10\varepsilon_0$.

Similar situations have been analyzed in literature when the lightning strikes to nearby conductive tall objects and tall structures, and the effects on the induced voltages are related with the multiple reflections of the current occurring between the top of the structure and the ground [25]. In this scenario no current reflections are considered along the channel, only the effects on the induced voltages due to the radiated fields caused by the ground geometry are taken into account.

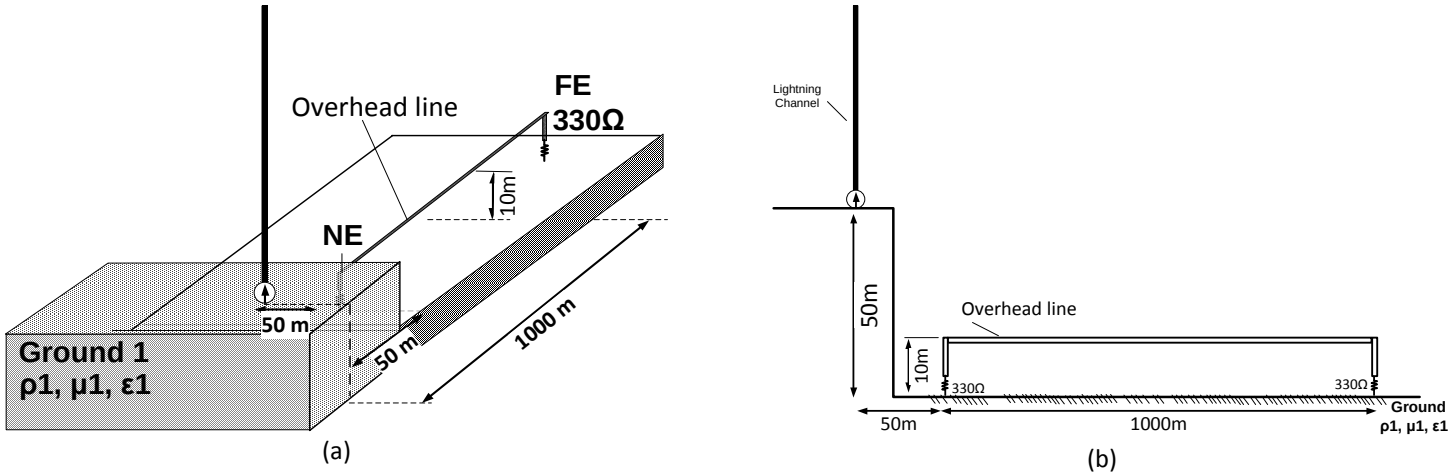

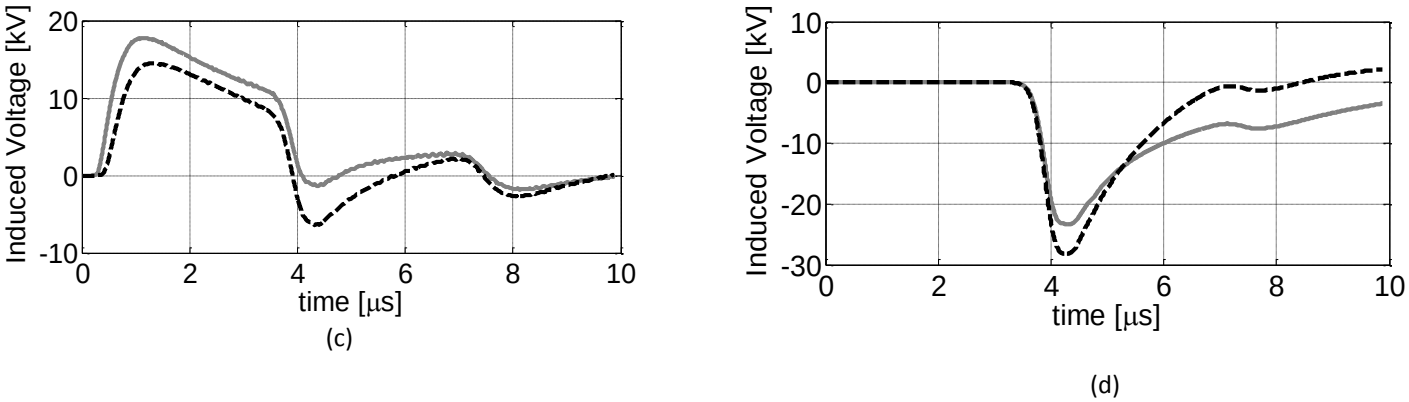

Figure 81 Geometry for the calculation of the induced voltages for a lightning strike on the top of a step mountain (Solid: Flat Ground, Dashed: Irregular Ground) (a) Relevant Geometry for the simulation set-up (b) Side view along the center of the mountain along the X-axis direction (c) Induced voltage at the near-end (d) induced voltage at the far-end

Figure 81(c) and Figure 81(d) show the induced voltages calculated at the near and far end. As it can be seen from Figure 81(c) there are two important effects on the peak magnitude on the induced voltage at the near-end when compared with the flat ground case: first a reduction on the peak-magnitude due to the relative distance between the channel base and the near-end location, and second, due to the presence of the step-terrain profile a "shadow effect" for the radiated field is present at points nearby this end as it was discussed in section 4.3.2. The induced voltage at the far-end presents an increase of the magnitude of about 30% above the flat ground case as it is shown in Figure 81(d).

A similar case is presented in Figure 82(a-b). In this case the overhead line is on the top of a step mountain and the lighting strikes to the bottom of the terrain profile. The same ground parameters and lightning channel model were used as in the previous case. The induced voltages at the near and far end are presented Figure 82(c) and Figure 82(d) respectively.

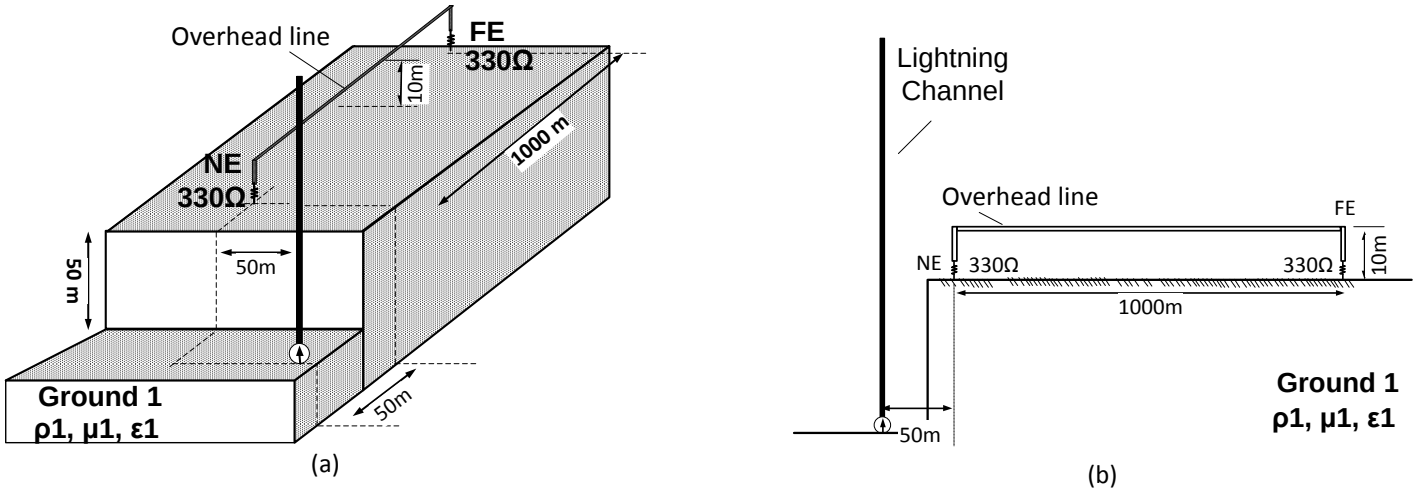

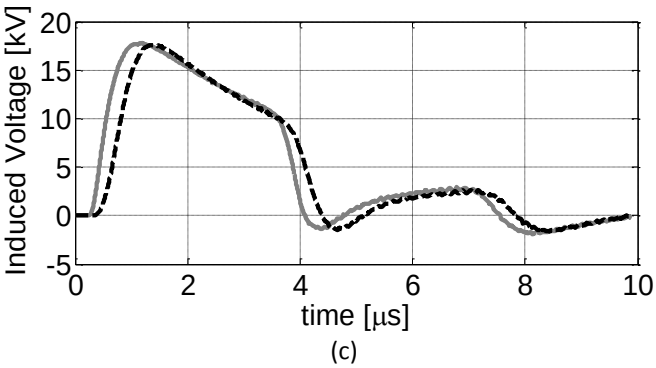

(c)

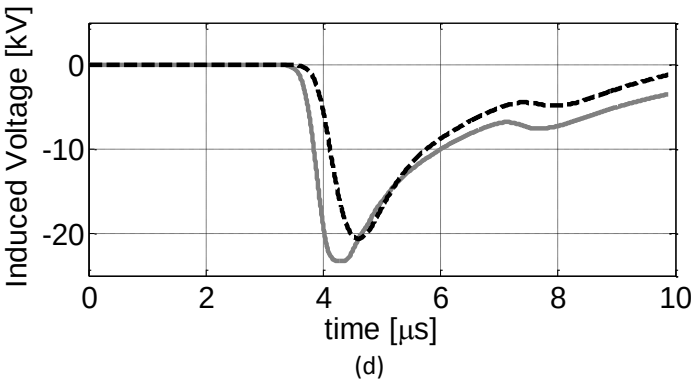

(d)

Figure 82 Geometry for the calculation of the induced voltages for a lightning strike on the bottom of a step mountain (Solid: Flat Ground, Dashed: Irregular Ground) (a) Relevant Geometry for the simulation set-up (b) Side view along the center of the mountain along the X-axis direction (c) Induced voltage at the near-end (d) induced voltage at the far-end

As it can be seen from the induced voltages at both terminations, there is an expected delay on the time of arrival of the incident field due to the first propagation path from the bottom of the step mountain where there is no interaction with the overhead line.

As it can be seen from Figure 82(d), there is a decrease of the magnitude of the induced peak-voltage at the far-end when compared with the flat ground case. For this scenario in contrast to the situation presented in the previous case of study, the far-end of the line is being "shadowed" by the terrain step-profile leading to a lower voltage magnitude. On the other hand, at the near-end a small decrease of the peak-magnitude is expected due to the current attenuation along the lightning channel. However, as it is a short length compared with the length of the channel and the distance to the overhead line remains unaltered, the attenuation effect and the radiation pattern of the lightning return-stroke is not considerably affected and the results are almost the same in magnitude and waveform as in the flat ground case, this can be also evidenced in Figure 82(c).

In order to include a more realistic terrain profile, a case of lightning induced voltages due to a lightning striking to the top of a mountain is presented in Figure 83(a). In this case the mountain is represented by a Gaussian. The simulated overhead line was open at both ends and no riser wires were simulated. In this case the ground irregularity was included into the FDTD method by a set of several cubes with a resolution of 1m in height. Side views along X and Y axis of the implemented ground structure into the FDTD are presented in Figure 83(b) and Figure 83(c) respectively. The lightning channel was represented by the MLTE model with 1.5km in length, the velocity of propagation was imposed to be 0.43 times the speed of light and a constant decay λ=2000. Despite both line terminations are located symmetrically from the channel base, they will be named near and far end in order to keep the used notation and descriptions.

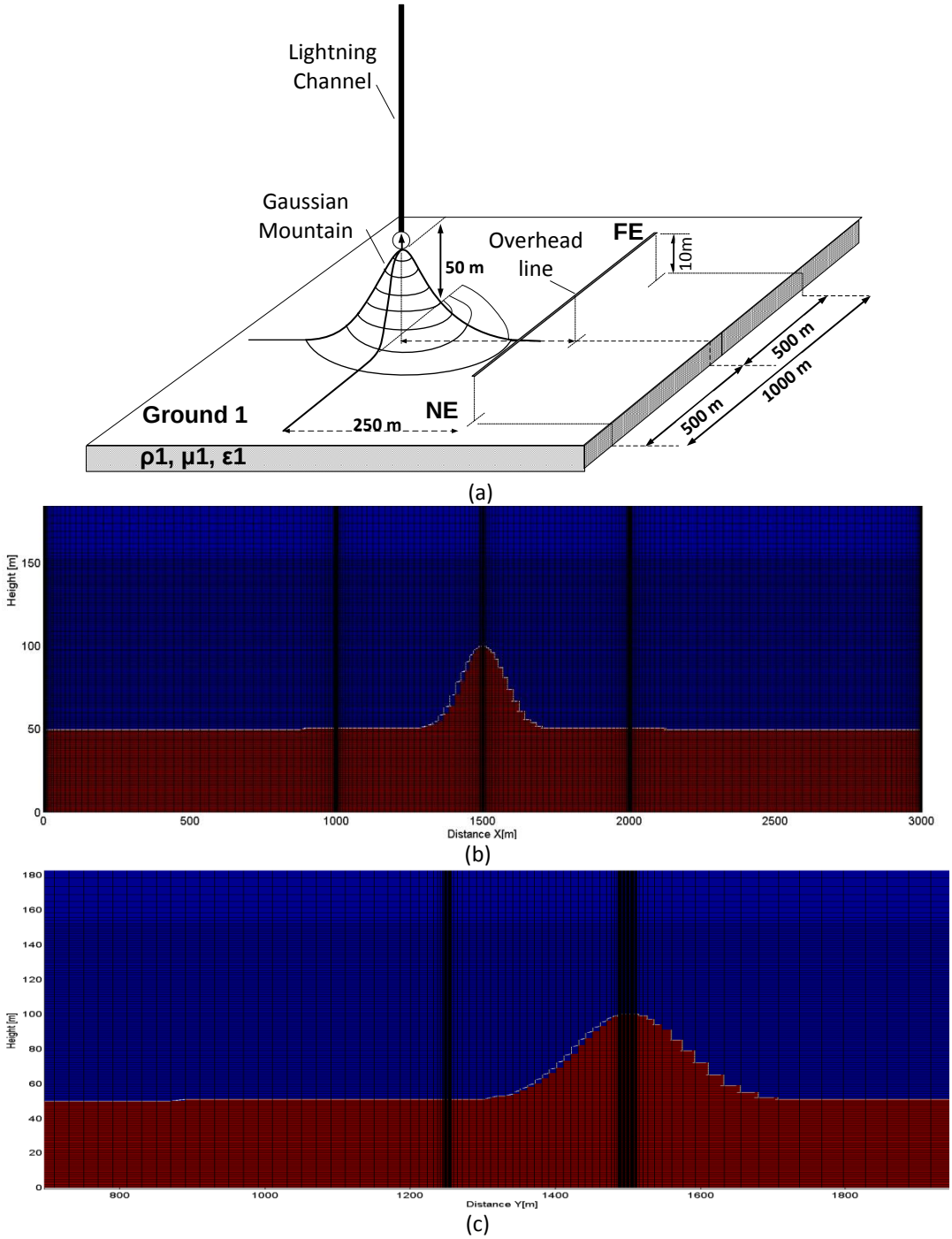

Figure 83 Geometry for the calculation of the induced voltages for a lightning strike on the top of a Gaussian Mountain (a) Relevant Geometry for the simulation set-up (b) Side view along the center of the mountain along the X-axis direction (c) Side view along the center of the mountain along the Y-axis direction

Figure 84 presents the induced voltages at the near and far end of the line. Similar results were presented in [28] by using a full-wave solution by means finite element method (FEM) for a striking point to the top of a cone-shaped mountain with a similar height. The proposed scenario

has an evident symmetry regarding distances to the lightning channel base and the terrain geometry is not causing important "shadowing effects" on any of the line terminations. Figure 84 presents the induced voltages for three different situations: the flat ground case in solid gray line, the cone-shaped mountain irregularity in gray circles and the Gaussians ridge mountain in dashed line.

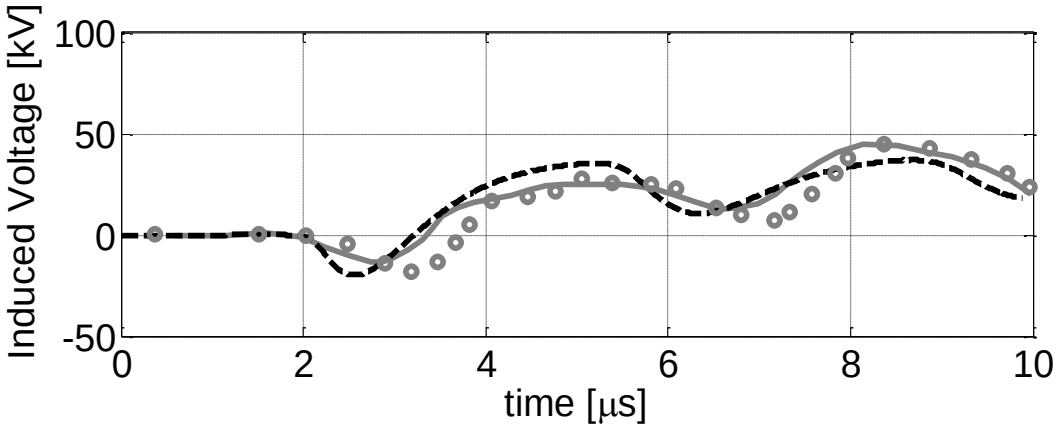

Figure 84 Induced voltages at near and far end due to a lightning strike on the top of a mountain (Solid Line: Flat Ground case with FEM, Dashed: Gaussian Mountain with FDTD, Circles: cone-shaped mountain with FEM presented in [28])

As it can be seen from the figure, there are not important differences in magnitude or waveforms between the three cases meaning that for the case under consideration, the effects of the terrain irregularities caused almost no distortion on the lightning propagated fields remaining similar to the flat ground case. It is worth noting that the slightly differences between the induced voltage waveforms are caused by the differences of the simulation approaches used.

The next simulation scenario is a typical case in rural distribution lines in mountainous regions. Figure 85 presents an overhead line on the top of a mountain and a nearby lightning striking to the flat ground area. This case can be seen as a variation of the last case. However, in this simulation the mountain has been extended along the overhead line path. In this simulation the overhead line was matched at both ends with a 450Ω resistor. The overhead line was simulated by means of the INY presented in section 3.7.4 with 5cm in radius and the lightning channel was simulated by means of the MLTE model with λ=1700 and a controlled velocity of propagation about 0.43 times the speed of light.

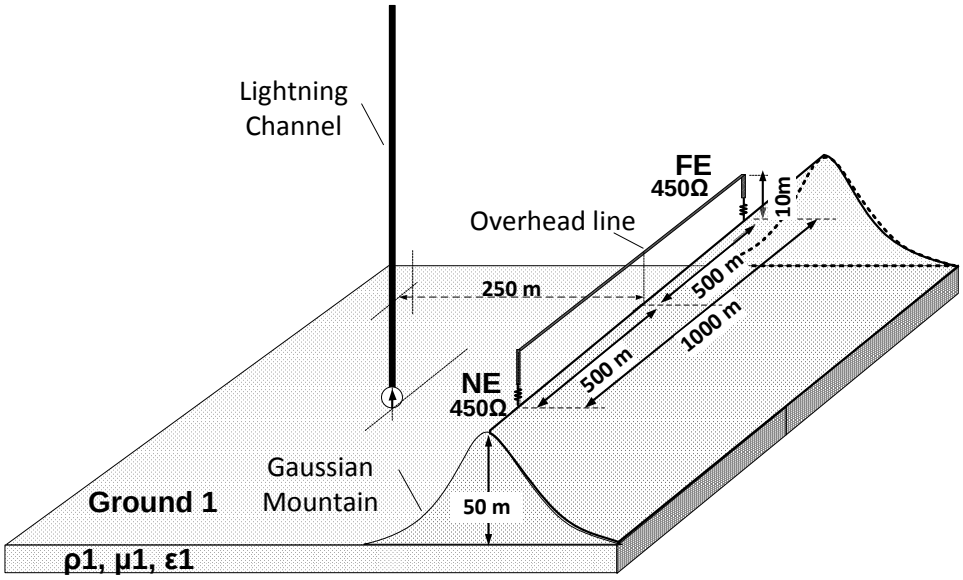

Figure 85 Overhead Line on the top of a mountain

In this scenario the location of the overhead line respect to the lightning channel lead to an increase of the induced voltage in almost 50% in its peak magnitude as is presented in Figure 86.

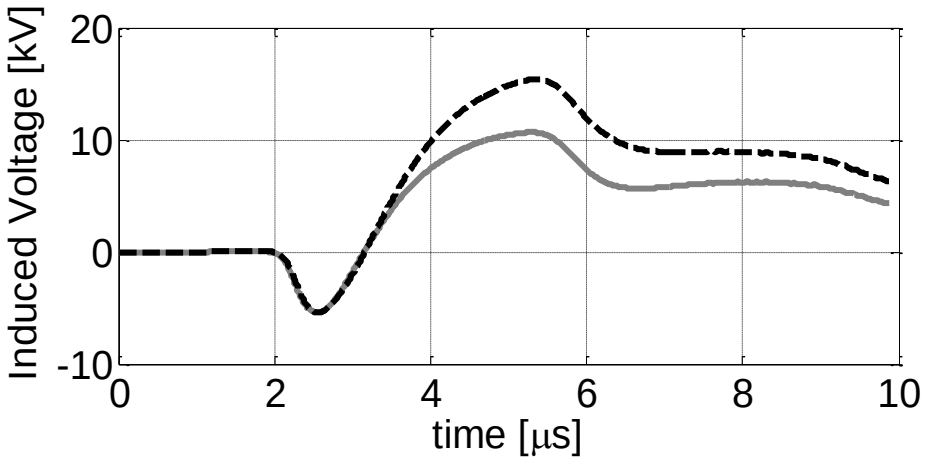

Figure 86 Induced Voltage for an Overhead Line on the top of a mountain (Solid Line: Flat Ground Case, Dashed: non-uniform ground)

It is worth noting that the induced voltage for the irregular terrain case presented in Figure 86 coincides for the first part of the waveform (about 3.4μs) with the flat ground case. In order to validate these effects of the previous scenario on the lightning radiated fields, a variation of the case presented before is depicted in Figure 87(a). In this scenario the overhead line is at the same ground level as the channel base and the mountain is located 200m behind the overhead line. The same ground parameters and lightning channel model as in the previous case was used.

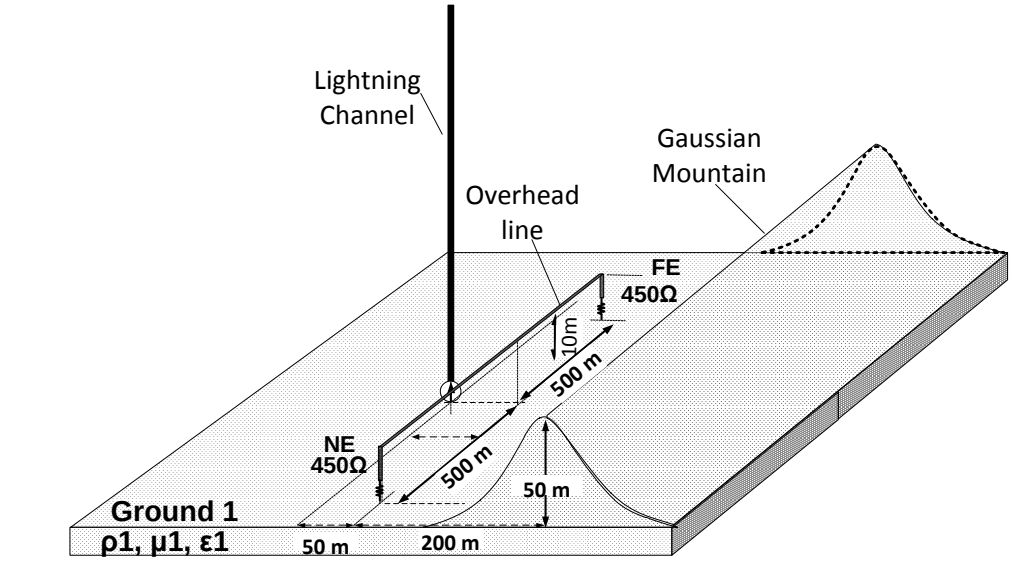

(a)

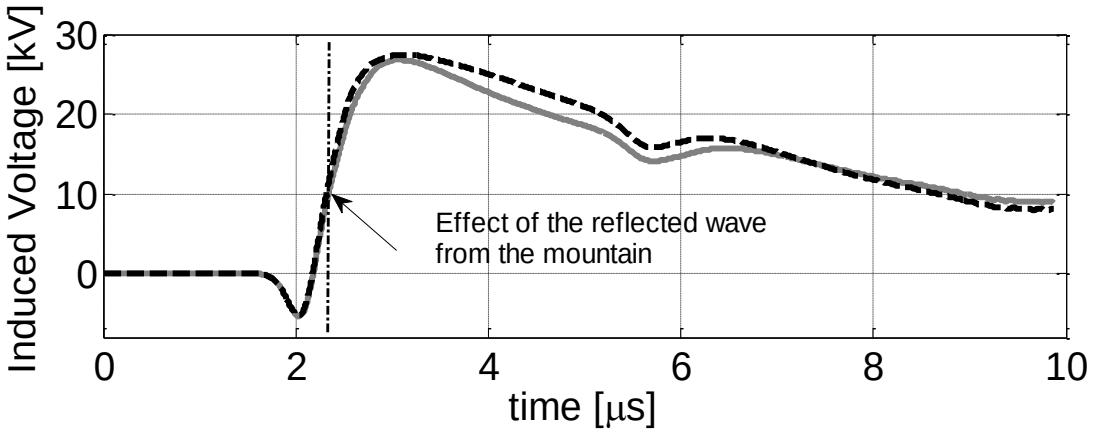

(b)

Figure 87 Induced Voltage for an Overhead Line with a mountain behind it (a) Relevant Geometry (b) Induced Voltage for an Overhead Line with a mountain behind (Solid Line: Flat Ground Case, Dashed: non-uniform ground)

Figure 87(b) presents the results of the induced voltage for the case under consideration. It can be seen that the difference between the irregular terrain case and the flat ground case begins once the reflected wave arrives from the mountain (at about 2.4μs). The effect of the reflect wave from the mountain behind the line represents less than the 3% in peak magnitude when compared with the flat ground but there can be observed differences of about 10% in some parts of the waveform due to the increase of the incident field at the overhead line location.

The next simulation cases are focused on the scenarios where the irregular terrain is under the overhead line. For these simulation scenarios the line parameters are highly affected by the irregular terrain and the interaction between the overhead line and the incident lightning electromagnetic field cannot be analyzed by using the uniform transmission line theory.

A typical case of an overhead line above non-uniform ground is presented in Figure 88, for this case the ends of the overhead line are located between two mountains. The same simulation parameters for the lightning channel and overhead line are used. The ground resistivity value remained unaltered in 1000Ωm. Near and far end names will be also used for referring the line terminations in the current case although they are at the same distance from the lightning channel base.

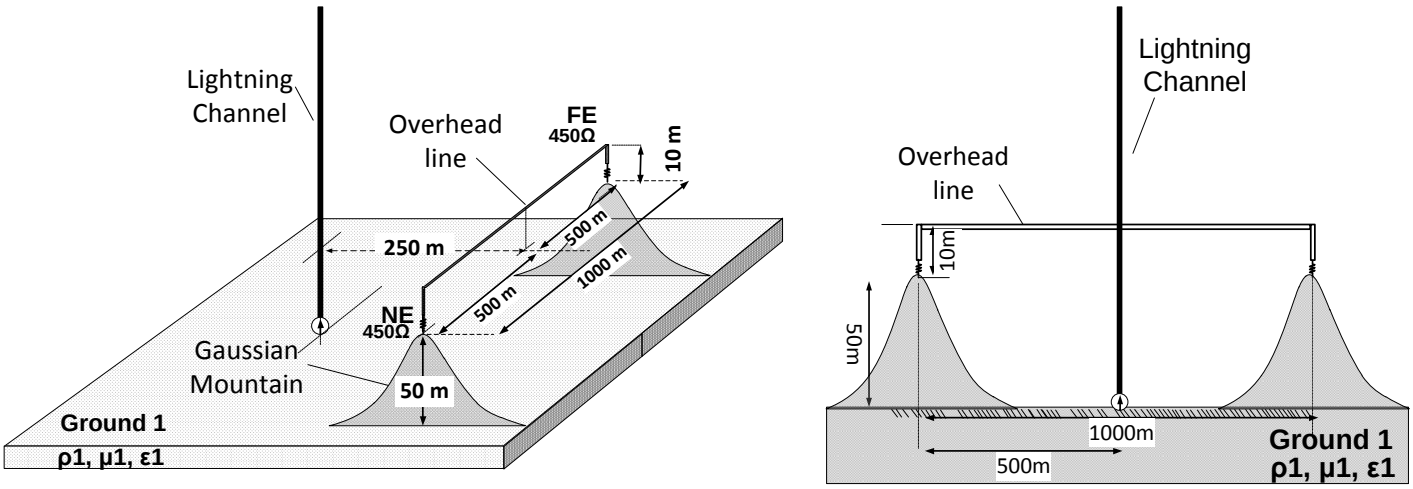

Figure 88 Overhead Line on between the top of two mountains (a) Relevant Geometry of the scenario (b) Side View

The comparison of the induced voltages between the non-uniform case and the flat ground case are presented in Figure 89. As it can be seen from the induced voltage for the irregular terrain scenario, the effect of the lightning electromagnetic fields and its interaction with the overhead line lead to almost three times the peak voltage magnitude for the homogeneous case.

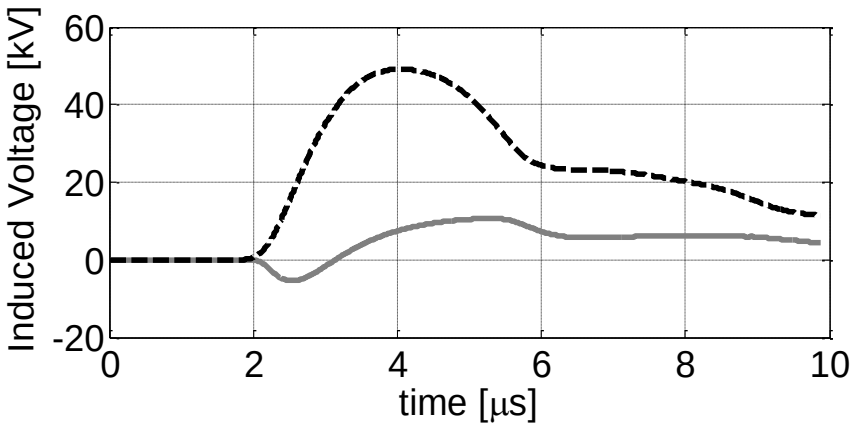

Figure 89 Induced Voltage for an Overhead Line between the tops of two mountains (Solid Line: Flat Ground Case, Dashed: non-uniform ground)

As it has been discussed along this thesis, the lightning induced voltage problem involves several parameters and variables that must be taken into account for the calculations, not only the effects

of the propagation path on the lightning radiated fields, but also the overhead line characteristics. The case under study presents both effects at the same simulation scenario. In order to address the line-parameters modifications due to the ground non-uniformity beneath the overhead line, a comparison of the calculated characteristic impedance for a single-wire overhead line for different heights is presented in Figure 90. These results show that under the TEM approach, the surge impedance increases with the relative height of the conductor to the ground level for a wide frequency band, therefore the propagating wave along the overhead line will face several reflections.

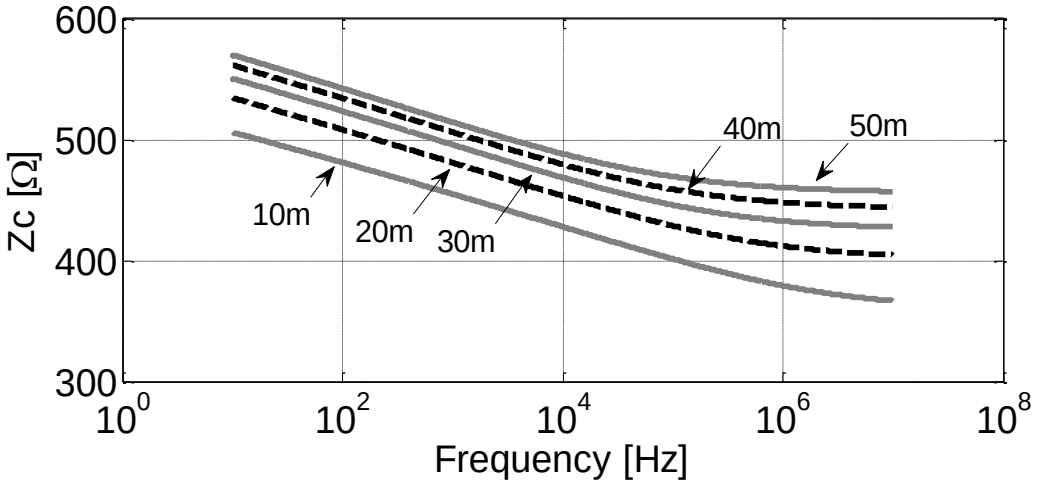

Figure 90 Characteristic impedance of a single-wire overhead line above 1000Ωm lossy ground depending on the conductor height by using the TEM approach

Based on the results presented in Figure 90 the increase of the induced voltage in Figure 89 is the result of a contribution of both effects: the propagation path effects and their electromagnetic coupling with the overhead line, and the line-parameter modifications which can lead to an increase of the induced voltage at both ends.

The next case of study quantifies the lightning induced over-voltages for a more realistic case of irregular terrains beneath the overhead line. For this case a cliff is present under the line as it is shown in Figure 91(a-b). In some practical situations there is not possibility for planting poles on the cliff bottom and two robust towers must be installed at each extreme of the cliff leading to a non-uniform line configuration. The lightning channel was simulated by means of a MTLE model with a velocity of propagation about 0.5 times the speed of light and a constant decay λ=1700. The simulation was performed assuming a ground resistivity of ρ1=1000Ωm and permittivity εr1=10. The overhead line is terminated with 330Ω resistors at both ends and the wire risers are also included at the line terminations. Despite both line terminations are located symmetrically from the channel base, they will be named near and far end for maintaining the used notation and descriptions.

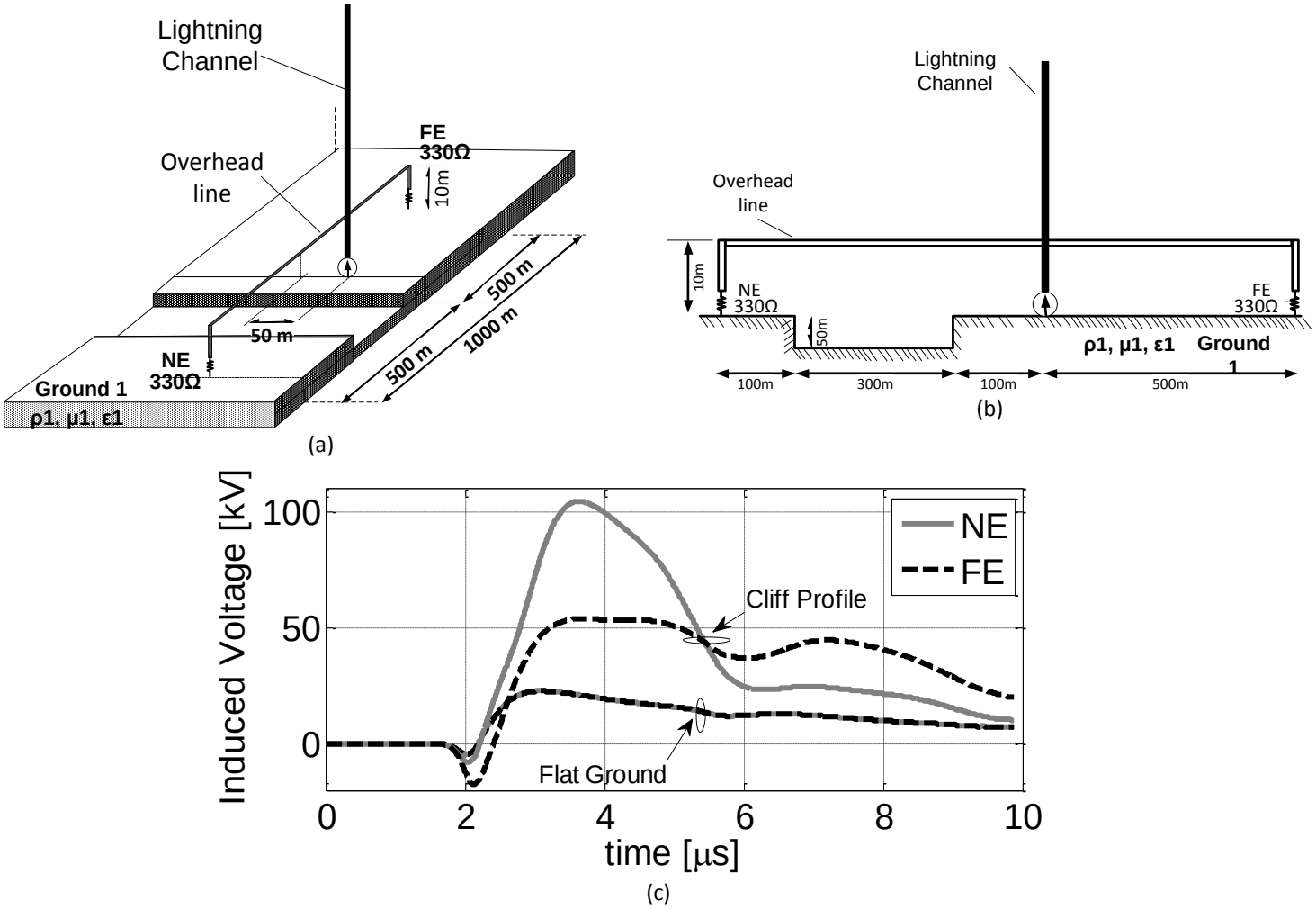

Figure 91 (a) Description of the Simulation Set-up for the irregular ground effects on induced voltages (b) Side View of the simulation set-up (c) Induced Voltage Comparison when a cliff is present under the ground

Figure 91(c) presents the comparison between the induced voltages on the near and the far end when a cliff is present under the overhead line compared with the flat ground induced voltage situation. As it can be seen, the presence of the cliff under the overhead line increases considerably the peak-value and the waveform at each ends of the line, reaching to almost 5 times the magnitude of the flat ground case.

It is worth noting that the induced voltages are not symmetric as in the flat ground case due to the location of the cliff section. This leads to a higher induced voltage at the near-end when compared with the induced voltage at the far-end. This result evidences the markedly effect that has the propagation path on the lighting radiated fields and the line-parameters modification for the induced voltage calculations.

An additional simulation based on the last case of study was performed in order to represent a river-crossing overhead line between two mountains. Figure 92(a) presents a combination between a cliff and a conductive change at its bottom which can be also seen a mixed-path condition for the propagating field. The simulation was performed assuming a ground resistivity of

ρ1=1000Ωm and permittivity εr1=10 for the ground. The cliff section at the bottom was simulated with a ground resistivity of ρ2=100Ωm and permittivity εr2=10. The same names as in the previous case will be used to refer the ends of the overhead line.

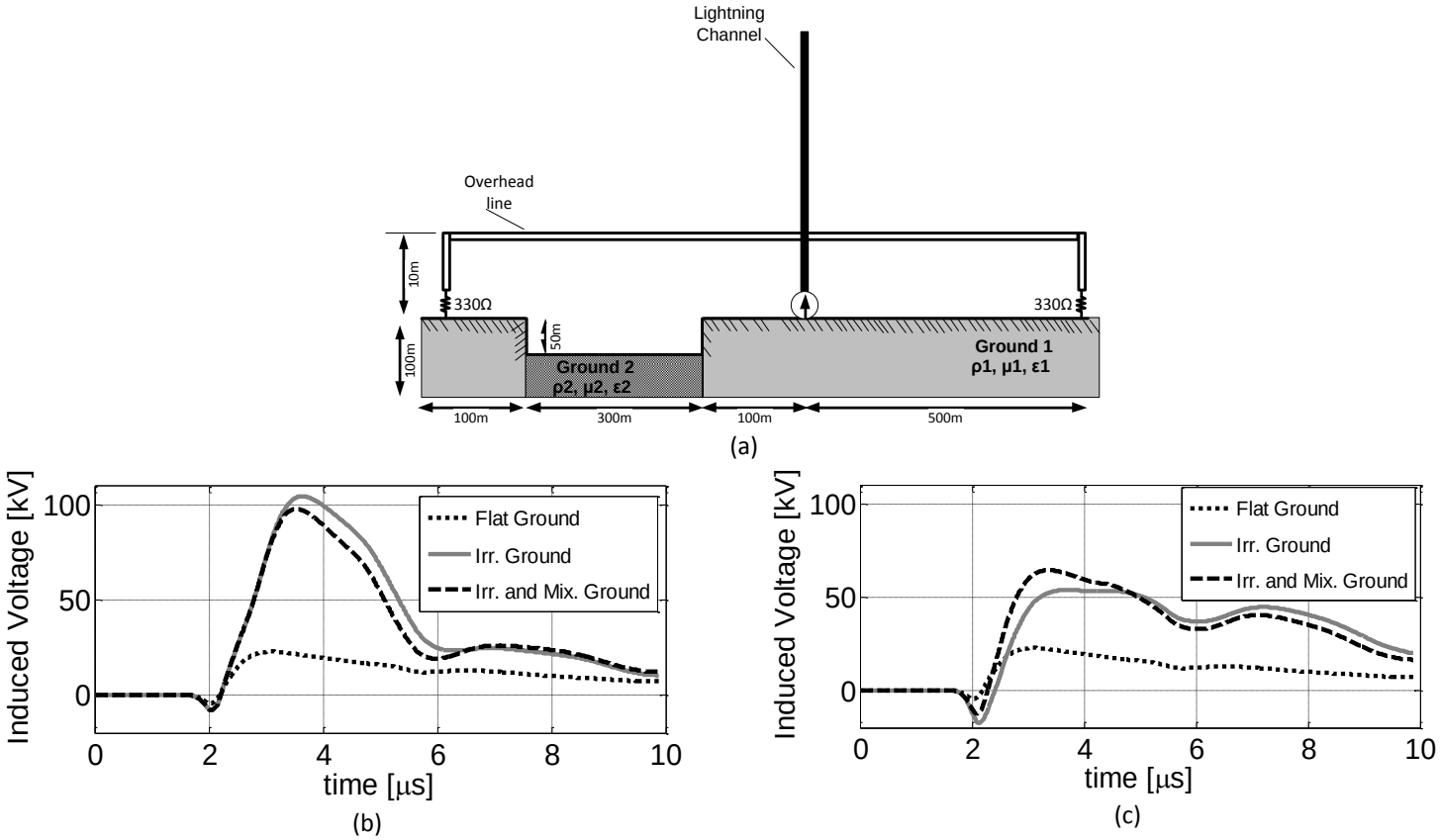

Figure 92 (a) Irregular and Mixed Path Ground structure for Induced voltages calculation (b) Induced Voltage at the near end (c) Induced Voltages at the far end

Figure 92(b-c) presents the comparison between the cliff condition without change of resistivity at its bottom and when the ground resistivity at its bottom is decreased. As it can be seen from the induced voltages waveforms presented in Figure 92(b-c), the effect of the change of the resistivity value at the bottom of the cliff is reducing the induced peak voltage at the near end and increasing it at the far end, this effect can be also associated to the modifications of the radiated electric fields due to the ground conductivity influence and on the line parameters.

8 Conclusions Remarks and Future work

This thesis dealt with all of the three aspects of the lightning induced voltage problem: return stroke models, calculation of lightning radiated fields and the evaluation of the induced voltages on single-phase overhead lines.

Several methods used nowadays for evaluating lighting radiated fields were analyzed in this thesis showing their theoretical basis and specifying their limitations, especially for calculations within the near field region.

A full wave solution was implemented using the FDTD Method including a non-regular mesh in order to represent different geometric features and allowing adequate near-field interactions calculation. The implemented FDTD scheme based on a non-regular meshing algorithm, allowed the representation of the ground irregularities and the overhead lines with a finer mesh and a coarser domain was used the rest of the problem space. An experimental case of a typical cross-talk problem was analyzed using the classical implementation of the FDTD and the non-regular mesh approach, showing its advantages over the classical formulation in representing larger problem space dimensions and lesser number of Yee's cells.

By means of the proposed methodology for representing the problem space by means a non-regular mesh, the calculation of lightning induced voltages became available including complex geometry into the simulation scenario in order to achieve more realistic representations of actual situations.

The effects on the lightning radiated fields due to the presence of different propagation paths were analyzed along this thesis showing their representative influence especially for the horizontal electric field. Several approaches based on far-field formulation and cylindrical symmetry regarding geometry were analyzed and compared with the full-wave solution by using the FDTD method, showing that those approaches could lead for some of the cases to an over or under estimation in the calculations of the radiated field components.

The mixed propagation path for the lightning radiated fields, lead to a variation of the induced voltage waveforms and magnitudes when compared with the homogeneous lossy ground case. The effects that have been evidenced are multi-variable dependent and the total result is obtained by several contributions. However, two main features can be derived from the induced voltage characteristics in presence of a mixed-path: First, the calculation of the characteristic impedance of the overhead line can be useful for a qualitative description of the reflected waves at the division of the mixed-paths and their contribution to the induced voltages at the line terminations and second, the effects of the mixed-path on the components of the lightning radiated electric fields lead to strong variations on the induced voltages due to the electromagnetic coupling with the overhead line.

Regarding irregular grounds, relatively important effects on the induced voltages were obtained when an effect of “shadowing” is present for some segments of the overhead line and the irregularities are larger enough to diffract part of the radiated fields. However, the most representative variations were obtained when the irregular terrain is below the overhead line leading to over-voltages near 5 times higher than those occurring over flat ground scenarios.

Based on the obtained results and the analysis made along this thesis, it is proposed as a future work to perform experimental testing for induced voltages above inhomogeneous and irregular grounds in reduced scale experimentations and full-scale controlled induced voltages by triggered lightning experiments, in order to validate their theoretical effects.

From the theoretical analysis and by using the implemented FDTD scheme, it will be interesting to address the modeling of the return-stroke including inclination and tortuosity in order to quantify their effects on the induced voltages taking into account irregular and inhomogeneous propagation paths in order to simulate a more realistic scenario.

9 References

[1] M. Master and M. Uman, "Lightning Induced Voltages on Power Lines: Theory", IEEE Transaction on Power apparatus and Systems, Vol. PAS-103, No. 9, Semptember 1984.

[2] A.K. Agrawal, H. J. Price and H.H. Gurbaxani, "Transient response of multiconductor transmission lines excited by a nonuniform electromagnetic field", IEEE Transactions on , vol.22, no.2, pp.119-129, May 1980.

[3] A.J. Eriksson, M.F. Stringfellow and D.V. Meal, "Lightning induced over-voltages on overhead distribution lines", IEEE Transaction on Power apparatus and Systems, Vol. PAS-101, pp. 960-969, April 1982.

[4] M. Master, M. Uman, W. Beasley, and M. Darveniza, "Lightning Induced Voltages on Power Lines: Experiment", IEEE Transaction on Power apparatus and Systems, Vol. PAS-103, No. 9, Semptember 1984.

[5] V. Rakov and M. Uman, "Lightning Physics and Effects", 2003, Ed. Cambridge University Press.

[6] Rachidi, F., "Recent Progress in Lightning Return Stroke Modeling and Eletromagnetic Field Computation", International Symposium on Lightning Protection SIPDA XI, Brazil 2011.

[7] Y. Baba, and V.A. Rakov, "Electromagnetic models of the lightning return stroke" Journal of Geophysical Research, vol. 112, Feb. 2007.

[8] Y. Baba and V. Rakov, "Applications of the Electromagnetic Models on the Lightning Return Stroke", IEEE Trans, on Power Delivery, Vol.23 No.2, April 2008.

[9] C.A. Nucci, "Lightning Induced Voltages on Overhead Power Lines", Part I, II and III, Electra, August 1995.

[10] J. Herrera, E., Pérez, and H.,Torres, "Statistical Evaluation of Transferred Voltages Through Transformers Due to Lightning Induced Overvoltages", IEEE Bologna PowerTech Conference, June 2003.

[11] E. Perez, J. Herrera and H., Torres, "Sensitivity Analysis on Induced Voltages on Distribution Lines", IEEE Bologna PowerTech Conference, June 2003.

[12] A., Borghetti, A. Morched, F. Napolitano, F., Nucci, C.A. and Paolone, M., "Lightning-Induced Overvoltages Transferred through Distribution Power Transformers", IEEE Transaction on Power Delivery, Vol. 24, No.1, January 2009.

[13] IEEE Guide for Improving the Lightning Performance of Electric Power Overhead Distribution Lines, IEEE Std 1410-2010 (Revision of IEEE Std 1410-2004).

[14] E. Sunde, "Earth Conduction effects in Transmission Systems", Dover Publications, 1949.

[15] F. Rachidi , C. A. Nucci , M. Ianoz and C. Mazzetti "Influence of a lossy ground on lightning-induced voltages on overhead lines", IEEE Trans. Electromagn. Compat., vol. 38, no. 3, pp.250 -264 1996.

[16] T.S.M.Maclean and Z. Wu, "Radion Wave Propagation Over Ground", 1993, Chapman&Hall.

[17] V. Cooray, "On the Accuracy of Several Approximate Theories Used in Quantifying the propagation Effects on Lightning Generated Electromagnetic Fields", IEEE Transactions on Antennas and Propagation, Vol 56, No.7, July 2008.

[18] J. R. Wait, "The Ancient and Modern History of EM Ground-Wave Propagation", IEEE Antennas and Propagation Magazine, Vol. 40, No.5, October 1998.

[19] A. Shoory, A. Mimouni, F. Rachidi, V. Cooray, and M. Rubinstein, "On the accuracy of approximate techniques for the evaluation of lightning electromagnetic fields along a mixed propagation path," Radio Science, vol. 46, no. 2, p. n/a–n/a, 2011.

[20] V. Cooray,"Horizontal Electric Field Above-and Underground Produced by Lightning Flashes", IEEE Transactions on Electromagnetic Compatibility, vol. 52, no. 4, pp. 936 – 943, Nov. 2010.

[21] M. Rubinstein "An approximation formula for calculation of the horizontal electric field from lightning at close, intermediate, and long ranges", IEEE Trans. Electromagn. Compat., vol. 38, no. 3, pp.531 -535 1996.

[22] V. Cooray, "Some considerations on the "Cooray-Rubistein" Formulation used in deriving the horizontal Electric field of lightning Return Strokes over Finitely Conducting Ground", IEEE Transactions on Electromagnetic Compatibility, Vol 44, No.4, November 2002.

[23] M. Ishii, K. Michishita and Y. Hongo, "Experimental Study of Lightning-Induced Voltage on an Overhead Wire over Lossy Ground" IEEE Transactions on Electromagnetic Compatibility, vol. 41, no. 1, pp. 39 – 45, Feb. 1999.

[24] Y. Baba and V. A. Rakov, "Voltages Induced on an Overhead Wire by Lightning Strikes to a Nearby Tall Grounded Object" IEEE Transactions on Electromagnetic Compatibility, vol. 48, no. 1, pp. 212 – 224, Feb. 2006.

[25] D. Pavanello, "Electromagnetic Radiation from Lightning Return Strokes to Tall Structures", PhD Dissertation Thesis, École polytechnique fédérale de Lausanne, 2007.

[26] A. Piantini and J.M. Janiszewski, "Lightning-Induced Voltages on Overhead Lines- Aplication of the Extended Rusck Model", IEEE Trans. Electromagn. Compatibility, Vol 51, No.3, November, 2009.

[27] E. Soto, E.Perez and J. Herrera, "Electromagnetic Field Due to Lightning Striking on Top of a Cone-Shaped Mountain using the FDTD", IEEE Trans. Electromagn. Compatibility, February 2014.

[28] J. Paknahad, K. Sheshyekani, M. Hamzeh and F. Rachidi, "Lightining Electromagnetic Fields and their Induced Voltages on Overhead Lines: The eefect of a non-flat Lossy Ground", *2014 International Conference on Lightning Protection (ICLP)*, vol., no., pp.286,289, 7-11 Oct. 2014.

[29] K. Yee, "Numerical solution of initial boundary value problems involving maxwell's equations in isotropic media," IEEE Transactions on Antennas and Propagation, vol. 14, no. 3, pp. 302 –307, May 1966.

[30] A. Taflove, and S. Hagness, "Computational Electrodynamics: The Finite-Difference Time-Domain Method", Artech House, 2005.

[31] A.Z. Elshebereni, V. Demir, “The finite Difference Time Domain Method for Electromagnetics With MATLAB Simulations”. Raleigh, NC: SciTech Pub., 2009.

[32] K. Kunz and R. Luebbers, “The Finnite difference Time Domain Method for Electromagnetics” CRC Press, 1993.

[33] G. Mur, “Absorbing Boundary Conditions for the Finite-Difference Approximation of the Time-Domain Electromagnetic-Field Equations”, IEEE Transactions on Electromagnetic Compatibility, vol. EMC-23, no. 4, pp. 377 – 382, Nov. 1981.

[34] B. Engquist, and A. Majda, “Absorbing Boundary Conditions for the numerical simulation of waves”, Mathematics of Computation, Vol.31,pp. 629-651, 1977.

[35] Z.P. Liao, H.L Wong, B.P. Yang and Y.F. Yuan, “A transmiting boundary for transient wave analyses”, Scientia Sinica (Series A), Vol XXVII, pp. 1063-1076, 1984.

[36] J.P . Berenger, “Perfectly matched layer for the Absorption of electromagnetic waves”, J. Computational Physics, Vol.114, pp.185-200, 1994.

[37] J.P . Berenger, “Perfectly matched layer for the FDTD solution of wave-interaction problems”, IEEE Trans. Antennas and Propagation, Vol. 44, pp.110-117, 1996.

[38] J.P . Berenger, “Three-dimensional perfectly matched layer for the absortion of electromagnetic waves”, J. Computational Physics, Vol.127, pp.363-379, 1996.

[39] J. Roden and S. Gedeney, “Convolution PML (CPML): An Efficient FDTD implmentation of the CFS-PML for arbitrary media”, Microwave Opt. Technol. Letters. Vol 27, no. 5 pp 334-339, 2000.

[40] K. Umashankar, A. Taflove, and B. Beker, “Calculation and experimental validation of induced currents on coupled wires in an arbitrary shaped cavity,” IEEE Transactions on Antennas and Propagation, vol. 35, no. 11, pp. 1248 – 1257, Nov. 1987.

[41] T. Noda and S. Yokoyama, “Thin wire representation in finite difference time domain surge simulation,” IEEE Transactions on Power Delivery, vol. 17, no. 3, pp. 840 – 847, Jul. 2002.

[42] Y. Taniguchi, Y. Baba, N. Nagaoka, and A. Ametani, "An Improved Thin Wire Representation for FDTD Computations", IEEE Transactions On Antennas And Propagation, Vol. 56, No. 10, October 2008.

[43] H. W. Dommel, Electromagnetic Transients Program (EMTP) Theory Book, Bonneville Power Administration, Portland, OR, 1986

[44] SINTEF Energy Research, ATPDRAW Version 3.5 Users’ Manual, Trondheim, Norway, 2002. Available on: http://www.eeug.org/files/secret/ATPDraw

[45] CanAm EMTP User Group, Alternative Transient Program (ATP) Rule Book, Portland, OR, 2001.

[46] C.R. Paul, “Analysis of Multiconductor Transmission Lines”, 2nd Edition, IEEE Press, John Wiley and Sons, 2007.

[47] C.R. Paul, “Introduction to Electromagnetic Compatibility”, 2nd Edition, Jhon Wiley & Sons, 2006.

[48] N. Theethayi and R. Thottappillil, Surge propagation and crosstalk in multiconductor transmission lines above ground, Electromagnetic Field Interaction with Transmission Linesfrom classical theory to HF radiation effects, Ed. By F. Rachidi and S. Tkachenko, WIT Press 2008.

[49] C. Balanis, Advanced Engineering Electromagnetics, Second Edition, John Wiley and Sons, 2012

[50] R.J. King, “Electromagnetic wave propagation over a constant impedance plane”, Radio Sciences, Vol 4, pp. 255-268,1969.

[51] R.J. King and G.A. Schlak, “The Ground Wave attenuation function for Propagation over highly Inductive Surface”, Scientific Report No. 37, Air Force Cambridge Research Laboratories, Office of Aerospace Research, August 1966.

[52] Ott, R.H. “A new method for predicting HF ground wave attenuation over inhomogeneous, irregular terrain”. Office of Telecommunications Boulder Co. Inst For Telecommunication Sciences, 1971.

[53] C. Constantinou, “Numerically intensive Propagation Prediction Methods”, Propagation of Radiowaves, Chp.21, Ed.Les Barclay, The Intitution for Engineering and Techology, 2012.

[54] Ott, R.H., “An alternative Integral Equation for Propagation over Irregular Terrain” Radio Science, vol. 6, Number 4, pp. 429–435, April 1971.

[55] J. R. Wait, Electromagnetic Waves in Stratified media, New York, Pergamon Press, Second Edition.

[56] R. J. King, S.W. Maley and J.R. Wait, “Groundwave propagation along three-section mixed paths”, Proc. IEE, Vol 113, No.5, May 1966.

[57] V. Cooray and K. Cummings, “Propagation effects caused by multi-section mixed paths on electric fields of lightning return strokes”. International Symposium on Lightning Protection. - Curitiba, Brazil. 2009.

[58] Q. Zhang; D. Li; Y. Zhang; J. Gao; Z. Wang, "On the Accuracy of Wait's Formula Along a Mixed Propagation Path Within 1 km from the Lightning Channel," Electromagnetic Compatibility, IEEE Transactions on , vol.54, no.5, pp.1042,1047, Oct. 2012.

[59] Y. Baba and V. A. Rakov, “On the mechanism of attenuation of current waves propagating along a vertical perfectly conducting wire above ground: application to lightning,” IEEE Transactions on Electromagnetic Compatibility, vol. 47, no. 3, pp. 521 – 532, Aug. 2005.

[60] S. Bonydi-Ram, R. Moini, S.H. H. Sagedghi and V.A. Rakov, “On the representation of lighthning return stroke as a lossy monopole antenna with inductive loading”, IEEE Transactions on Electromagnetic Compatibility, vol. 50, no. 1, pp. 118 – 127, Feb. 2008.

[61] V. Rakov and M.A. Uman, “Review and evaluation of lightning return stroke models including some aspects of their application”, IEEE Trans. Electromagnetic Compatibility, Vol.40 No.4, pp 403-426, Nov 1998.

[62] F. Rachidi and C.A. Nucci, “On the Master, Uman, Lin, Standler and the modified trasmission line lightning return stroke current models”, J. Geophys. Res, Vol.95, 1990.

[63] G. Maslowski and V. Rakov, “Equivalency of Lightning Return-stroke models employing lumped and distributed current sources”, IEEE Transactions on Electromagnetic Compatibility, vol. 49, no. 1, pp. 123 – 132, Feb. 2007.

[64] R. Moini , B. Kordi , G. Z. Rafi and V. A. Rakov "A new lightning return stroke model based on antenna theory", J. Geophys. Res., vol. 105, no. D24, pp.29693 -29702 2000.

[65] S. Bonydi-Ram, R. Moini, S.H. H. Sagedghi and V.A. Rakov, "On the representation of lighthning return stroke as a lossy monopole antenna with inductive loading", IEEE Transactions on Electromagnetic Compatibility, vol. 50, no. 1, pp. 118 – 127, Feb. 2008.

[66] Gibson, W., The Method of Moments in Electromagnetics, 1st ed., vol. 1. Chapman & Hall, 2008.

[67] Burke, G. Numerical Electromagnetic Code NEC-4, Method of Moments, Part I, User´s Manual, Jan 1992.

[68] Q. Zhang, D. Li, Y. Fan, Y. Zhang, and J. Gao, "Examination of the Cooray-Rubinstein (C-R) formula for a mixed propagation path by using FDTD", J. Geophys. Res., 2012.

[69] J. R. Wait "Concerning the horizontal electric field of lightning", IEEE Trans. Electromagn. Compat., vol. 39, no. 2, pp.186 1997.

[70] M. Khosravi-Farsani; R. Moini; S.H.H. Sadeghi; F., Rachidi, "On the Validity of Approximate Formulas for the Evaluation of the Lightning Electromagnetic Fields in the Presence of a Lossy Ground," Electromagnetic Compatibility, IEEE Transactions on , vol.55, no.2, pp.362-370, April 2013.

[71] V. Cooray, "Calculating Lightning-Induced Overvoltages in Power Lines: A Comparison of two Coupling Models", IEEE Trans. Electromgan. Compatibility, Vol.36, No.3, August 1994.

[72] F. Rachidi, "Formulation of the field-to-transmission line coupling equations in terms of magnetic excitation field", IEEE Trans. Electromagn. Compat., vol. 35, no. 3, pp.404 -407 1993.

[73] V. Cooray and V. Sckuka, "Lightning-Induced Voltages in Power Lines: Validity of various Approximations made in Overvoltage Calculations", IEEE Trans. Electromagn. Compatibility, Vol 40, No4, November, 1998.

[74] R.K. Pokharel, M. Ishii and Y. Baba, "Numerical Electromagnetic Analysis of Lightning-Induced Voltage Over Ground of Finite Conductivity", IEEE Transactions on Electromagnetic Compatibility, vol. 45, no. 4, pp. 651 – 656, Nov. 2003.

[75] C.A. Nucci, F. Rachidi, M. Ianoz and C. Mazzetti, "Lightning-Induced Voltages on Overhead Lines", IEEE Trans. Electromagn. Compatibility, Vol.35, No.1, Febraury 1993.

[76] B. Yang, B.H. Zhou, C. Gao, L.H. Shi, B. Chen, and H.L. Chen, "Using a Two-Step Finite-Difference Time-Domain Method to Analyze Lightning-Induced Voltages on Transmission Lines", IEEE Trans. Electromagn. Compatibility, Vol.53, No.1, Febraury 2011.

[77] R.E. Jiménez-Mejía, J. Herrera-Murcia, "Lightning induced voltages on overhead lines above an inhomogeneous ground," *Lightning Protection (XII SIPDA), 2013 International Symposium on* , vol., no., pp.241,248, 7-11 Oct. 2013

[78] Sheshyekani K. and Paknahad J. "The effect of an Ocean-Land Mixed propagation path on the lightning Electromagnetic Fields and Their Induced Voltages", IEEE Trans. Power Delivery, Vol.30, No.1, July 2014.